UNIVERSITÀ DEGLI STUDI DI MILANO - BICOCCA
DIPARTIMENTO DI FISICA G.OCCHIALINI

CORSO DI DOTTORATO IN FISICA E ASTRONOMIA

MultiPhoton Multifocal Methods For Neuroscience and Hemodynamics

Settore scientifico disciplinare: FIS/07

Tesi di dottorato di:
PAOLO POZZI

Tutor: Prof. Giuseppe Chirico

Co-Tutor: Prof. Egidio D'Angelo
Dott. Jonathan Mapelli
Dott.ssa Daniela Gandolfi

Anno Accademico 2013/2014

"Experimental science is like that fickle girl you like:
each day she makes you more disgruntled and dejected,
but she only has to smile at you once,
and you are back in love again."

Contents

Introduction

A common assumption about biological research is that most systems of interest evolve on very slow time scales. That is easily apparent since biologists usually work on solutions of molecules of interest, cultured cells, or acute tissues, all of which are apparently still or anyway changing and evolving on very slow time scales. It is however not to be forgotten that the aim of biological research is the understanding of life and living organisms, which, while being formed by tissues, cells, and, in the end, interacting molecules, are extremely fast, yet complex systems, in which the ability to react to an external stimulus has been incessantly optimized by evolution over million of years.

Even simple actions imply a series of complex events, both on a macroscopic and microscopic scale, which happen in very short time scales and in near-perfect coordination; for example, when catching an object as it flies, an action which can be performed in few hundreds of milliseconds, the retinas are acquiring a series of images of the object, while the muscles of the eyes keep the field of view centered on the object itself, the brain, besides taking the decision of catching the object, gathers the information from the retina and the eye muscles, calculates the trajectory, and communicates to the arm muscles in order to move the hand in a position where the object will land shortly. The muscle contraction itself happens extremely fast in a controlled way, converting energy coming from glicolysis to mechanical motion.

All of these fast macroscopic events are based on underlying microscopic mechanisms, acting even faster, and their comprehension has primary importance in the understanding of the organism as a whole.

Progress in biological research is always sustained by development and refinement in research methods, among which fluorescence microscopy has always had a prominent role, due to its high versatility and signal/noise ratio in sensing and its low impact on the living samples when kept in physiological conditions. Recent advances in optical microscopy have mainly followed the commendable aim of increasing spatial resolution, specificity, and biocompatibility, but relatively few steps were made on the front of time resolution and on the study of

correlated actions.

This thesis describes two separate and partially complementary fluorescence microscopy implementations specifically developed to study fast phenomena in living biological samples on the millisecond scale, while preserving three dimensional, diffraction limited spatial information. In particular one setup is specifically developed for the recording of the activity of multiple neurons in the cerebellar cortex, and the other for the characterization of blood flow dynamics in zebrafish embryos. Both optical setups and the data analysis developed hereafter, are based on the exploitation of pixelated detectors combined to two photon fluorescence excitation and structured diffraction limited focalization in the field of view.

The activity of cerebellar neuronal network was studied through an original high speed two photon calcium imaging method, at the cutting edge of molecular neurophysiology research. Calcium imaging is a technique based on the staining of tissues with fluorescent dyes changing their fluorescence emission depending on intracellular calcium concentration; in its traditional two photon form, it is performed through the use of a galvanometric scanner, which has limited movement speed, so that millisecond scale acquisitions can be performed only on single lines, while only a few images per second can be acquired on large fields of view. In Part II of this thesis an original method for high speed calcium imaging is presented. The experimental setup is based on a fast sCMOS detector and a spatial light modulator, which allows the creation of multiple focal points at user selected positions throughout the field of view. Through such system a confocal image of the sample can be acquired, and multiple pixels of interest can be selected and simultaneously illuminated, so that the detector can acquire fluorescence signals from all the points on the millisecond scale. The system was successfully employed on cerebellar slices to study the fast dynamics of calcium concentration in the cellular soma and the spatial organization of the excitatory and inhibitory balance of the network.

Blood flows in animal models, here Zebrafish embryos, were studied through a dedicated experimental setup for spatial fluorescence cross correlation spectroscopy (sFCCS), a variation of the standard fluores-

cence correlation spectroscopy based on the statistical analysis of fluorescence signals from two separate locations in the field of view. While the theory of the cross-correlation analysis in fluorescence spectroscopy was already developed, the only optical implementations are based on the use of fixed beam splitters and two separate photon counting detectors: the complexity of such system, the difficulty of image acquisition on the same setup, and limitations in focuses positioning, limited its reported applications to simple test systems in vitro. The alternative experimental setup for sFCCS presented in the third part of this thesis thesis, based on an EMCCD detector, a modified interferometer for focuses placement and a galvanometric mirrors system for images acquisition, is technically simpler to use and more versatile, allowing the precise positioning of the excitation volumes at user selected positions in a confocal image of the sample. This setup has been applied here to the study of the blood flow in Zebrafish embryos, in order to estimate the speed of the circulation, the dynamics of hearth strokes, and the shear stress in blood vessels.

The thesis is divided as follows: in Part I a brief introduction to the physiology of neuronal networks and cardiovascular systems, and the state of the art in microscopy techniques for their study is reported. Part II describes the technique of high speed holographic imaging, with the necessary theoretical background, the description of the setup, and a report of calcium imaging experiments of biological interest performed on cerebellar acute slices. Part III describes the sFCCS technique, with the necessary theoretical background, the description of the setup, and a report of experiments of biological interest performed on Zebrafish embryos.

Part I.

Optical microscopy for functional biological imaging

1. Fluorescence Microscopy

1.1. General outlook

The acquisition of images is an extremely important part of biological research. While images of nanometric and sub-nanometric structures can be efficiently acquired through electron microscopy and atomic force microscopy, such techniques generally require complex sample treatments, usually undermining its functionality. Optical microscopy, while only being able to resolve micrometric structures, is still the most widely used imaging technique in biological research, due to its relative simplicity, and its compatibility with the use of living samples.

While there are a number of techniques to acquire images of light transmitted or reflected by the sample, often the structures of biological interest do not provide any contrast in this kind of images. High contrast images of specific structures can be acquired through fluorescence microscopy.

Fluorescence is the molecular event in which a molecule is excited to a vibrational level of an higher quantum state through absorption of a photon. The vibrational energy acquired is dissipated as heat in few picoseconds, and a photon is emitted after a few nanoseconds, when the molecule relaxes to the ground state. Due to the heat dissipation at the excited state, the emitted photon has lower energy, and therefore longer wavelength, than the absorbed one, generating a gap between the absorption and emission spectra called *Stokes shift*.

Most organic molecules have absorption and emission spectra in the ultraviolet range, but some molecules are fluorescent in the visible range. Visible fluorescent molecules can be functionalized in order to bind them to specific biological structures. Moreover, since the discovery of the green fluorescent protein (GFP), it is possible to create

samples expressing fluorescent versions of proteins of interest, thus allowing to obtain intrinsic fluorescence from virtually any structure of interest in a sample.

This chapter describes the most used microscopy techniques for the recording of fluorescence images and signals, with a special focus on acquisition frequency.

1.2. Epifluorescence microscopy

The easiest and most used technique for the acquisition of μm scale fluorescence images is epifluorescence microscopy. An epifluorescence microscope is based on a standard infinity corrected microscope which can be described as a two lenses system.

The first lens is the objective, which should have a short focal length, and an high numerical aperture in order to obtain magnified images with high spatial resolution. The sample is placed in the focal plane of the objective, so that an image of it is formed at an infinite distance.The second lens, called tube lens, creates an image of the sample in its focal plane, where a pixelated detector is usually placed. The total magnification of the system is given by the ratio $\frac{F_t}{F_o}$, where F_t is the tube lens focal length, and F_o is the objective focal length[1]. One of the advantages of an infinity corrected objective is the possibility of adding optical elements, such as mirrors and filters, in the space between the objective and the tube lens, called infinity space, without changing the axial position of the image created by the tube lens. In an epifluorescence microscope, a dichroic mirror and a fluorescence filter are placed in the infinity space[2], as shown in figure 1.1, panel A. The fluorescence filter is a bandpass filter which only transmits fluorescence emission wavelengths, while the dichroic mirror, placed at 45° with respect to the optical axis, reflects light in the excitation spectra, and transmits fluorescence light. In this configuration, an incoherent light source at the excitation wavelength (usually a white lamp with a fluorescence filter, or an LED light) is collimated by a lens, and reflected by the dichroic mirror in the objective back aperture, so

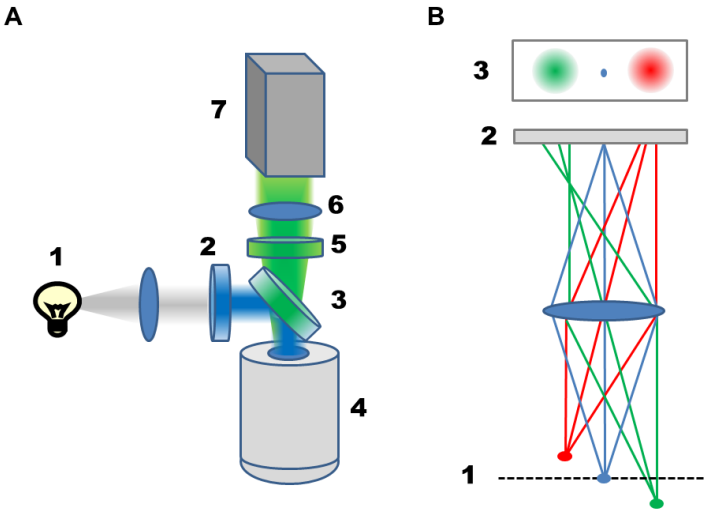

Figure 1.1.: Epifluorescence microscopy.

A. scheme of an epifluorescence microscope. 1. Incoherent light source. 2. Excitation filter. 3. Dichroic mirror. 4. Microscope objective. 5. Emission filter. 6. Tube lens. 7. Pixelated detector. B.Out of focus contribution. For simplicity the microscope is represented as a single lens, of unitary magnification. The focal plane (1) is conjugated to the plane of the pixelated detector (2). Objects on focus, like the blue spot, will be sharp on the final image (3), while out of focus objects, like the red and green spots, will be blurry, and illuminate a large area of the detector.

that the focal plane of the objective is uniformly illuminated at the excitation wavelength. The fluorescence signal elicited in the sample is collected by the objective, transmitted through the dichroic mirror and the fluorescence filter, and generates an image through the tube lens on the detector surface.

The main drawback in epifluorescence microscopy is the contribution of out of focus fluorescence. While the technique works well in bidimensional sample, like cultured cells or thin tissue slices, in three dimensional samples, such as thick slices, or in vivo imaging, fluorescent structures on out of focus planes will create a blurred background

on the image acquired by the detector, as shown in figure 1.1, panel B. The most used method to solve the problem of out of focus contribution is confocal microscopy (see section §1.3), but epifluorescence microscopy remains the simplest and cheapest fluorescence imaging technique, and, being based on the use of a pixelated detector, is the fastest commercially available technique for fast recordings over wide fields of view.

1.3. Confocal microscopy

As discussed in the previous section, standard epifluorescence microscopy is not an adequate technique for imaging in three dimensional samples, as out of focus structures contribute to the image of the focal plane with a bright background, deteriorating contrast and resolution. In order to suppress out of focus contributions, a confocal microscope (represented in figure 1.2, panel A) is needed. In confocal microscopy, the excitation light is focalized on a single point, as small as possible, in the focal plane, while a tight pinhole is placed on the image plane. In this way, as represented in figure 1.2, panel B, light emitted in the small illuminated spot passes through the pinhole, while out of focus light is blocked for the most part. Obviously, in this kind of configuration, the system does not acquire an image, instead it measures the fluorescence light obtained by illuminating the sample in a single point. Therefore a pixelated detector is not needed anymore, instead a light detector, such as a photodiode or a photomultiplier is employed. In order to acquire an image with a confocal microscope, this punctual measure of fluorescence should be performed many times in different positions, covering the desired field of view. Usually the focal spot is moved in a raster scan pattern, traveling at constant speed along an horizontal line, then moved back as fast as possible, shifted vertically on a small distance, moved at constant speed again on another line, and so on. This way the fluorescence intensity measured in each point is converted in a digital value and the resulting image is generated by a calculator. This image represents the fluorescence intensity distribution on a single two dimensional plane (confocal plane). A three dimensional image can be

generated by acquiring multiple confocal images at multiple depths.

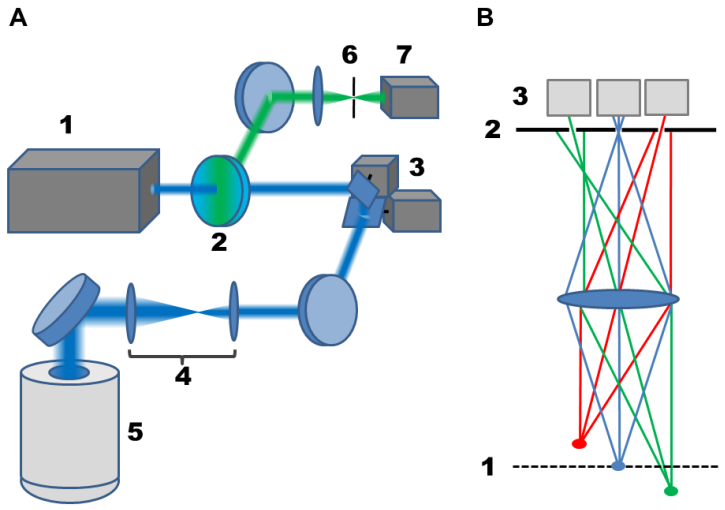

Figure 1.2.: Confocal microscopy.

A. Scheme of a single photon confocal microscope. 1.Coherent excitation light source. 2.Dichroic mirror. 3.Galvanometric mirrors. 4.Scanning head. 5.Microscope objective. 6. Pin-hole. 7. Light detector. B. Suppression of out of focus contribution. For simplicity the system is represented as a single imaging lens, with multiple pinholes and detectors; real system has more complicated optics, but a single pinhole and detector. The focal plane (1) is conjugated with the pinhole plane (2). Light coming from the illuminated point in the focal plane, represented in blue, is entirely transmitted through the pin-hole, while out of focus light, represented in red and green, is blocked for the most part on the pinhole plane.

In order to create a confocal microscope there are therefore two requirements, the generation of the smallest possible illumination spot, and the possibility of moving the illuminated spot in the focal plane, while keeping its image on the pinhole for detection.

A small illumination spot can be obtained in incoherent light by introducing a pinhole in the illumination pattern too, and using a lens to conjugate the excitation pinhole plane with the focal plane of the objective. While this technique was widely used in early confocal mi-

croscopy implementations, modern microscopes rely on coherent illumination sources. A collimated coherent Gaussian beam, filling the objective's back aperture, generates the smallest possible spot, with dimensions physically limited only by diffraction (see section §5.1).

The simplest way to illuminate the focal plane in different positions is to physically move the sample, while keeping the optical system still. However, sample motion is usually not recommended with biological samples, and, moreover, the speed of sample motion is limited, leading to long acquisition times for a single image. In modern confocal microscopes, galvanometric mirrors are used in order to scan excitation light on a still sample. The position of the illumination spot in the focal plane can be changed by changing the angle at which the laser beam impinges on the objective back aperture, while keeping it collimated and centered.

In order to achieve such configuration, a couple of galvanometric mirrors is used to steer the excitation beam on two axes. A two lenses telescope (scanning head) conjugates the plane of the galvanometric mirrors to the objective back aperture. As the image of the beam on the mirrors remains still even if the mirrors are tilted, this configuration keeps the beam centered on the back aperture during scanning. The telescope configuration of the lenses keeps the beam collimated, moreover, the diameter of the beam is expanded (or reduced) depending on the ratio between the two focal lenses, thus enabling the perfect filling of the back aperture.

This kind of optical system allows for the motion of the excitation light over the sample; in order to obtain an image of the sample, however, the fluorescence light generated must be focalized on the pinhole, regardless of the excitation beam position. To achieve such condition, the dichroic mirror is placed between the excitation source and the galvanometric mirrors, so that fluorescence light reflected by the mirrors receives opposite steering with respect to the excitation beam; a lens positioned after the dichroic mirror will therefore focalize the fluorescence light in the same position, where a pinhole is placed, regardless from the mirrors movement.

Three dimensional images can be acquired by moving only the objec-

tive in the axial direction, as a movement of the back aperture position of some micrometers does not effectively affect the position or dimension of the focal spot.

It is important to notice that, although three dimensional imaging can be achieved with a confocal microscope, the imaging depth achievable is strongly dependent on the sample nature. In the acquisition of three dimensional images, several factors can affect the images quality while penetrating in depth in a tissue:

- Out of focus excitation light absorption: In most three dimensional samples, fluorescent molecules are present in all of the volume. This means that, imaging deeper planes in the sample, excitation light can be absorbed by fluorophores closer to the surface, generating fluorescence light which is rejected by the pinhole. In the presence of out of focus absorption, only a fraction of the excitation light actually reaches the focal point. As absorption in a thick sample follows the exponential *Lambert-Beer* law, this is the main limiting factor in confocal microscopy imaging depth.

- Excitation light scattering: Even in particular samples, where fluorophores are confined in deep locations and there is no out of focus absorption, excitation efficiency is still affected at deep focal planes by light scattering, which reduces excitation power at the focal point, and affects the wavefront, thus making the excitation volume bigger and affecting image resolution.

- Fluorescence light scattering: Fluorescence light coming from the focal volume is affected by scattering in its way to the objective. As the pinhole selects only photons coming from the focal volume position, scattered photons will be rejected by the pinhole, thus decreasing the total signal.

The use of galvanometric mirrors and a scanning head allows the acquisition of confocal images at relatively high speed, without moving the sample. There are two main limiting factors in the acquisition speed of a confocal microscope:

- The galvanometric scanner speed. As any mechanical device, the rotation speed and acceleration of galvanometric mirrors is limited. While constant rotation speed isn't usually an issue, changes in rotation direction, needed at the end of each line of an image, usually require a longer time, thus limiting the speed of the entire acquisition process. Faster image acquisition can be achieved with resonant scanning galvanometric mirrors. Instead of moving the focal volume at a constant speed during the acquisition of a single line in the image, a resonant scanner speed varies in a sinusoidal waveform, thus avoiding abrupt changes in the movement direction. The downside in the use of a resonant scanner is that the time spent by the focal volume in each pixel is not constant, therefore a software correction on the acquired image is required.

- The pixel dwell time: During acquisition, fluorescence signals from single positions are stored separately as pixels of the final image. Each pixel should correspond to an area smaller than the dimension of the excitation spot, in order to gather all the possible information from the image. It is therefore required that a larger field of view should be divided in more pixels. As the signal to noise ratio of a light intensity measurement increases with integration time, the sampling of a wide field of view with adequate pixel sampling is often limited by the detector efficiency, and not by the scanner speed. Higher excitation light power can increase signal to noise ratio at high acquisition speeds, but at the cost of high photobleaching and sample photodamage, and anyway only up to a saturation level where the ground state of fluorescence molecules is completely depleted.

1.4. Spinning disk confocal

As reported in the previous section, the ultimate limit in confocal image acquisition speed is given by the signal intensity at very low pixels dwell times. As this limit is due to the serial nature of the acquisition,

the only way to increase time resolution is the acquisition of signals over multiple focal points simultaneously. In order to achieve parallel scanning a different optical setup, called spinning disc microscope, is used[3]. In this configuration, schematically represented in figure 1.3, a disk with multiple pinholes is placed in an optical plane conjugated with the focal plane of the objective, so that, when excitation light impinges on the disk from the back side, an array of excitation spots is generated on the sample. The positions of the pinholes on the disk are designed so that, while the disk spins on its axis, the focal points are scanned on the sample, illuminating the entire field of view. The dichroic mirror is placed on the back side of the disk, so that the pinholes used to generate the array of focal points acts as an array of confocal pinholes too. After the dichroic mirror, on another plane conjugated to the disk plane, the image is formed on a pixelated detector, usually a CCD or a CMOS camera.

In order to obtain an image, a single exposure of the camera is acquired, while the field of view is sequentially illuminated. This procedure allows for extremely fast imaging, with a theoretical frame rate limit of up to thousands of frames per second set by the disk rotation speed, and a real limit set by the camera acquisition rate. Despite its frame rate enhancement with respect to standard confocal microscopy, there are several drawbacks in the use of spinning disk confocal:

- Excitation efficiency: Most of the excitation light provided is stopped, and partially reflected, by the disk. In addition to the inevitable decrease in actual excitation power reaching the sample, part of the back reflected excitation light can reach the detector, providing an undesired background, and therefore avoiding the detection of low fluorescence structures. This problem can be partially addressed by adding a second spinning disk with microlenses focalizing the excitation light on the pinholes. Even with such precaution, however, the maximum reported light efficiency is about 40%[4].

- Fixed pinhole aperture: In a standard confocal microscope, the size of the pinhole can be adapted to the objective numerical

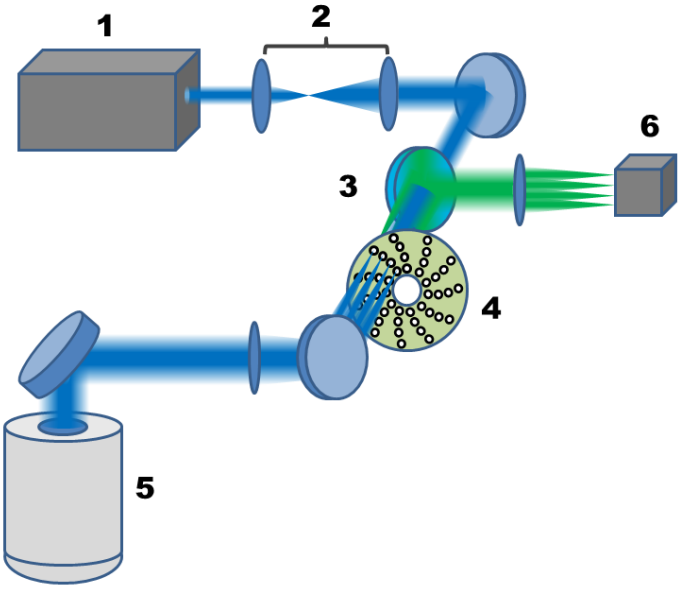

Figure 1.3.: Spinning disk confocal microscope.

1. Excitation light source. 2. Beam expander. 3. Dichroic mirror. 4. Nipkow disk. 5. Microscope objective. 6. Pixelated detector.

aperture. In spinning disk microscopy, the size of the pinholes is fixed, and therefore optimized for a single objective. Using an objective with higher magnification, or lower numerical aperture would mean losing signals, while using a lower magnification or higher numerical aperture would mean losing axial resolution.

- Pinholes crosstalk[4]: In a confocal microscope, the fluorescence from out of focus structures illuminates the pinhole plane in a wide area, with a diameter proportional to the objective numerical aperture and to the axial distance of the structure from the focal plane. While in a standard single pinhole microscope all of this light is always rejected, in a spinning disk microscope the pinhole rejection works properly only if the diameter of the out

of focus image is smaller than the distance between two pinholes. This means that, if there are fluorescence structures at an high axial distance from the focal plane, they will create an undesired background on the final image. This kind of artifact practically limits the maximum axial dimension of the studied samples, and the limitation gets tighter while using an high numerical aperture objective.

1.5. Two photon microscopy

As considered in previous sections, three dimensional confocal imaging is severely limited in depth, especially in strongly scattering samples. Imaging in thick and turbid media can be achieved through multiphoton microscopy[5]. Multiphoton microscopy is extremely similar in concept to standard confocal microscopy, as it uses a coherent excitation source, a couple of galvanometric mirrors, and a light detector. The main difference lies on the exploitation of two photon fluorescence excitation.

Two photon fluorescence excitation is the simultaneous absorption from the fluorophore of two photons at roughly twice the wavelength of single photon excitation. The process is nonlinear, and in particular the probability of two photon absorption is quadratically dependent on the excitation power. The main consequence of the non linearity of two photon excitation is that, focusing laser light with an high numerical aperture objective, fluorescence emission is confined in a tight, diffraction limited volume in the focal point. Exploiting two photon excitation for fluorescence microscopy has several advantages:

- Infrared excitation: Since most fluorescent molecules used in biology are excited in the visible range, typical two photon excitation wavelengths lie in the near infrared range. This is convenient, as light scattering is proportional to $\frac{1}{\lambda^4}$, thus allowing the focalization of infrared light deeper in tissues. Moreover, the absorption properties of water, hemoglobin and melanin are minimum in the near infrared region of the spectra, making two

photon microscopy ideal for intravital application. The downside in the use of infrared excitation light is the loss in image resolution, which is directly proportional to the excitation wavelength.

- Absence of out of focus absorption: As two photon excitation is only possible in the focal volume, out of focus fluorescent molecules do not absorb excitation light, and therefore do not emit fluorescence. As the only fluorescence light present is generated in the focal volume, there is no need to select focal photons through the pinhole. This makes a two photon microscope optically simpler than a standard single photon confocal, as the dichroic mirror and the detector can be positioned just above the objective, as fluorescence light does not have to be descanned through the mirrors and pass through the pinhole. Moreover, the absence of a pinhole means that even fluorescence light scattered in its way back to the objective is integrated as signal, further improving the achievable imaging depth of the system.

- Broadband excitation: Two photon absorption spectra are usually much wider than their single photon counterparts, this means that usually multiple fluorescent molecules with different emission spectra can be excited with a single excitation wavelength, allowing simultaneous multichannel imaging. This simplifies further the optical setup, as multichannel acquisition in single photon confocal microscopy requires perfect alignment of multiple excitation sources, specific dichroic filters, and careful selection of fluorophores to avoid superposition between the emission spectra of a molecule and the excitation wavelength of another one.

While a two photon microscope is generally simpler in design than a standard single photon confocal, the low probability of two photon excitation requires a high flux of photons in order to elicit detectable fluorescence. Such an high excitation power is usually provided by a femtosecond pulsed tunable Ti:Sa laser, which provides the needed flux of photons during pulses, while keeping the average power relatively low, in order to avoid photodamage of the sample.

1.6. Multiphoton multifocal microscopy

Since a two photon microscope is based on a galvanometric scanner, the acquisition speed limits are the same of a standard confocal. However, even if some implementations are reported[4], realizing a spinning disk two photon microscope would prove problematic, due to the low transmission of excitation light through the Nipkow disk. In order to obtain two photon parallel scanning, a different setup, known as a multiphoton multifocal microscope is more widely used[6]. Multiphoton multifocal microscopy takes advantage of Fourier optics (see section §5.1 and 5.2) in order to illuminate the sample with multiple diffraction limited excitation volumes. The generation of multiple focuses is obtained by placing a diffractive plate in an optical plane conjugated with the objective back aperture. The excitation focuses are then scanned in the focal plane through a standard galvanometric scanner, therefore the increase in maximum frame rate is proportional to the number of focal points generated by the diffractive element.

Once the excitation power is divided in multiple focuses, there are different possible configurations for light detection. The easiest and fastest configuration is based on a high resolution pixelated detector, which is exposed for the entire duration of the scan, as it happens in spinning disk microscopy. In this configuration, light can be distributed over tens of excitation volumes, thus granting elevated acquisition speed, up to hundreds of frames per second. Due to the lack of pinholes, however, scattered fluorescence photons are free to reach the detector, contaminating neighboring pixels, and therefore drastically reducing resolution when imaging in depth in strongly scattering tissues.

An alternative, more efficient, but more complex method, is the use of photon counting detector, such as a SPAD, and temporally separating the laser pulses of the different focuses. In this way the position of origin of fluorescence photons can be determined from the time of detection, even if they are scattered by the tissue. This method however can only be applied on few focuses (a commercial version is available with eight focal points), thus reducing the enhancement in temporal

resolution.

1.7. RAMP microscopy

For the purpose of beam scanning, an alternative to galvanometric mirrors is given by acousto optic deflectors[7]. These devices are based on Bragg diffraction in transparent photoelastic materials, whose refraction index changes with mechanical strain. When an acoustic standing wave is generated in a photoelastic material, most of the light of a beam impinging at the Bragg angle is deviated in the first order of diffraction, at an angle proportional to the wave frequency. An acousto optic deflector has comparable deflection properties to a galvanometric scanner, but has the advantage of being free of inertia, thus allowing rapid changes of direction in the focal point motion. Acousto optic deflectors can not be used for scanning in standard, single photon confocal microscopes, as the light deflection is dependent on the wavelength, thus making fluorescence light descanning impossible.

As discussed in section §1.3, the main time resolution limit in imaging a large field of view with a scanning microscope is given by the minimum pixel dwell time required for adequate signal integration. The use of acousto optic deflectors is therefore not particularly convenient in raster scan imaging. However, in the study of many fast biological dynamics, the aim of the experiment is the acquisition of signals from multiple small regions distributed over the field of view. In this situation, acousto optic deflectors allow a rapid shift in the focal point position, in order to serially illuminate multiple points of interest, without having to scan the entire image plane.

This technique is called random access multiphoton microscopy (RAMP)[8], and is the fastest reported technique for monitoring fluorescence signals in multiple locations, reaching kHz frequency on up to 20 points of interest. The main limitation in the technique is still due to the pixel dwell time, which, due to the serial nature of the measurement, limits the number of points of interest studied at a given acquisition frequency.

1.8. A different perspective: SPIM

All of the techniques for confocal imaging described in the previous sections rely on serial illumination of diffraction limited points, and the final image is obtained by software reconstruction (or camera integration, in the case of spinning disk microscopy). A different possible approach is the realization of a properly confocal illumination, where only a thin plane of the sample is illuminated by excitation light. This can be achieved by selective plane illumination microscopy (SPIM, also known as lightsheet microscopy, or ultramicroscopy), a technique in which two microscope objectives are used, one focalizing an excitation light sheet in the sample, the other generating the fluorescence image on a pixelated detector.

In order to generate the light sheet illumination, a laser beam at the excitation wavelength is expanded, and focalized through a vertical cylindrical lens on the illumination objective's back aperture. Since light is focalized by a cylindrical lens, the back aperture of the objective is illuminated in a line pattern, very thin in the horizontal axis, and extended over all of the back aperture in the vertical axis.

As the back aperture is properly filled only on the vertical axis, the point spread function at the focal plane is very wide horizontally, and diffraction limited vertically. The diffraction limited vertical shape is conserved axially for approximately the Rayleigh length of the objective $\left(z_R = \frac{\pi\omega_0^2}{\lambda}\right)$, where ω_0 is the beam waist $\left(\omega_0 = \frac{\lambda}{2N.A.}\right)$.

The detection objective is mounted on the direction perpendicular to the lightsheet, therefore obtaining images which have the lateral resolution of an epifluorescence microscope, and an axial resolution equal to the lateral resolution of the illumination objective. The field of view is limited axially, on the propagation axis of the lightsheet, by the Rayleigh range of the illumination objective, therefore a low N.A. objective should be used for illumination in order to obtain an usable field of view.

Through SPIM, confocal images with a wide field of view can be acquired at the maximum speed allowed by the detector. However the technique has several limitations:

- Sample support: While most of the samples observed in optical microscopy are relatively thin, and mounted on glass microscopy slides, this is not a useful configuration for SPIM, since the illumination beam would propagate in a parallel direction to the glass slide, introducing aberrations. The ideal sample for SPIM should be mounted in a three dimensionally structured, uniform and transparent media, with smooth and planar surfaces. Most SPIM samples are included in low density agarose gel, but some biological system can not be included in gels.

- Light scattering: As the entire focal plane is simultaneously illuminated, and no pinhole is present, scattering of fluorescence light in its optical path to the objective creates artifacts on the image. Moreover, excitation light has to propagate through the sample on the lateral direction of the image. If the sample is uniformly scattering, the axial resolution of the image is affected. moreover, the presence of scattering objects in the sample, can create striped artifacts on the image. Therefore the sample should present low scattering properties, and should not extend too much out of the field of view in the direction of the illumination objective.

- 3D Imaging: Confocal 3D imaging is usually obtained by shifting the objective position, in order to avoid stressing the sample. In SPIM moving both the objectives can prove extremely difficult, therefore 3D imaging is achieved by moving the sample through a piezoelectric actuator, or by moving the lightsheet through galvanometric mirrors, and synchronizing such motion to the one of the collection objective.

2. Pixelated detectors

When fluorescence light is produced throughout the field of view, traditional microscopes relied on eyepieces, in order to generate an image of the sample on the experimentator's retina, which has been for centuries the most sensible, fast and reliable pixelated photodetector available in optical microscopy. Nonetheless procedures as images storing, ultraviolet and infrared detection, and numerical image analysis, could not obviously be performed by the experimentator, leading to the development of digital devices capable of detecting images, and transferring them to a calculator as a matrix of numbers, each representing light intensity at a given location. Up to recent years digital devices had significantly lower sensitivity and spatiotemporal resolution compared to the human retina, technological advances in this field led to the production of extremely fast, sensible, and resolved detectors; up to the point where modern microscopy setups, while still having eyepieces available, are often only used through a digital camera.

This chapter describes the basic working principles of traditional CCD detectors and some of their most significant evolutions, and then covers in detail the technology used in the sensors employed for the measurements reported in chapter 8 and chapter 11. A last section describes the state of the art in the development of commercial arrays of photodiodes and photomultipliers, which, while not actually ready for extensive use in optical microscopy, are a promising technology for future applications.

2.1. CCD detectors

The first digital pixelated photodetector implementation was reported by Thompsett et Al. in 1971[9], based on a charge coupled device

(CCD), invented by W.S.Boyle and G.E. Smith in 1970 [10], and the design, although heavily improved in the following 40 years, is still used for most modern detectors.

A CCD is a semiconductor device capable of storing electric charge in multiple "potential wells", and of moving said charges by a variation in the wells potentials. The potential wells are created by conductor plates separated from the semiconductor by a thin layer of isolating material. As the plate is positively charged, a potential well is formed in the semiconductor, and eventual charge-hole couples formed in the semiconductor near the plate is prevented from recombining.

In a bidimensional CCD for imaging use, the semiconductor is generally silicon, with different doping properties depending on the wavelengths which it is intended to detect. The semiconductor is covered with an array of equally spaced plates creating charge wells; each pixel of the CCD is formed by nine charge wells, organized in three rows of three wells each. The potential of each well is positive, but inside each pixel the potential gets higher from the top to the bottom row, and in each pixel's rows it gets higher from left to right, so that all the negative free electrons generated in the semiconductor move, following the potential gradient, to the bottom right well of the pixel in which they were generated, and are stored there. An analog to digital converter (ADC) is located in the bottom right corner of the device.

In order to acquire an image, all of the pixels of the device, except from the line at the bottom, are exposed for a given amount of time (exposure time) to incoming light. Each photon absorbed by photoelectric effect generates an electron-hole couple, and the electron is stored in the pixel where the photon was absorbed.

At the end of the exposure time, a mechanical shutter stops the exposure to incoming light, and the electrons stored at each pixel are moved, one pixel at a time, to the bottom right corner of the device, generating a current which, in earlier devices, was used as a signal for a cathode ray tube in order to show the acquired image, and in more recent devices is converted to numerical values by an analog to digital converter (ADC) in order to store the image in a calculator memory.

In order to move the electrons toward the DAC, without mixing the

electrons from adjacent pixels, the potentials of the charge wells are swapped following a clock cycle. In a first step, the potential values of each well is simultaneously converted to the potential value of the well above it, so that the electrons are moved downward of one line. This procedure is performed three times, so that the line of pixels at the bottom, which was not exposed to light and is therefore empty, acquires the electrons which were trapped in the bottom exposed line, and each exposed line receives the electrons of the line above it.

After such procedure, the same iteration is performed horizontally only on the pixels of the bottom line, shifting the trapped electrons one pixel to the right, and moving the electrons of the bottom right pixel to the ADC. The horizontal shift is performed a number of times equal to the number of pixels composing a line, so that the bottom line of the device is emptied, and the vertical shift can be performed again, beginning the readout of the following line.

Once each pixel of each line has been read out, the shutter can be opened for another exposure, acquiring a new image.

The working principle just described, used in the first implementations of CCD detectors, is prone to a series of problems, which were solved with small adaptations in the following years:

- Front illumination: In most of the early CCD detectors, and indeed in most modern cheap detectors, the conductive plates generating potential wells were positioned on the side of the silicon chip exposed to light. While transparent conductive plates can be realized, the wiring is necessarily opaque, absorbing a significant percentage of the photons impinging on the chip and limiting the efficiency. The problem is solved on high-end modern devices by employing a thin silicon chip with electrodes on the back side.

- Readout time: In the procedure described previously, it is apparent that the CCD detector spends only a fraction of time exposed to light, and remains "blind" for all the time required for the readout procedure, reducing drastically the percentage of incoming photons detected. In order to avoid this inconvenience,

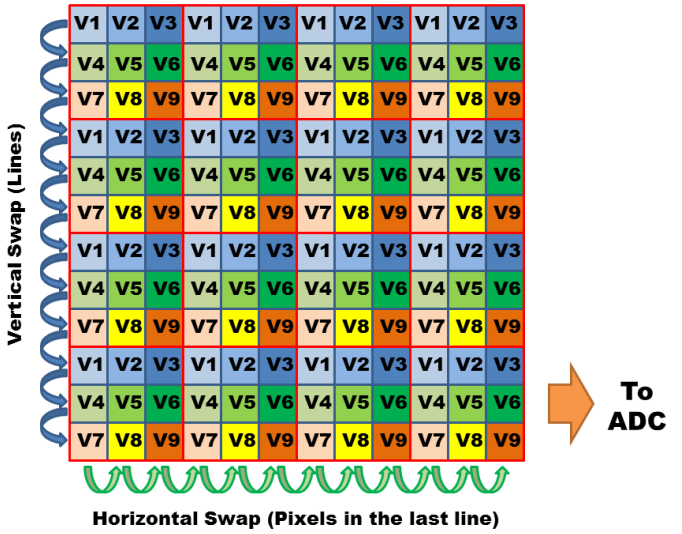

Figure 2.1.: CCD detector (4x4 pixels) working principle.

Squares represent single electrodes, kept during the exposure at voltages V9>V8>....>V1. Red lines include single pixels. During readout electrons are moved toward the bottom of the chip by swapping line voltages along the blue arrows. Each time a new line reaches the bottom, electrons are moved toward the right by swapping voltages of the last line along the green arrows.

two different chip architectures, named "frame transfer" and "line transfer" architecture, have been developed. In the frame transfer architecture, only half of the silicon chip is exposed to light. At the end of the exposure, all the pixels electrons are quickly transferred to the dark area of the chip, so that a new exposure starts immediately, while the readout procedure is carried out on the dark part of the detector. A similar procedure is applied to line transfer architectures, where exposed and darkened columns are alternated on the chip. In such an architecture, the electrons in each column are transferred on the adjacent dark column at the end of the acquisition, and readout of the dark columns is

performed during the following exposure. Both transfer methods allow to avoid "blind" times, and have the important secondary advantage of working without a slow, expensive and fragile mechanical shutter. The advantage in the use of a line transfer architecture is that the transfer time is extremely low, avoiding artifacts which may appear in a frame transfer device when bright lights irradiate the detector during the transfer procedure. On the other hand, half the image area of a line transfer device is darkened, so that a line transfer device has half the efficiency compared to equivalent frame transfer device.

- THERMAL ELECTRONS: As in all semiconductors, photoelectric effect is not the only source of electron-hole pairs formation. The other main contribution is due to thermal generated couples, which, at ambient temperature, can introduce a white noise which makes it impossible for the CCD to work in low light situations. Low light cameras are equipped with cooled CCD sensors. Cooling can be applied with a variety of methods, ranging, in order of complexity, from simple air cooling, which prevents the CCD from heating over ambient temperature, to liquid cooling, keeping the CCD at $\sim$ 10°C, to Peltier cell cooling, which can get to ~ -70°C, up to liquid nitrogen cooling ($\sim 77K$) for the most demanding applications.

- COLOR SENSITIVITY: One of the main disadvantages in the use of a CCD sensor compared to human vision, is the intrinsic capability of the human eye of spectral characterization of each "pixel". In order to achieve the same result with a CCD detector, a matrix of optical bandpass filters is deposited over the CCD pixels matrix, so that for each square of 2x2 pixels, one pixel is only exposed to blue light, one to red light and two to green light (in order to reproduce the higher sensitivity of the eye in the green part of the spectra). This way, however, the effective spatial resolution of the chip is divided by 4, and most of the photons are blocked by the filters. For low light, color sensitive applications, multiple monochromatic CCD sensors are used, diverting

different wavelengths to different detectors through dichroic mirrors. In this way the spatial resolution is preserved, and there is no loss in light efficiency due to the filters presence. Another possible solution, less expensive than a multiple CCD system, is the use of dichroic mirrors and apertures to create multiple images for different wavelengths on a single CCD chip, so that light efficiency is conserved, and only the spatial resolution of the system is affected.

- LIMITED WELL DEPTH: The charge well structure of the pixels, indeed, allows for the storage of a limited number of electrons. In case of excessive exposure, electrons tend to move, due to the well potentials organization on the chip, to vertically adjacent pixels, creating vertical stripes on the acquired image. This problem can be solved by reducing exposure times, but this would decrease the signal in darker pixels toward the noise level. The limited well depth imposes therefore a limit in contrast detection, as in a given acquisition it is not possible to simultaneously detect areas with vastly different brightnesses.

2.2. EMCCD detectors

As described in the previous section, thermal noise can be suppressed by CCD cooling. However, when increasing the clock frequency for readout, the ADC conversion becomes the predominant source of noise (readout noise), imposing a threshold in the minimum detectable light intensity. In order to reduce the effect of readout noise, the number of collected electrons should be increased. This can be achieved by increasing the exposure time, but such measure would necessarily reduce the acquisition frequency, which is often a crucial experimental parameter.

Fast frequency acquisitions in low light environments can be achieved with a different chip architecture, known as electron multiplying charge coupled device (EMCCD). The active surface of an EMCCD has the same structure of that of a standard CCD detector; the difference lies

in the darkened part of the chip used for readout. While in the standard CCD the ADC is on the extremity of the last line of pixels, in an EMCCD electrons are carried horizontally in an additional line of unexposed pixels before reaching the ADC. The clock sequence of such pixel line, while maintaining the same frequency, uses different voltages with respect to the clock sequence of the rest of the chip. In particular, for each pixel translation, electrons are moved from a charge well with low voltage to one with extremely high voltage. In high voltage electron displacement through a semiconductor, the phenomenon of impact ionization can occur, creating a number of electron-hole couples proportional to the number of electrons present in the charge well. This procedure creates an effective amplification of the signal before the stage of digital readout, so that the signal is increased, while keeping the noise constant, obtaining a dramatic increase in signal to noise ratio.

While EMCCD detectors are, at the moment, the most sensible commercially available pixelated detectors, their versatility is limited by the limited well depth of passive CCD pixels. As the readout speed, and consequently the readout noise, increases, a higher level of amplification is required. However, the maximum amplification achievable is limited by the amount of electrons storable on a single pixel, thus limiting the effective readout speed achievable. Moreover, the use of high voltage clocks on full pixels can easily damage the detector itself, so that electron multiplication voltages must be carefully adjusted during acquisition.

2.3. sCMOS detectors

In order to achieve an higher contrast range and higher frame rates, a completely different architecture can be used, based on complementary metal-oxide semiconductors (CMOS). CMOS photodetectors are arrays of integrated transistor devices, each acting as a photodetector coupled to an amplifier. The design of a single pixel can vary radically between devices (the simplest possible three transistor setup is illustrated in 2.2), but it is always based on a transistor with the gate

voltage regulated by a photodiode. At the beginning of each exposure the gate voltage is set to a baseline value, and decreases when light, impinging on the photodiode, creates a leak current. The resistance across the transistor is then evaluated, obtaining a measure of the light intensity, and the potential at the transistor gate is reset to the starting value, beginning a new exposure. Since there is no actual storage of electrons in a semiconductor, the intensity of light detectable for each exposure is only dependent on the reset voltage, thus increasing the contrast achievable, compared to CCD detectors. The readout is performed serially one row at a time. Acquisition can be performed alternating exposure and readout phases as in a CCD detector (global shutter mode), or reading one row at a time while keeping the chip exposed (rolling shutter). Rolling shutter mode allows to achieve higher frame rates, but the signal at different rows in the image are not perfectly synchronized, thus inducing image deformation artifacts when imaging fast moving objects.

The basic design of a CMOS detector was reported even before CCD cameras[11], but actual production began much later, and up to recent years CMOS detectors had inferior performances to CCD detectors, and were only used as cheaper alternatives. However, recently developed CMOS detectors, specifically developed for scientific research (sCMOS), were capable to achieve light sensitivity performances comparable to that of an EMCCD detector, while reaching much higher frame rates.

At the moment of writing this thesis, EMCCD detectors still have the best light sensitivity performances, while sCMOS detectors can achieve the highest resolutions, frame rates and contrast ranges (As an example, one of the best EMCCD on the market, the *Photometric Evolve Delta*, has 96% quantum efficiency at 550nm, with an effective readout noise $< 1e^-$ rms, and can achieve 65 fps on the full 512x512 pixels of the chip, and 1100 fps on a 16x16 pixels subregion, while one of the best sCMOS detectors, the *Hamamatsu Orca Flash 4.0*, has 70% quantum efficiency at 600nm, with an effective readout noise of $1.9e^-$ rms, and can achieve, in rolling shutter mode, 100 fps on the full 2048x2048 pixels of the chip, and up to 3200 fps on a 64x64 pixels

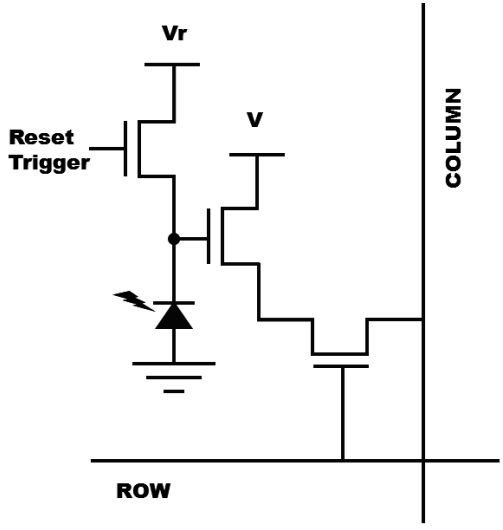

Figure 2.2.: CMOS pixel scheme.

Functional scheme of a simple CMOS pixel. Actual high performance CMOS detectors employ different and more complex circuits to minimize noise. Exposure start with a reset trigger pulse, which brings the photodiode potential to V_{reset}. As photons hit the detector during exposure, a leaking current lowers the diode potential toward the ground value. At the end of the exposure, in order to read the intensity value at the pixel, the row electrode potential is increased, and current along the column electrode is measured.

subregion.).

2.4. SPAD arrays and microchannel plates

Microscopy applications in which no spatial information is required at the detection level, as confocal and two photon microscopy or fluorescence correlation spectroscopy, can rely on a variety of light detectors which have obviously better performances in sensitivity and time resolution compared to a camera pixel. The "ideal" pixelated detector

for microscopy would indeed consist in a spatial array of miniaturized, micron scale, versions of such detectors. While semiconductor CCD and CMOS cameras are still the most versatile option for microscopy, arrays of better performing photodetectors are available.

The most sensitive detector used for "single pixel" applications is the single photon avalanche diode (SPAD), a semiconductor photodiode working at high voltages, where the absorption of a photon generates an electron-hole pair, and the electron immediately produces impact ionization, resulting in a sudden burst of current through the diode. The output of such detector is an actual photon count, producing a standard digital pulse each time a photon hits the diode, with picosecond time resolution. Since such devices are semiconductor based, the manufacturing of an array of micrometer sized SPADs is achievable. The problem, however, lies in the digital conversion of signals to images, as the amount of information gathered can be overwhelming for memory storage. Due to such problem, reported implementations of high resolution SPAD arrays[12] can only reach frame rates similar to the ones of a CMOS camera (2400 fps on 128x128 pixels). The advantage in the use of such detectors is given by the possibility to store temporal differences in photon detection between pixels in the same image. While this is widely used for macroscopic applications, such as time-of-flight 3D imaging[13], no microscopy applications of the technique have yet been reported. Lower resolution, monodimensional SPAD arrays (8 pixels linear array), have been used for parallel fluorescence correlation microscopy[14].

A less sensible, more versatile single pixel detector than the SPAD is the photomultiplier tube (PMT). PMTs consist on a photocathode and a series of dynodes at increasing voltages. Photons absorbed at the photodiode generate electrons, which are then accelerated through the potential difference to the closer dynode, where the arrival of high energy electrons generates the emission of multiple low energy electrons, which are accelerated to the next dynode. The process is repeated for each dynode, up to a final step in which electrons hit the anode of the system, and a current is detected. Due to the steps of amplification, the signal generated by a single photon can generate currents

lasting some nanoseconds, thus limiting time resolution compared to SPADs, and making photon counting feasible only in extremely low light environments. However, while limited in performance compared to SPADs, PMTs are widely used in microscopy due to their highest dynamic range and durability, and still can outperform the pixels of a CCD or CMOS camera both in time resolution and in light sensitivity.

PMTs are however difficult to miniaturize, due to the presence of the dynode amplification chain, so that PMTs arrays are not suitable for use in microscopy imaging. The device which more closely resembles an array of PMTs is a microchannel plate (MCP). MCPs are plates of highly resistive material, in which an array of micrometer-sized cylindrical holes connects the opposite sides of the plate. A photocatode is laid on one side of the plate, and a voltage is maintained between the sides of the plate, so that electrons emitted by the photocatode enter the microchannels, and the sides of the channel act as dynodes, multiplying the electrons as they move toward the anode.

MCPs where at first manufactured to reduce the time jitter of photomultipliers, with multiple short range amplifiers instead of a long series of dynodes, and they were used as a "single pixel" detector, using a single anode on the far side of the plate. While the use of an array of anodes would create digital conversion problems similar to the ones of SPAD array, MCPs can be used with a phosphors screen on the far side of the plate. This kind of device is called image intensifier, and acts as an effective photon multiplier, as when a photon is absorbed at the photocatode it is converted in a shower of electron, each of which generates the emission of photons at the phosphor screen. Photon multiplication rate can be as high as 10^6.

Image intensifiers can be coupled to CCD or CMOS cameras, dramatically increasing the effective light sensitivity of the detection process. The time resolution remains limited by the CCD or CMOS performance, but the light amplification allows the use of less sensitive devices, which can achieve higher frame rates (as an example the *PCO Dimax* camera can achieve 7000 fps on 1000x1000 pixels). For extremely high frame rates applications, the response time of the image intensifier screen must be carefully considered, as the widely used P43

phosphorous screen have response times of fractions of millisecond, which can interfere with the actual time resolution of the system, fast P46 phosphorous screens (response times on the microsecond scale) are to be preferred in this respect.

3. Neuroscience

This chapter gives a brief introduction to the physiology of the nervous system, with the basic information required in order to better understand the experiments reported in chapter 8, and a report of the most used optical microscopy techniques used in neurophysiological studies. A complete and rigorous description of this extremely complex subject is available in well known physiology manuals[15, 16].

3.1. Neuronal membrane dynamics

One of the most complex functions of the nervous system is the control of the interactions of the organism with the external world, from simple reflexes to complex behaviors. Its main activity is therefore the acquisition, elaboration, and transmission of information between other structures. Such activity should be performed in the fastest and most efficient way in order to maximize the chances of survival of the organism. To this purpose, evolution led to the development of an extremely complex network of excitable cells, called neurons, which form an intricate network of connections with each other, organized in a central elaboration unit, formed by the brain and the spinal cord, with terminations in every area of the body. Just to give an idea of the complexity of the systems, it has been estimated that the human brain contains 10^{11} neurons, each in average forming 10^4 contacts (called synapses) with other neurons. While many different types of neurons are present in the nervous system, characterized by the presence of a long termination, called axon, which can extend, depending on the neuron type, from several micrometers to a meter, and many shorter terminations, called dendrites.

The main function of neurons is gathering and elaboration of infor-

mation, which is mainly carried out through the modulation of the membrane potential. As in all cells, the different concentration of ions in the intracellular and extracellular environment, creates an electric potential difference between the sides of the cellular membrane, leading, for most neurons, at a resting state of about $-70mV$. The activity of a neuron is regulated by the opening of ion channels in the membrane, which are pore-forming proteins selectively allowing the flow of ions according to the electrochemical gradient. The transition of ion channels from an open to a closed configuration, can be regulated, depending on the nature of the channel, from the membrane potential or from the interaction with a ligand. Conversely, the opening of a channel, by locally varying the ion concentration, influences the membrane potential. The mutual interaction between the channels conformation and the membrane potential leads to complex feedback patterns, which can be extremely different between neuron types. However, all neuron types share the possibility to generate a stereotyped event, called an *action potential*(see figure 3.1).

An action potential occurs in the cell when the membrane potential increases up to a threshold, generally around $-55mV$, where voltage gated channels for Na^+ open. Since the concentration of sodium is much higher outside the cell than inside it, this causes a rapid increase in the membrane potential, up to positive values, where voltage gated channels for K^+ open and Na^+ channels close. The concentration of potassium is higher inside the cell, so that the opening of the channels abruptly lowers the membrane potential towards negative values. The action potential propagates along the axon at high speeds (up to 100 m/s) though the serial opening of voltage gated sodium channels equally spaced along the axon. At its termination the axon ramifies, and contacts other neurons by synapses, contact zones in which the axon membrane is just few nanometers distant from the other cell. When the action potential reaches the synapse location, local voltage activated calcium channels open, and the increase in calcium concentration triggers exocytosis of a neurotransmitter in the synaptic space, effectively passing information between neurons. Ligand gated channels on the other neuron can open by receiving the neurotransmitter,

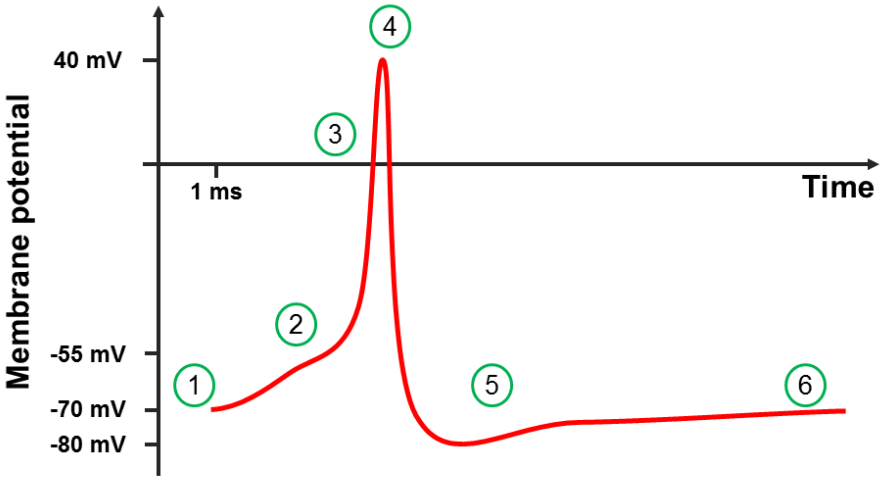

Figure 3.1.: Schematic evolution of an action potential.

1. Resting state. 2. Sodium channels opening threshold. 3. Potassium channels open. 4. Sodium channels close. 5. Refractary period. 6. Resting state.

so that the membrane potential is altered. Depending on the nature of the neurotransmitter and the channels involved, the synapse can either be excitatory, when the post synaptic cell potential increases, or inhibitory, when the post synaptic cell potential decreases.

The described event results in a fast spike in membrane potential, which lasts, in most vertebrate organisms, humans included, around one millisecond. This order of magnitude is extremely important for the study of neural networks, as the action potential is the basic event regulating the activity of the whole nervous system. An experimental setup developed for the study of neuronal networks should therefore have a time resolution of at least 1 ms, in order to acquire all the available information about the network activity.

3.2. Cerebellum

The network of neurons and synapses forming the nervous system, is hierarchically organized, forming small dedicated microcircuits, which themselves are connected creating macro-structures with specific functions in the organism. The methods developed in this thesis were employed for the study of one of the most important and complex macro-structure of the brain, the cerebellum.

The cerebellum is a part of the brain, which is traditionally believed to be responsible for motion coordination and motor learning, and has more recently been proved to be involved in cognitive processes[17].

The cerebellum is constituted by a convoluted cortex of gray matter, containing half the neurons of the whole brain, tightly packed together, surrounding a central core of white matter, mainly constituted by fibers of input and output, and containing some neurons, dedicated to the output of the signals from the cortex, called cerebellar nuclei. The fibers connect the cerebellum to several other parts of the brain, especially the motor cortex and sensory areas.

The cerebellar cortex is divided in three layers: the granular layer, closer to the core, the more superficial molecular layer, and the single cell thick Purkinje cells leyer. A scheme of the organization of the cortex is reported in 3.2. The granular layer is mainly formed by tightly packed granule cells (GCs), small cells of $4 - 5\mu m$ of diameter. Granule cells dendrites are around $50 - 100\mu m$ long, contacting fibers termination inside the granular layer, while their axons are projected into the molecular layer.

Beside granule cells, the granular layer contains the termination of input Mossy fibers, some inhibitory neurons, mainly Golgi cells, distributed among the layer.

The molecular layer has sparse presence of inhibitory neurons. Purkinje cells (PCs), the most complex neuron type of the cerebellum, have extremely ramificated planar dendritic prolongations in the molecular layer, creating multiple synapses with GC axons and input climbing fibers. The axons of PCs extend through the granular layer, and join the cerebellar nuclei, constituting the output of the cerebellar cortex.

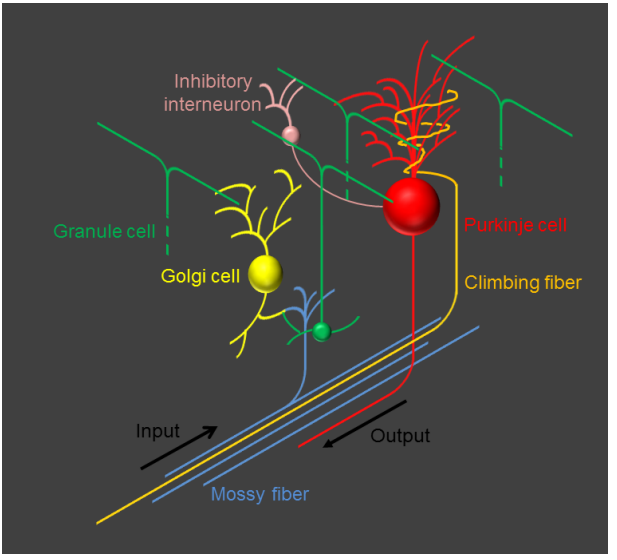

Figure 3.2.: Scheme of the cerebellar cortex.

Input is provided by Mossy and climbing fibers. While climbing fibers directly contact the dendritinc tree of Purkinje cells, Mossy fibers contact granule cells, the axons of which contact dendritic trees of Purkinje cells, Golgi cells, and interneurons of the molecular layer. Golgi cells provide inhibition at the Mossy-granule synapse. Inhibitory interneuron contact the Purkinje cells at somatic level. The axons of Purkinje cells is the only output of the cerebellar cortex.

The cerebellum can therefore be seen as a massive parallel computation unit, in which multiple input Mossy fiber contact the granular layer, the signal is elaborated in the granular layer, and integrated by PCs.

3.3. Fluorescence microscopy in neuroscience

Calcium imaging

As described in section §3.1, the activity of the nervous system is based on the variations in membrane potentials of neurons. A good and easily detectable indirect indicator of the activity of a neuron is the concen-

tration of Ca^{2+} ions in the intracellular medium. Such ions are kept, at the steady state, at a very low intracellular concentration ($10-100nM$) by active membrane channels moving the ions outside the cells and inside intracellular stores. Concentration of calcium inside the cells can be increased by the opening of calcium channels on the membrane, or by release from intracellular stores. Most calcium channels in neurons open when the cell membrane is strongly depolarized, usually during an action potential, while intracellular stores release Calcium depending on the cellular calcium concentration, so that an increase in calcium concentration can generate a further calcium release from the stores, in a positive feedback process known as *calcium induced calcium release*. The opening of calcium channels has the double function of depolarizing the membrane and increasing the intracellular concentration of calcium. These changes determine variations in the structure and function of calcium sensitive proteins, therefore altering the cell physiology.

The effect of variations in intracellular calcium concentration is important for the regulation of the activity of the neuron itself, as the calcium influx triggers the release of neurotransmitter at the synapses, and can change the long term probability of neurotransmitter release, increasing the activity of the synapse (long term potentiation) or decreasing it (long term depression), phenomena which are fundamental for the activity of the brain, being involved in memory and learning processes.

A stereotyped calcium concentration variation upon the onset of firing activity in a neuron generally consists in small variations in dendrites due to calcium channels opening, followed by a fast and uniform increase at the cell soma as the calcium store sense the small increase of concentration due to the calcium channels opening.

Calcium concentration can be easily detected through fluorescence microscopy, as a wide variety of calcium sensitive fluorescent dyes is available on the market. Such dyes are generally molecules with numerous negatively charged binding sites; when calcium binds to the dye it can change the absorption and emission spectra, generating a variation in the fluorescence intensity collected by the microscope.

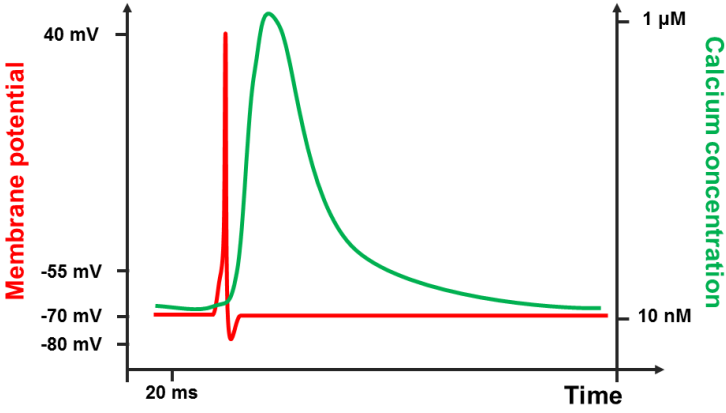

Figure 3.3.: Schematic evolution of somatic calcium concentration after an action potential.

After membrane depolarization, calcium concentration increases due to voltage gated calcium channels opening. A fast sequence of action potentials can trigger calcium induced calcium release, furtherly increasing the calcium concentration. Rising and decay times can widely vary depending on the cell type. Typical rise times in concentration are on tenths of millisecons, and decay times are on hundreds of milliseconds.

Since most calcium dyes are extrinsic organic molecules, different staining procedures are used, depending on the type of experiment required. In particular, two main procedures are generally employed: intracellular loading and bulk loading.

Intracellular loading is obtained by filling a patch-clamp pipette with an intracellular solution containing a calcium dye, and performing patch clamp on a neuron. This results in the staining of a single neuron, with high fluorescence intensity and contrast even in turbid media, and in the possibility of monitoring and controlling the electric activity of the neuron through the patch clamp pipette during the calcium signal acquisition. Given such characteristics, intracellular loading is

usually employed for the study of intracellular calcium dynamics of a single cell, acquiring signals from the axon and the dendrites during neuron activity induced externally or synaptically.

On the other hand, bulk loading consists in the perfusion of the sample with an extracellular solution containing a calcium sensitive dye, followed by rinsing in standard extracellular solution. When bulk loading is performed, part of the dye remains in the intracellular medium of most of the cells in the sample. Due to the low concentration of the dye and to the intricate connections between neurons, it is generally difficult to isolate signals from dendrites in bulk loading conditions, and this procedure is generally used to monitor the spatial organization of a network of multiple neurons by monitoring the somatic calcium concentration.

Calcium imaging is the most reliable and widespread technique for monitoring the activity of a network of neurons, and it has applications on cell cultures, tissues and in vivo in living organisms. Calcium imaging in cell cultures, or in intracellularly loaded cells in tissues, can be easily performed with epifluorescence microscopy. On the other hand, imaging in bulk loaded tissues and in vivo microscopy require high imaging depth and benefit greatly from the possibility of three dimensional acquisition, thus making two photon microscopy the most used microscopy technique in the field. However, while epifluorescence calcium imaging can benefit from the high acquisition speed of modern CMOS cameras, the speed of traditional two photon imaging is limited, and only allows to gather partial information on the network activity. In order to perform high speed acquisition in three dimensional samples, RAMP microscopy can be employed[18].

Full field, three dimensional calcium imaging on the kHz scale can be achieved in vivo with SPIM microscopy in Casper zebrafish embryos[19], a mutation of the zebrafish with no skin pigmentation, and therefore completely transparent. This is only possible in highly transparent specimens, and would not be possible on brain tissue samples, both in vitro and in vivo, due to the limitations of SPIM in imaging strongly scattering samples.

Voltage sensitive dyes

As discussed in the previous section, calcium concentration is an indirect indicator of neuronal activity. Since the basic event of neuronal signaling is the action potential, a rapid depolarization of the cell membrane, lasting about 1 ms, the ideal microscopy experiment on neurons should employ a voltage sensitive dye staining cell membranes, and a time resolution of at least 1 kHz. Voltage sensitive dyes are hydrophobic molecules with pronounced sensitivity to *Stark Shift*, the physical phenomenon which increases the energy gap between energy level of molecules in the presence of an electric field, thus shifting both the excitation and emission spectra towards shorter wavelengths. The wavelength shift obtained during an action potential is however limited to few nanometers, so that even using very thigh bandpass filters for excitation and emission light, set at the wavelength of highest variation of the spectra, variations in light detection only amount to less than a few percent, so that detection requires an extremely high S/N ratio in acquisition. The situation gets worse when employing two photon excitation, as the broad two photon excitation spectra generally do not present high steepness zones, resulting in even lower signal variations during action potentials.

A recently published variant for voltage sensing is the use of voltage sensitive proteins[20]. Such proteins show two fluorescent sites with different spectra, can be expressed in cell membranes, and vary their conformation depending on membrane potential. The two fluorescent sites of the molecule are interested by Förster resonant energy transfer, a phenomenon in which a site excited at shorter wavelengths can relax non radiatively to the ground state while exciting an adjacent long wavelength site; the probability of energy transfer between two molecules is inversely proportional to the sixth power of the distance, so that the signals of the two sites show detectable variations when the protein changes conformation. Results with VSD proteins are promising, with high variations in the ratio between emissions during depolarization, but at the moment only measurements of ensemble activity, or low frame rate detection of small variations of membrane potential have been reported[21]. No evidence of the possibility of detecting

action potentials with VSD proteins has been published yet.

Due to the need of high frame rates in order to gather significant information, VSD imaging is mainly performed with epifluorescence microscopes[22], employing high speed CMOS cameras in order to achieve kHz time resolution. This allows to visualize single action potentials in cultured cells, but due to the non confocality of the measures, VSD imaging on working neuronal networks, found in acute slices or in vivo, can only obtain ensemble activation information.

The only reported technique capable of acquiring action potentials with VSD dyes in acute slices is RAMP microscopy, performed on five cells at 2.5 kHz time resolution[23], however, the technique is not easily employable for neuroscience research, as the dye employed is not commercially available, and excitation is performed at a long wavelength, requiring an optical parametric oscillator in addition to the traditional titanium sapphire laser used for two photon excitation.

4. Hemodynamics

Most cellular types in a biological organisms can only work in a strict range of environmental conditions, with, for example, specific concentrations of molecules relevant for metabolisms, at specific temperatures, in a specific pH intervals. Moreover, the activity of tissues tends to degrade its own environment, changing molecular concentrations with reactions, producing waste products, altering pH, and changing the temperature. In order to keep the tissues in the correct environment, a continuous flow of molecules of interest is provided by blood circulation. This chapter gives a brief introduction to hemodynamics, with the basic information required in order to better understand the experiments reported in chapter 11, and a report of the most used optical microscopy techniques used in neurophysiological studies. A complete and rigorous description of this extremely complex subject is available in well known physiology and hemodynamics manuals[16, 24].

4.1. Blood composition

Blood is a colloidal solution, in which a variety of corpusculate elements are suspended in an aqueous solution of gases, ions, and organic molecules. Blood flow grants the continuous supply of important molecules, such as oxygen and nutrients, and the removal of waste products, such as carbon dioxide or lactic acid. Moreover, blood carries important cells for immunological responses, regulates pH and osmotic pressures, and regulates body temperature at the extremities.

The corpusculate part of the blood, composing around 40% of the volume of human blood, consists mainly in red blood cells, while the rest is composed by cells of the immune system, and platelets, small cellular fragments responsible for the activation of hemostatic functions,

closing lesions to the blood vessels.

Red blood cells are small discoidal anucleated cells ($\sim 5 - 10\mu m$ diameter), which main function is carriying oxygen to peripheral vessels, as the solubility of oxygen in plasma is too low to grant correct oxygenation of the organism. In order to transport oxygen, red blood cells are rich in hemoglobin, a complex protein showing exposed iron ions, which affinity to oxygen binding is affected by pH. In normal arterial blood, nearly all of the hemoglobin in the blood is bound to oxygen; as a red blood cell reaches an peripheral capillary where the concentration of carbon dioxide is higher than a threshold level, oxygen is released and transferred to the adjacent tissue.

4.2. Anatomy of the cardiovascular system

Blood circulation is provided by an intricate network of vases, in which blood is forced to flow by a pumping muscular organ, the heart. Different superior organisms have very different blood circulation systems and heart structure.

In mammals the heart is a complex muscle divided in four cavities, two atri and two ventricules; each atrium-ventricule couple forming a separate pump. The contraction of the heart muscle is involuntary and regulated by dedicated excitable cells. The pump formed by the right atrium-ventricle couple pumps blood through a short loop which ramifies in the lungs, where the blood is oxygenated, and going back to the heart at the left atrium, where the pump formed by the left atrium-ventricle couple sends it to peripheral organis.

The Vessel system in most vertebrate animals is organized in a network of arteries decreasing in diameter along the flow direction, from the heart to the peripheral organs, carrying oxygen and nutrients, and a network of veins, increasing in diameter as the flow goes from the peripheral organs back to the heart, carrying waste products and carbon dioxide. The two networks come in contact at the capillaries, the smallest vessels in the network, in which the vessel walls are permeable to gases and molecules. In the vessels, osmotic and hydrostatic pressure cooperate for the exchange of molecules to the irrorated or-

gan, transforming oxygen and nutrients rich arterial blood in waste and carbon dioxide rich venous blood.

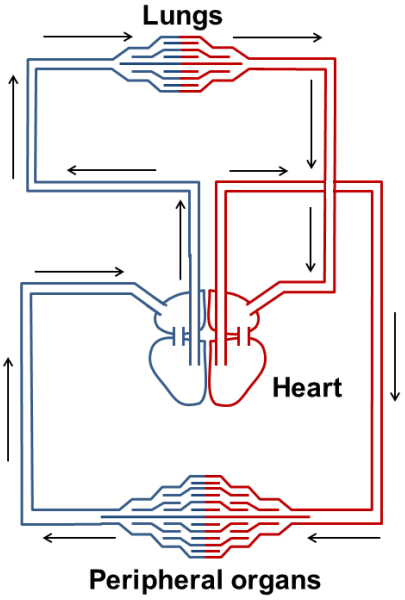

Figure 4.1.: Scheme of the human vascular system.

Veins are represented in blue, while arteries are represented in red. The right atrium-ventricle pump sends blood to the lungs, where hemoglobin is oxygenated. The blood goes back to the left atrium, and the left atrium-ventricle pump sends blood to peripheral organs.

The permeability of the vessels to substances carried in the blood is regulated by the internal vessels surface tissue, called endothelium. The endothelium is formed by regularly spaced endothelial cells, separated from the blood by a 100 nm thick layer of highly negatively charged glycoproteins. The endothelial cells are thightly packed in all vases, with intracellular spaces of around $10\mu m$, and are more spaced in thin capillaries, in order to facilitate transport. Endothelial cells are sensible to mechanical stress, produced by blood pressure and by *shear stress*, the force applied to the endothelium by the friction of flowing blood. In reaction to variations of the mechanical stress, endothelial

cells can influence through complex system of mechanotransduction, the vasomotor tone, change the permeability of the endothelium, and interact with platelets and the cells of the immune system.

4.3. Fluid dynamics

From a fluid-dynamics point of view, arterial and venous flow are fundamentally different. In arteries the flow speed is pulsed, due to the pumping action of the heart, presenting regular fast pulses of high speed flow, called systolic phases, intervalled by diastolic phases of low speed flow. The arterial flow speed decreases as the network ramifies, going, in humans, from some meters per second at the aortal artery, to few micrometers per second in the capillaries. In the veins the flow is more regular, showing a pulsate behavior only in the veins of higher diameter closer to the heart. Blood flow speed varies dramatically along the blood circulation system and between organisms.

In large arterial vessels, due to the high speed of the flow, and to complex geometrical shape of the vessels, the flow is turbulent and difficult to characterize, while it becomes laminar at the smaller, peripheral vessels and capillaries.

4.4. Zebrafish model system

The variability in the vascular system organization between species, imposes the necessity for a careful selection of an animal model system to be employed for research. The most used model for fluorescence microscopy studies is the Casper Zebrafish. The main reasons in the use of such model are the complete knowledge available of its genetic code, allowing to realize fluorescent mutants, and mutants showing cardiovascular patologies of medical interest. Moreover, the Casper variety of Zebrafish has no pigmentation, allowing optimal performances with optical microscopy techniques.

The Zebrafish vascular system is of course different in many ways from the human one, but has some interesting characteristics making it useful for research. The Zebrafish heart is formed by only two

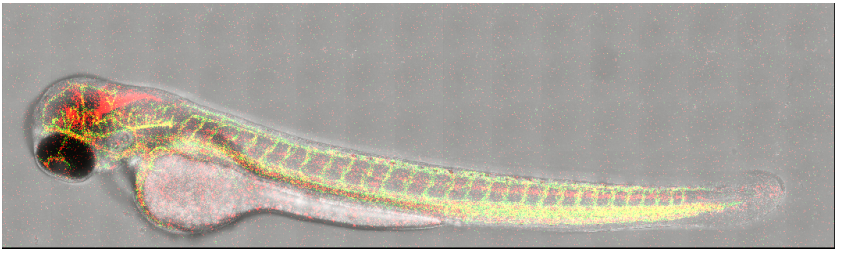

Figure 4.2.: Casper Zebrafish.

Merged confocal and brightfield image of a transgenic casper zebrafish embryo. Green channel shows gfp expressing endothelial cells. Red channel shows DsRed expressing red blood cells. The dorsal aorta and cardinal vein are veri close to each other in the lower part of the image, while the DLAV is clearly visible on the upper part of the image.

chambers, generating a flow moving in direction of the tail through a main artery, called *dorsal aorta*, and flowing back to the earth through two main veins, parallel to the aorta: the cardinal vein and the *dorsal longitudinal anastomotic vessel* (DLAV). Many short straight capillary connect the aorta with the DLAV and the cardinal vein throughout the Zebrafish body lenght[25].

The Zebrafish blood flow is particularly interesting as it has comparable heartbeat frequency with the human one, and its red blood cells, while being nucleated, have similar dimensions to the human ones. Moreover, the dimensions of the zebrafish vessels, around $30 - 50\mu m$ is comparable to the one of peripheral vessels in the human body. The main difference in the flow dynamics is given by the absence of endothelial muscolature in the zebrafish artery.

4.5. Fluorescence microscopy in hemodynamics

While imaging of neuronal activity, generally detected through variations of fluorescence on still structures, can be performed at low time resolution, at the cost of the loss of part of the information, microscopy on blood flow requires high acquisition frequencies, due to the fast motility of the sample. Given this limitation, most mi-

croscopy research in hemodynamics is performed through epifluorescence microscopy. Since blood flows are generally found only in living organisms, and therefore are three dimensionally structured in scattering material, epifluorescence microscopy is severely limited, and most studies are carried out on artificial systems in which blood samples flow through square glass capillaries. High frequency microscopy images are generally studied with particle image velocimetry, a positional tracking technique, producing a map of the flow of macroscopic objects throughout the field of view.Some in vivo applications have been reported in casper zebrafish embryos. The transparency of such samples allows PIV measurements, recently performed in three dimensions with an optical tomography setup[26].

In vivo measurements of flow, due to the slow acquisition frequencies of confocal and two photon microscopy, are generally performed through FCS[27], a statistical analysis of fluorescence fluctuations described in detail in chapter 9, giving high accuracy measurement of the flow speed in a single diffraction limited position. Recent publications report FCS measurements parallelly performed in zebrafish through SPIM microscopy[28].

Part II.

Holographic microscopy in Neuroscience

5. Introduction to spatial light modulation microscopy

This thesis proposes a novel two photon microscopy method based on spatial light modulation, which is a Fourier optics based technique allowing the generation of arbitrary light distributions on an optical plane, by manipulating the phase of the wavefront in another plane along the optical path. This chapter provides a simple theoretical background on Fourier optics, describes the principles of spatial light modulation, the algorithms used for holograms calculation, and the working principles of spatial light modulators, and finally reports the most recent applications of spatial light modulation to fluorescence microscopy.

5.1. The lens as a Fourier transformer

While a complete discussion on Fourier Optics theory can be found on a variety of excellent books[29, 1], the theory of spatial light modulation only requires one important rule, which states that, under appropriate approximations, the electric field distribution generated by a propagating monochromatic wave on the focal plane of a lens (or a lenses system), is the Fourier transform of the electric field distribution in the back focal plane. This section reports a demonstration of such theorem, with some useful considerations for spatial light modulation theory.

As in all optics problems about electric field propagation, we start with the free space version of the Fresnel-Kirchhoff diffraction integral, which, given the electric field distribution generated by a monochromatic wavefront at a plane in space, describes the field distribution at

another plane, parallel to the first one, at a distance z:

$$E(x_2, y_2, z) = \frac{e^{i2\pi\frac{z}{\lambda}}}{\lambda z} \iint E(x_1, y_1, 0) e^{\frac{i\pi}{\lambda}\frac{(x_2-x_1)^2+(y_2-y_1)^2}{z}} dx_1 dy_1 \quad (5.1)$$

where λ is the wavelength of the monochromatic wave used. The formula can be qualitatively interpreted as an evaluation of the interference at the plane in z. In order to do so, the field at (x_2, y_2, z) is evaluated by taking the field at each point $(x_1, x_2, 0)$ of the initial plane, reducing its amplitude by a factor proportional to z, in order to account for the distance (in the approximation $z \gg (x_2-x_1), (y_2-y_1)$), and adding the phase change of a wave of wavelength λ traveling for the distance between the point $(x_1, x_2, 0)$ and the point (x_2, y_2, z). It is important to notice that the correct form for the phase term should be:

$$e^{i\varphi} = e^{\frac{i\pi}{\lambda}\sqrt{z^2+(x_2-x_1)^2+(y_2-y_1)^2}} \quad (5.2)$$

taking in to account the correct distance traveled by the wave. However, such form is particularly unsuitable for integral calculations, so the system is considered in parabolic approximation:

$$\sqrt{z^2 + (x_2 - x_1)^2 + (y_2 - y_1)^2} \approx z + \frac{(x_2 - x_1)^2}{z} + \frac{(y_2 - y_1)^2}{z} \quad (5.3)$$

which is valid when $z \gg (x_2 - x_1), (y_2 - y_1)$, thus corresponding to the analytic version of the paraxial approximation used in geometric optics.

Knowing the Fresnel-Kirchhoff integral, it is virtually possible to find a solution to any propagation problem. In particular we are interested in what happens in the focal plane P_f of a thin lens, knowing the electric field distribution at plane P at a distance z on the other side of the lens. In order to do so, we should use the Fresnel-Kirchhoff integral to calculate the propagation of the electric field $E(x, y)$ in the plane P to the lens plane P_l at a distance z, than add the phase shift $e^{i\varphi_l(x',y')}$ due to the presence of the lens thus finding the field after the lens $E_l(x', y')$, and than propagate such field to the plane P_f, obtaining the desired field $E_f(x'', y'')$. The procedure is illustrated in figure 5.1

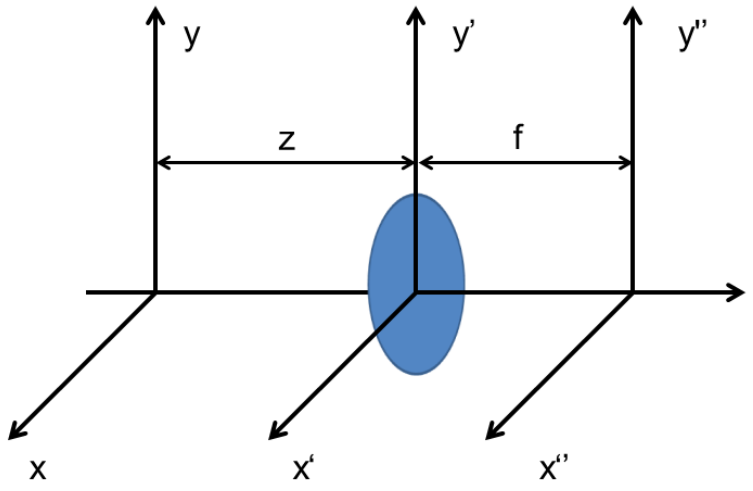

Figure 5.1.: Cross correlation fit function

Scheme of the procedure applied to calculate the effect of a lens on the propagation of the electric field. the field at the plane (x,y) is propagated through equation (5.5) to the plane (x',y'), then the lens phase pattern is summed, and the obtained field is propagated to the plane (x",y").

For a spherical lens of focal length f, supposing it has infinite aperture, the phase shift term can be approximated as:

$$\varphi_l(x', y') = -\frac{x'^2 + y'^2}{\lambda f} \tag{5.4}$$

Therefore, propagating the field at P to the lens plane we obtain:

$$E_l(x', y') = \frac{e^{i2\pi\frac{z}{\lambda}}}{i\lambda z} \iint E(x, y) e^{i\pi\frac{(x'-x)^2+(y'-y)^2}{\lambda z}} e^{-i\pi\frac{x'^2+y'^2}{\lambda f}} dxdy \tag{5.5}$$

and with the last stage of propagation:

$$E_f(x'',y'') = \frac{e^{i2\pi\frac{f}{\lambda}}}{i\lambda f}\iint E_l(x',y')e^{i\pi\frac{(x''-x')^2+(y''-y')^2}{\lambda f}}dx'dy' \tag{5.6}$$

.

With some straightforward calculations, we obtain:

$$\begin{aligned} E_f(x'',y'') &= \frac{e^{i2\pi\frac{z+f}{\lambda}}}{-\lambda^2 fz}e^{i\pi\frac{x''^2+y''^2}{\lambda f}}\iint dxdyE(x,y)e^{i\pi\frac{x^2+y^2}{\lambda z}} \\ &\iint dx'dy'e^{i\pi\frac{x'^2+y'^2}{\lambda z}}e^{-i2\pi\left[\frac{x'}{\lambda}(\frac{x}{z}+\frac{x''}{f})+\frac{y'}{\lambda}(\frac{y}{z}+\frac{y''}{f})\right]} \end{aligned} \tag{5.7}$$

.

It must be noted that the term

$$\iint dx'dy'e^{i\pi\frac{x'^2+y'^2}{\lambda z}}e^{-i2\pi\left[\frac{x'}{\lambda}(\frac{x}{z}+\frac{x''}{f})+\frac{y'}{\lambda}(\frac{y}{z}+\frac{y''}{f})\right]} \tag{5.8}$$

is the Fourier transform of $e^{i\pi\frac{x'^2+y'^2}{\lambda z}}$ with respect to the coordinates $u = \frac{1}{\lambda}\left(\frac{x}{z}+\frac{x''}{f}\right)$ and $v = \frac{1}{\lambda}\left(\frac{y}{z}+\frac{y''}{f}\right)$. We must now use one of the basic principles of the Fourier transforms, which states that the Fourier transform of a Gaussian term is another Gaussian, with a width which is inversely proportional to the one of the original Gaussian. The bidimensional version of such rule can be written as:

$$F(e^{-\pi(a^2x^2+b^2y^2)}) = \frac{1}{ab}e^{-\pi(\frac{u^2}{a^2}+\frac{v^2}{b^2})} \tag{5.9}$$

In our case $a = b = \sqrt{\frac{i}{\lambda z}}$, so that the expression for the electric field at the focal plane becomes:

$$\begin{aligned} E_f(x'',y'') &= \frac{e^{i2\pi\frac{z+f}{\lambda}}}{\lambda f}e^{i\pi\frac{x''^2+y''^2}{\lambda f}} \\ &\iint dxdyE(x,y)e^{i\pi\frac{x^2+y^2}{\lambda z}}e^{-i\pi\frac{z}{\lambda}\left[(\frac{x}{z}+\frac{x''}{f})^2+(\frac{y}{z}+\frac{y''}{f})^2\right]} \end{aligned} \tag{5.10}$$

which, with straightforward calculations leads to:

$$E_f(x'',y'') = \frac{e^{i2\pi\frac{z+f}{\lambda}}}{\lambda f} e^{i\pi\frac{x''^2+y''^2}{\lambda f}(1-\frac{z}{f})} \iint dxdyE(x,y)e^{-i2\pi\frac{xx''+yy''}{\lambda f}} \tag{5.11}$$

.

Where the last integral is the Fourier transform of $E(x,y)$ with respect to the coordinates $\frac{x''}{\lambda f}$ and $\frac{y''}{\lambda f}$.

In the particular case in which $z = f$, which corresponds to the propagation of the electric field distribution in the back focal plane, the second exponential vanishes, leading us to the form:

$$E_f(x'',y'') = \frac{e^{i4\pi\frac{f}{\lambda}}}{\lambda f} \iint dxdyE(x,y)e^{-i2\pi\frac{xx''+yy''}{\lambda f}} \tag{5.12}$$

where the first exponential is a constant phase term, which can be neglected, the denominator is an amplitude modulation accounting for the distance traveled by the wave, and the last integral is the Fourier transform of the original field distribution, as we intended to demonstrate.

It is important to notice that the Fourier transform coordinates are depending on the parameters f and λ. While the dependence on f is just a consequence of the magnification of the optical system, the wavelength dependence of the magnification is an important factor, which needs to be accounted for in the design of a spatial light modulation setup.

Another important observation must be done about the effect of apertures: this chapter will describe a method for the creation of arbitrary light patterns at the focal plane of an optical system, based on the Fourier transform rule just introduced. While limitations to the system resolution and field of view due to the optical system apertures still remain, it is obvious that modulation of the electric field in the back focal plane of the system can only be performed in practice on a limited area, and with a limited spatial resolution.

According to the Nyquist theorem, the resolution of a function limits the spatial extent of the Fourier transform (or in the case of optics the field of view), while the spatial extent of the function limits the resolution of the Fourier transform. In order to further study the problem, we consider, in one dimension for the sake of simplicity, the Fourier transform of a "box" function $A_d(x)$ of size d:

$$\begin{cases} A_d(x) = 1, & -d/2 < x < d/2 \\ A_d(x) = 0, & x < -d/2 \vee x > d/2 \end{cases} \tag{5.13}$$

The Fourier transform of $A_d(x)$ is the *sinc* function:

$$F\left[A_d(x)\right] = sinc(d * u) = \begin{cases} 1, & u = 0 \\ \frac{sin(du)}{du}, & u \neq 0 \end{cases} \tag{5.14}$$

which is a function peaking in $u = 0$, and which goes to zero symmetrically in $u = \pm\frac{1}{d}$. This is the one dimensional version of the airy disk which limits resolution in optical systems, and a common approximation of its width, used as a limit for resolution, is $\frac{1}{d}$. In the case of a lens Fourier transform, the Fourier coordinate u is $\frac{x''}{\lambda f}$, therefore, using an optical system of focal f in order to transform a constant electric field extending over a region of size d, we would obtain a *sinc* shaped profile of width d':

$$d' = \frac{\lambda f}{d} \tag{5.15}$$

.

In order to illuminate the smallest possible area, a constant electric field over the widest possible area must be used in the back focal plane; therefore if we can modulate the field over an area of size D, the size of the smallest illumination point at the focal plane (and therefore the resolution of the system) will be:

$$d_0 = \frac{\lambda f}{D} \tag{5.16}$$

.It is important to consider that if D is exactly equal to the size of the

lens back aperture, we find (an approximation of) the Abbe law for resolution:

$$d_0 \approx \frac{\lambda}{2N.A.} \tag{5.17}$$

while if D is bigger than the objective back aperture, the modulation applied to the field at coordinates outside the back aperture will be discarded, and therefore it will be irrelevant for the shape of illumination at the focal plane. If D is smaller than the size of the back aperture, the maximum resolution of the system will be limited by the extent of the modulation area, being effectively unable to reach the theoretical performance of the lens.

As for the field of view, the larges possible illumination area at the focal plane is achieved by using a point like source at the back focal plane. If the field modulation at the back focal plane is, like in practical cases, operated over pixels of size d_{pixel}, we obtain a maximum field of view of size:

$$D_{fov} = \frac{\lambda f}{d_{pixel}} \tag{5.18}$$

which should be carefully considered in the design of a spatial light modulation optical setup.

5.2. Phase shaping

In the previous section it was established that the lens acts as a Fourier transformer for monochromatic waves between the back focal plane and the focal plane. In an ideal system, in order to obtain a desired illumination pattern in the focal plane, the inverse Fourier transform of such pattern would be computed, and the electric field would be modulated accordingly in the back focal plane. However, in applications such as two photon fluorescence microscopy in biological samples, laser power is a limited and precious resource, and since amplitude modulation of the field can only be performed by attenuating the total power, phase only modulation is generally preferred. Since the modulation is generally performed digitally in a defined area, with a defined number of pixels, in order to generate a desired pattern, a value of the phase shift

should be computed for each pixel of the light modulator. The matrix of phase shifts is called a phase mask.

The next section will describe iterative algorithms which allow to compute phase masks in order to generate any arbitrary intensity distribution in the focal plane. However, for some particular operations, some analytic patterns, described in this section, can be applied without the need for complex algorithms.

Fresnel lenses

equation (5.12) proved that the field distribution $E_{focus}(x'', y'')$ in the lens focal plane is the Fourier transform of the field distribution $E(x, y)$ at the back focal plane. The addition of an arbitrary phase pattern $\phi(x, y)$ is performed by multiplying the field $E(x, y)$ to a phase exponential so that:

$$E_{modulated} = E(x, y)e^{i\phi(x,y)} \tag{5.19}$$

, for the well known convolution theorem, the Fourier transform of the product of two functions is the convolution between the Fourier transforms of the two functions. In the case of the lens Fourier transform, the field at the lens focal plane becomes:

$$E_{focus,modulated}(u, v) = \iint F_{u',v'}\left[E(x, y)\right] F_{(u-u'),(v-v')}(e^{i\phi(x,y)})du'dv' \tag{5.20}$$

,with $u = \frac{x''}{\lambda f}$ and $v = \frac{y''}{\lambda f}$.

Let's now use a phase pattern similar to the one introduced by the presence of a spherical lens. Such pattern is called a Fresnel lens, and has a phase equal to:

$$\phi_{fl}(x, y) = 2\pi\frac{(x^2 + y^2)}{\lambda f^2}a \tag{5.21}$$

For the same Gaussian Fourier transform rule used to obtain equa-

tion (5.10), the field at the lens focal plane becomes:

$$E_{focus,modulated}(u,v) = \frac{\lambda f^2}{a} \iint_{-\infty}^{+\infty} F_{u',v'}\left[E(x,y)\right] e^{i\pi\frac{\lambda f^2}{a}\left[(u-u')^2+(v-v')^2\right]} du'dv' \quad (5.22)$$

which, changing variables to (x'', y'') becomes:

$$E_{focus,modulated}(x'',y'') = \frac{f}{\lambda a} e^{i4\pi\frac{f}{\lambda}} \iint E_{focus}(x''',y''') e^{i\pi\frac{1}{\lambda a}\left[(x''-x''')^2,(y''-y''')^2\right]} dx'''dy''' \quad (5.23)$$

. The obtained equation is the exact expression for the propagation of a field equal to$E_{focus}(x'', y'')$ placed in a plane at a distance from the lens $D = f - a$, propagated to the focal plane through equation (5.5). This means that the presence of a Fresnel lens pattern shifts the plane in which the Fourier transform is operated of a distance a, Allowing to move the focal plane without moving the lens.

Prism function

Another useful, well known, phase pattern, is the prism pattern, where the added phase is proportional to a spatial coordinate. It can be expressed as:

$$\varphi_{prism}(x,y) = 2\pi bx \quad (5.24)$$

As in the case of the Fresnel lens, we consider a field at the back focal plane equal to

$$E_{modulated} = E(x,y)e^{i\varphi_{prism}(x,y)} \quad (5.25)$$

. Again, the field at the focal plane will be the convolution of the Fourier transform of $E(x, y)$, and the Fourier transform of the phase

exponential:

$$E_{focus,modulated}(u,v) = \iint F_{u,v}\left[E(x,y)\right] F_{u,v}(e^{i\phi_{prism}(x,y)})dudv \tag{5.26}$$

. In this case the result is much easier to obtain, as the Fourier transform of $\varphi_{prism}(x,y)$ is a Dirac delta centered in $u = b$. The field at the focal plane, after adequate variables change becomes:

$$E_{focus,modulated}(x'',y'') = E_{focus}(x'' - \frac{\lambda b}{f}, y'') \tag{5.27}$$

so that the introduction of a prism pattern actually performs a linear translation of the field at the focal plane. The result could be interpreted intuitively, as a linear variation in phase could be easily produced by the presence of a mirror forming an angle with the optical axis. When a mirror is put in the back focal plane of a system, and it is tilted, the illumination at the focal plane is moved linearly. This principle is used in galvanometric scanners, employed in confocal and two photon microscopy (see section §1.3 and section §1.5).

5.3. Phase mask computation

Most of the time, when more than one focal point is required, the desired pattern of illumination is not one of the specific cases discussed in the previous section, and therefore the corresponding phase mask can not be calculated analytically. In all of those cases, the phase mask can be computed with analytic approximations or iterative algorithms. An extremely clear and complete review by Spalding et Al. of all the most used algorithms is available[30]. In this section a short description of the most used alternatives is reported, evaluating the advantages and disadvantages in the use of each type of algorithm.

Random mask algorithms

The analytic patterns described in the previous section allows the calculation of the phase mask necessary to generate with high efficiency a single diffraction limited focal point at coordinates (x, y, z). A very simple and fast way to obtain a number N_{focus} of focal points with N_{pixel} pixels available, is the calculation, for each pixel, of the analytic value of the phase mask, in that pixel only, for one of the N_{focus} focal points chosen randomly. With such algorithm, each focus will be created by the interference of the light coming from N_{pixel}/N_{focus} pixels of the modulator. It is quite straightforward that the performance of the algorithm decreases extremely fast when the number of focuses increases. In particular, increasing the number of focuses, the light efficiency decreases dramatically, and an uniform illumination is obtained throughout the field of view, with small local maxima at the focal points locations. While such situation is reasonable for applications like optical trapping or digital holography, the laser power requirements for two photon fluorescence excitation make this kind of algorithm unsuitable for the application described in chapter 6.

Superposition algorithms

Another possible approximate procedure is the use of superposition of patterns. In this case, the complete analytic phase mask for each focus is calculated, and the resulting phase mask is computed as the sum of all the phase exponential representing each mask. Due to the superposition principle for electromagnetic fields, a sum of all the fields should generate all the focuses with the maximum efficiency, but in this case, only the phase terms are being summed, while the intensity remains Gaussian. Due to interference principles, when summing multiple Gaussian fields with different phase masks, the total intensity will not be Gaussian anymore.

Such an approximation leads to an acceptable efficiency in addressing the light in the desired focuses positions, but very high differences in the light intensity at each focus are present. Moreover, with highly symmetric focuses patterns, many undesired focuses are created. As

the application described in chapter 6 requires the generation of highly symmetric patterns, this kind of algorithm should not be used.

Fourier transform based Gerchberg Saxton algorithm

The most used algorithms for phase masks calculation are variation of the one published by Gerchberg and Saxton in 1972[31]. The classic algorithm is based on iterative calculations of Fourier transforms and inverse Fourier transforms.

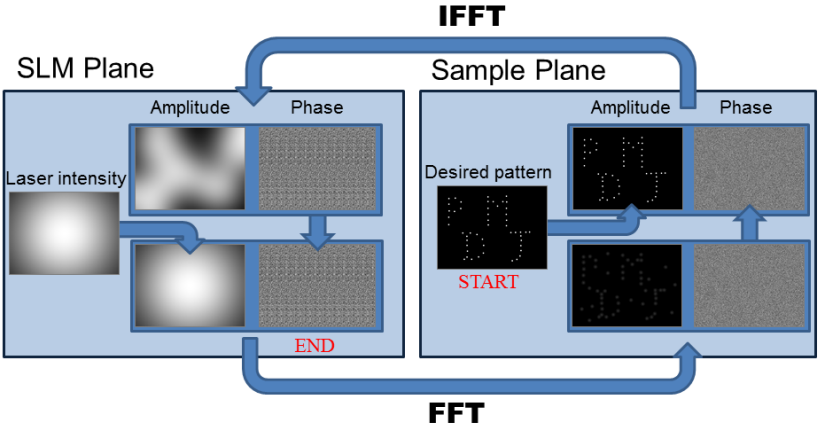

Figure 5.2.: Classic GS algorithm

Standard form of the Gerchberg-Saxton algorithm.

In order to calculate the phase mask, the algorithm, as illustrated in figure 5.2, starts with the desired intensity pattern with a random phase distribution. The inverse Fourier transform is computed, obtaining an ideal pattern at the back aperture, with an intensity distribution different from the Gaussian one of the laser beam used in practice. The phase distribution of such pattern is conserved, while the intensity distribution is substituted with a Gaussian. This pattern is Fourier transformed, obtaining a pattern at the focal plane which is similar to the one desired, but with low efficiency and several defects. The phase

distribution of such pattern is kept, while the intensity is replaced with the desired pattern, and the inverse Fourier transform is computed again, starting a new cycle. The algorithm slowly converges to a field distribution with Gaussian amplitude at the back aperture, which will generate the desired pattern with high efficiency and uniformity at the focal plane.

Since a variety of extremely efficient and optimized Fourier transforms algorithms for matrices are available, this kind of algorithm can be run in very short times (milliseconds) by desktop computers, however the algorithm has some limitations, as it can only realize bidimensional patterns, as opposed to the three dimensional patterns achievable with the previously described algorithms. Moreover, since the algorithm works on matrices of pixels, the minimum dimension of the input matrix should be at least equal to the light modulator resolution. However, the accuracy in points positioning is limited to the number of elements of the input matrix. In order to precisely position the focal points, the horizontal dimension of the input matrix should be higher than the ratio between the field of view dimension and the diffraction limit, thus increasing the computation time required.

Local field calculation Gerchberg Saxton algorithm

A three dimensional, more precise variation of the Gerchberg-Saxton algorithm, is its local field variant. Instead of calculating the Fourier transform of the field at the back aperture, the interference of the field is calculated, only at the focuses locations, with a discrete version of equation (5.5). The quality of the distribution obtained, necessary in order to decide when to stop the computation, is determined by evaluating the intensity at the focuses locations, which should be uniform between focuses, and sum up to the total intensity of the field at the back focal plane. The back propagation, instead of using an inverse Fourier transform, is performed by reversing the variables in equation (5.5), considering a starting field of point-like sources at the focuses locations, with the phases obtained by the local field calculation.

This kind of algorithm is slower than the Fourier transform based version, but it is still reasonably fast for a low number of focuses, and allows three dimensional positioning of focuses at extremely accurate positions.

Direct search algorithms and simulated annealing

In order to calculate a near-perfect phase mask, brute-force pixel variation methods can be used. In this case, a starting phase mask is generated with one of the previously described algorithms. An error function is defined, describing numerically the difference between the pattern generated by the phase mask and the desired pattern. The values of random pixels of the phase mask are then varied randomly, and the new value of the error function is computed. In direct search algorithms the change in pixel value is kept if the error is lowered, or rejected if the error increases, and the cycle goes on until a sufficiently low value of the error function is reached. This approach, while significantly slower than the previously described algorithms, leads to extremely accurate phase masks. However, there is the possibility that a direct search algorithm will lead to a local minima, and a low enough value of the error function is never reached.

To limit the occurrence of this kind of situation, simulated annealing algorithms can be used. The procedure is the same of direct search, but a change increasing the error can be accepted, with a probability decreasing dynamically in successive cycles of the algorithm. This measure dramatically reduces the possibility of the algorithm to converge in a local minimum, but furtherly increases the computational cost of the procedure.

Direct search and simulated annealing algorithms are the ones generating the best possible phase masks, and are especially needed when the desired pattern is a continuos distribution, instead of a distribution of single focuses of identical intensity. Their computational cost, however, makes it impossible to use them to calculate phase masks in real time. Their use is therefore suitable only for the calculation of fixed, pre-generated phase mask.

5.4. Phase only spatial light modulators

The previous sections of this chapter describe the theoretical procedures necessary for phase only spatial light modulation. In order to translate all of this in practice, a programmable pixelated device changing the phase of light at every pixel, called spatial light modulator (SLM) is necessary, and it should be placed in the back aperture of the optical system.

The most used technology is based on nematic liquid crystals devices, schematically represented in figure 5.3. A nematic liquid crystal, is an organized transparent fluid where molecules are aligned in a given direction. This kind of material is strongly birefringent, as when light passes through it, its refractive index remains constant for the component perpendicular to the direction of the molecules, while effective refractive index for the parallel component is depending on the rotation of the crystal along the light propagation axis. A liquid crystal spatial light modulator is a device in which a nematic crystal is deposited on a reflective array of electrodes, with molecules aligned parallel to the electrodes surface, and protected on the opposite surface by a glass layer with an array of transparent electrodes on it. Such a device modulates the phase of polarized monochromatic light passing through the nematic surface and reflected by the reflective bottom surface. The polarization of incoming light must be parallel to the direction of the nematic molecules.

As a potential difference is applied to a pixel, which is formed by the couple of a transparent electrode and the reflective electrode on the other side of the crystal, the nematic molecules tend to align with the electric field, rotating around an axis perpendicular to both the light polarization direction and the light propagation direction. The angle of rotation is proportional to the applied potential, therefore the potential directly influences the index of refraction of the crystal, and the phase of the reflected wavefront.

This kind of device can achieve phase shifts up to 2π even on near infrared light, but requires a careful design of the optical setup. Light must be generated by a coherent monochromatic source, and it must

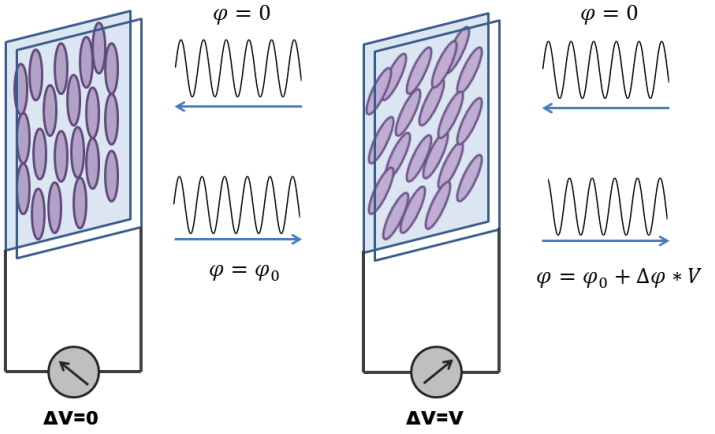

Figure 5.3.: Nematic spatial light modulator working principle.

Action of a single pixel of a nematic spatial light modulator on an incoming monochromatic wave. When a potential ΔV is applied to the opposite sides of the nematic crystal, the molecules rotate, changing the refractive index. This induces a phase shift proportional to the applied potential.

have polarization direction parallel to the one of the nematic crystals. Moreover, the angle of incidence on the modulator should be as small as possible, in order to minimize the fraction of light moving through two adjacent pixels.

Another problem is given by the position of the back focal plane of the optical system. When using an SLM for digital holography, a single plano-convex lens of fairly long focal length can be used, but for microscopy application the Fourier transform is generated by a microscope objective with very short focal length (some mm), which has a back focal plane extremely close to its back side, and in some cases geometrically inside the objective itself. In such a situation, it is

impossible to position a reflective spatial light modulator in the back focal plane.

In order to solve this problem, a three lenses system must be used, with two plano-convex lenses between the spatial light modulator and the objective. The first lens is placed at a distance equal to its focal length from the SLM, so that the desired pattern is generated on its focal plane. The second lens is placed at a distance equal to its focal length from the previously generated pattern, thus forming with the first lens a Galilean telescope. The second lens generates the Fourier transform of the desired pattern, which due to Fourier transform properties is equal to the field at the SLM surface, in its focal plane, where the back focal plane of the objective should be located.

This arrangement makes it possible to use an SLM with a short focal lens such as a microscope objective, and has the added advantage of adding a magnification to the phase mask equal to the ratio between the focal lengths of the telescope, so that, with a carefully selected couple of lenses, it is possible to perfectly fill the objective back aperture, thus maximizing the resolution and the field of view, as explained in section §5.1.

5.5. State of the art in SLM microscopy

As discussed in the previous section, RAMP microscopy can achieve kHz sampling frequency on multiple points, but the intrinsic serial nature of the detection limits the maximum number of points detectable in a given time window. A higher number of points can be monitored if they are illuminated simultaneously by multiple diffraction limited focal volumes, and detecting their signals through a pixelated detector. Simultaneous illumination over multiple positions ca be realized through a SLM.

Reported microscopes of this kind[32] consist in a modified two photon laser scanning microscope, with an additional pixelated detector, and an SLM in an optical plane conjugated by a telescope to the position of the galvanometric mirrors (figure 5.4), thus granting the possibility to acquire a standard two photon image (with a uniform SLM

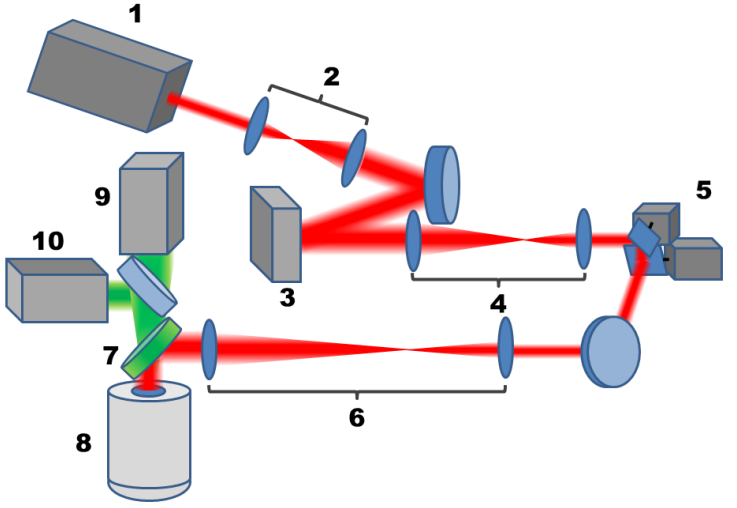

Figure 5.4.: Scheme of an holographic setup, based on a modified standard two photon microscope.

1. Ti:Sa Laser 2. Beam Expander 3. Spatial Light Modulator 4. Telescope 5. Galvanometric Mirrors 6. Scan Head 7. Dichroic Mirror 8. Microscope Objective 9. Phototube 10. Camera

pattern and moving the mirrors) and illuminating the sample on user selected points of interest (using the SLM to generate the excitation pattern and keeping the mirrors in a fixed position).

The typical experimental procedure with this kind of setup consist in the acquisition of a two photon image, the selection of points of interest throughout the image, and the simultaneous illumination through the SLM of such points, while acquiring fluorescence signals through the camera.

The points selection procedure, however, is not straightforward, as the input space of the hologram generation and the two photon images produced by the galvanometric scanner are on different systems of coordinates, and a complex calibration procedure is required before each experiment[33].

Probably due to this intrinsic complexity in the use of such device, while proof of principle applications have been published some years ago, the technique has never since been used for high speed imaging measurements in biological research, and its use has remained limited to photolysis of caged neurotransmitter, an application which does not require high precision in the positioning of focal volumes.

Aim of this thesis is the design and application of an alternative holographic microscopy setup and procedure, aimed at the realization of a completely digital two photon microscope, capable of acquiring two photon images through the only use of the SLM, and of positioning holographic focal points with sub-micrometer precision. A theoretical discussion of the techique is reported in chapter 6, the description of the realized setup is reported in section §7.1, and result of physiological interest obtained with such setup are reported in chapter 8.

6. Holographic multiphoton multifocal microscopy

This chapter describes a procedure for the acquisition of two photon images through the use of the SLM, thus enabling precise selection of points of interest without the need of calibration procedures. Moreover, by avoiding the use of galvanometric mirrors for scanning, a completely digital setup can be employed, thus dramatically reducing the complexity of the optical layout.

6.1. Basic principles

As described in section §5.2, an SLM based microscope can precisely position an excitation focal volume in the field of view, using a prism phase mask. It would therefore be possibile to perform a raster scan, as in a standard two photon microscope, by using a sequence of phase masks, and detect light with a photomultiplier, thus creating a confocal image. However, even if theoretically possible, the procedure would be extremely slow, due to the limited refresh rate of commercially available SLMs. The procedure can be sped up through parallel raster scanning, in which instead of a single focal volume, a grid of volumes is generated on the sample. This of course requires multiple detectors in order to separate fluorescence signals from different focal points. However, for the detection of multiple signals, an holographic setup already has to be equipped with ah high performance pixelated detector, which can acquire an image sequence during the SLM grid scan, and separately acquire the fluorescence intensity from every focal point of the grid in every frame of the sequence.

6.2. Scanning patterns

The acquisition of a single confocal image with a SLM based setup is performed by scanning a grid of focal points in a raster pattern. The raster scan is obtained projecting a sequence of pre calculated holograms on the SLM, showing the same grid of points in different positions. A scanning grid is characterized by several parameters, which must be optimized in order to obtain the best performances from the system. The main parameters to optimize are:

- The number of total focal points: a large number of focal points allows to scan a field of view in a small number of frames, however the total power of the laser is limited, especially at longer wavelengths, thus limiting the number of total focal points to a few hundreds.

- The distance between focal points: with a given number of focal points, the distance between the spots makes it possible to scan a small field of view in a small number of frames, or a larger field of view with a longer sequence of holograms. However, the maximum field of view is generally determined by the camera chip size and by the detection optics. On the other hand, if the spots become too close to each other, it could become difficult to discriminate their intensities, especially in highly scattering samples, where the diffusion of fluorescence light in the tissue makes the dimension of the spot's image on the camera much larger than the actual spot size.

- The number of frames in the sequence: once the number of focal points and their distance is defined, the number of frames of the sequence determines the spatial sampling of the resulting image. Since the system is diffraction limited, the ideal sampling is 2-3 pixels per points spread function, as an higher sampling would not give any additional information. However, since most commercial SLMs have a limited refresh frequency (usually 60 Hz), it is reasonable to lower the sampling to 1 pixel per point spread function or less, in order to obtain images faster.

Obviously different applications require different grid parameters. Since the uniformity of spots intensities is very important for a good image reconstruction, each hologram requires an high number of GS iterations (the ones used for the measurements showed in this thesis were obtained with 150 GS iteration, leading to an average uniformity >90%), therefore a set of scanning grid with different parameters must be calculated and stored for use, as it is impractical to calculate a new sequence during an experiment.

In the case of the calcium imaging experiments performed in this thesis, a bright two photon dye (Fura-2 AM) was used to stain an highly scattering sample (cerebellar slices), while the largest possible field of view was required, in order to record the activity of as many cells as possible. Such experimental conditions require a large grid of distant points, while the number of focal points can be fairly high, due to the brightness of the dye. Three separate grid sequences were computed, one for fast low resolution imaging, one for standard point selection purposes, and one for slow, high resolution imaging. Grid parameters are reported in table 6.1.

	Points number	Points distances (20x objective)	Resolution	Field of view	Frames number (Time)
Fast scan	28 x 28	dX=8.48 μm dY=11.58 μm	336x336	246x336 μm^2	144 (2.4 s)
Points selection	30 x 30	dX=7.09 μm dY=9.67 μm	600x600	220x300 μm^2	400 (6.7 s)
High resolution	25 x 25	dX=9.31 μm dY=12.69 μm	1000x1000	242x330 μm^2	1600 (26.7 s)

Table 6.1.: Scanning grid settings used in the reported calcium imaging experiments.

6.3. Image reconstruction

The grid scanning described in the previous section provides uniform two photon excitation over the defined field of view in a time window of a few seconds. The simplest way to acquire an image is to synchronize the detector exposure time with the entire length of a sequence. With this kind of procedure the output of the detector is already an image of the sample, but the quality of the image is deteriorated when imaging deep focal planes in scattering samples, as the scattered fluorescence

light coming from single points spreads over a wide area of the sample. Nonetheless, for simple visualization of the sample or focal plane selection, this procedure, called live imaging, combined with the use of a short, low resolution scanning sequence, proves useful, as it can generate a stream of low quality images of the sample at a relatively high speed (2 frames per second, in the reported experiments).

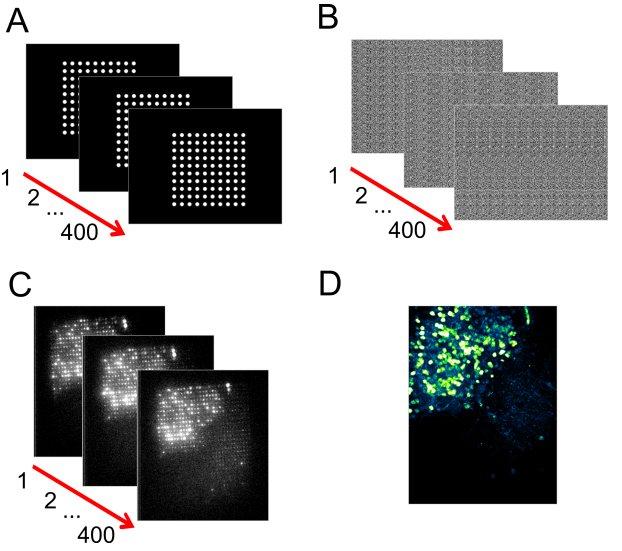

Figure 6.1.: Scheme of the image acquisition and reconstruction procedure.

A. A set of square grid patterns covering the entire scanning area in a raster-scan sequence is generated and **B.** the corresponding holograms are computed with the Gerchberg-Saxton algorithm. The series of holograms is shown on the SLM surface, and the resulting wavefront is projected on the sample. **C.** An image of the sample is acquired for every frame of the sequence, and the fluorescence of each excitation volume is stored. **D.** The stored fluorescence signals are converted in grayscale values and assigned to the corresponding pixels of the reconstructed image. The numbers in A, B and C indicate the frame index.

In order to acquire high quality images, with a much lower scattering contribution, each frame of the raster scan has to be acquired

separately, and the fluorescence intensity at each focal point location has to be gathered separately, and stored as the value of a pixel of the resulting image. A schematic illustration of the procedure is reported in figure 6.1. The spatial sampling of these images will then be determined not by the resolution of the detector, but by the number of focal points in the scanning grid and by the number of images in the sequence.

In order to separately store the intensity at each focal point, the expected position of the focal points image on the detector must be known before acquiring the sequence. Such positions can be easily determined by acquiring a single scan sequence on an uniformly fluorescent sample, and finding the local maxima in the images acquired. Once the positions of the maxima have been stored, images of the sample are realized by assigning to each pixel the total light intensity in an user defined area around the correspondent spot location. Since two photon fluorescence is a non linear process, and all of the fluorescence light is generated in a diffraction limited focal volume, it is reasonable to integrate fluorescence signal from the largest possible area, in order to exploit even scattered photons. However, as the sample is illuminated in a grid of equally spaced focal points, cross talk between focal volumes can generate ghosting artifacts in the resulting image. As a rule of thumb, with bright fluorophores, the best results are obtained with a small integration area (usually 3x3 pixels, covering an area of 19.5x19.5 μm^2 on the detector), which should only be increased if the signal is too low.

Three dimensional imaging

In standard two photon microscopy, a three dimensional image of the sample can be obtained by acquiring multiple two dimensional images on different focal planes. The focal plane is selected by axially moving the objective through a piezoelectric actuator. Piezoelectric focal shift can be easily applied in a spatial light modulating two photon microscope. The holographic nature of the system, however, allows for focal shifting through the use of the SLM, keeping a completely digital

procedure in the acquisition of three dimensional images.

An holographic focal shift in the excitation light pattern can be obtained, with the objective in a fixed position, by simply adding a Fresnel lens pattern to the calculated hologram (see section §5.2). A three dimensional image can be therefore acquired by scanning several times one of the scanning sequences, adding to all the phase masks of the sequence a Fresnel lens of different focal power at each scan. There are however some limitations in the system's ability to obtain images axially shifted from the objective's intended focal plane.

A first limitation comes from the fact that the tube lens of a standard microscope creates an image of the focal plane of the objective on the detector's surface. The axial shift of the excitation pattern therefore creates an out of focus image on the detector. The magnitude of such problem depends on the numerical aperture of the objective; with the high numerical aperture required for two photon excitation, the artifact makes the spots indistinguishable from each other even with a few micrometers of defocusing. A second limitation is due to the corrections of the objective itself. Modern microscope objective are engineered with the aim of minimizing aberrations on their focal plane. The downside of such optimization is that focal points generated on other planes, even if only slightly shifted from the main one, are affected by a strong spherical aberration.

In the measurements reported in this thesis, the only correction applied in order to suppress such problems, was an increase in the spot integration area while defocusing. With such correction, and a 1.0 N.A. objective, an effective defocusing range of $\pm 20 \mu m$ was achieved. Further correction could be obtained with the use of an adaptive tube lens, in order to keep the spots on focus on the detector. Spherical aberration correction on the excitation light path could be applied through the SLM, modifying the holograms with adaptive optics technique. Similar corrections on the fluorescence light path would require an adaptive mirror.

Points of interest selection

Once an image of the sample has been acquired, the calculation of a phase mask illuminating user defined points of interest is straightforward. Since all the phase masks of the raster scan are calculated with the discrete FFT method, the intensity of each pixel of the two photon image was acquired by illuminating the sample in a location corresponding to a single pixel in the GS algorithm input image.

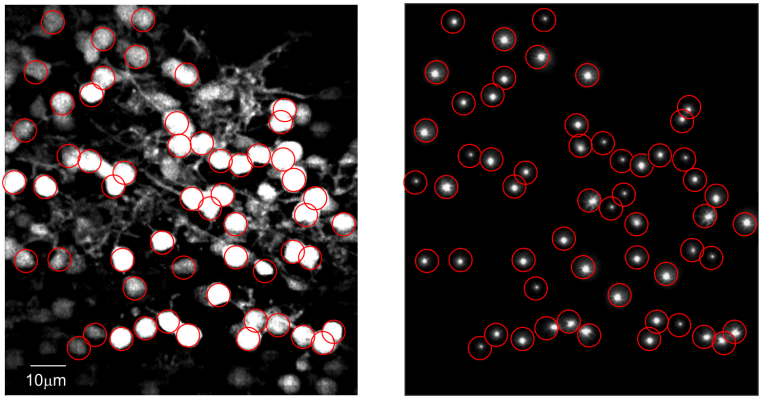

Figure 6.2.: Example of points selection.

A. After the acquisition of an image (left panel), the user selects multiple pixels of interest (at the center of the red circles). A phase mask illuminating the points of interest is calculated, right panel reports an image of the camera output during points illumination.

The two photon image is therefore effectively represented in SLM input coordinates. Once the user has selected a number of points of interest (by simply mouse-clicking on them on the graphic interface), a synthetic binary image with value 1 in the pixels corresponding to the points of interest, and 0 elsewhere, is generated and used for the calculation of the hologram.

In the selection of the points of interest, it is important to select only points which can be easily discriminated by the detector during acquisition. There are three important factors in the determination of the minimum distance for the discrimination of points of interest:

- THE DIFFRACTION LIMIT: In an ideal system the minimum distance would be determined by the diffraction limit. The signals from two points placed at a diffraction limit distance from each other could be discriminated with some signal analysis procedure. However, in order to completely avoid cross talk, a minimum distance of $\sim 2-3$ times the diffraction limit should be imposed.

- THE SPOT SIZE ON THE DETECTOR DUE TO TISSUE SCATTERING: In highly scattering tissues, such as the cerebellar slices used in the reported experiments, the light spots on the detector are much bigger than the diffraction limit. A safe minimum distance between points of interest in this situation is the distance between focal points in the grid used for the acquisition of the two photon image. Shorter distances are usually possible, but a test of discrimination of the signals is necessary during the first acquisition.

- THE DETECTOR'S PIXEL SIZE: Since the acquisition of fast signals is usually performed on fast detectors with low spatial resolution, or on a subregion of an high resolution detector, it is important to verify that no couple of points is imaged on the same pixel, or adjacent pixels, of the detector.

7. Experimental setup

7.1. Setup design

Calcium imaging experiments were carried out on cerebellar slices from rats and mices, stained with Fura-2 AM (Detailed preparation procedure is reported in chapter 8). Most experiments were performed with a standard procedure:

1. Selection, in brightfield microscopy, of an area of interest in the slice, on which to perform the experiment.

2. Positioning of a bipolar tungsten electrode on an input fiber, performed in brightfield with a three dimensional micromanipulator.

3. Selection, with live two photon holographic microscopy, of a focal plane of interest.

4. Acquisition of an holographic two photon image of the sample.

5. Selection of multiple points of interest.

6. Periodic acquisition of calcium signals in response to fiber stimulation, over a long time span (up to 1-2 hours).

The setup used for these experiments thus needs a detector with high spatial resolution for brightfield and holographic imaging, and high acquisition speed for calcium signals recording. Illumination of the sample must be provided by a standard white lamp for brightfield, and by a femtosecond pulsed infrared laser for two photon imaging, with a SLM for light modulation. A low magnification objective with high numerical aperture is needed for optimal two photon performances.

The experiments were performed on a custom made upright microscope. A standard Kohler illumination optical path provides condensed white light from a fiber coupled halogen lamp, for brightfield illumination porpoises. The two photon microscopy setup is schematically illustrated in figure 7.1.

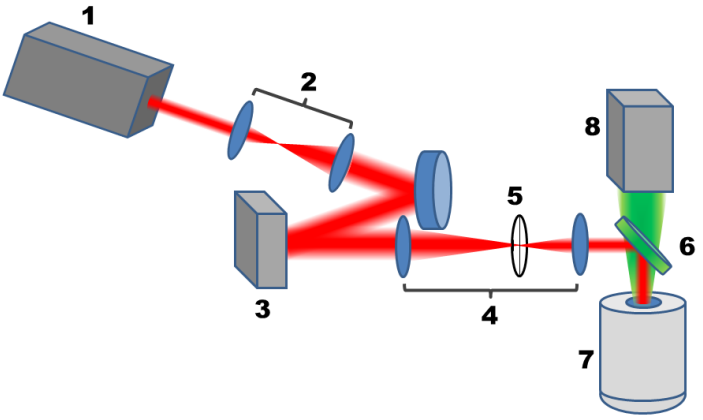

Figure 7.1.: Schematic of the Calcium imaging setup.

1-Ti:sa Laser (Chameleon Ultra II, Coherent) 2- 6x Beam expander (f1=2.5 cm, f2=15 cm) 3- Spatial Light Modulator (X10468-07, Hamamatsu) 4- Telescope (f1=40 cm, f2=25 cm D=60cm) 5- Zero order beam stop 6- Dichroic Mirror (750nm ,750dcspxr, Chroma) 7- Microscope Objective (Zeiss Plan-APOCHROMAT 20X 1.0 N.A. or Zeiss Plan-APOCHROMAT 40X 1.0 N.A.) 8- Camera (Coolsnap, Photometrics and Micam Ultima, Scimedia / Orca Flash 4.0, Hamamatsu).

Fluorescence excitation is provided by a mode locked, $Nd : YVO_4$ pumped $Ti : Sa$ laser (Chameleon Ultra II, Coherent), with continuously tunable emission wavelength in the 720-1064 nm range, with a peak power of 4 W at 800 nm. Output power of the laser can be finely tuned with a $\lambda/2$ waveplate mounted on a motorized rotation actuator, followed by a fixed position Glan-Taylor polarizer. After the

polarizer, excitation light has vertical polarization, required for optimal SLM performances. In order to fill the SLM active surface, the beam is expanded by a 6x beam expander, formed by two plano-convex, IR coated lenses.

After expansion, the beam is reflected by the SLM surface, and passes through a beam reducing telescope, which reproduces the Electric field distribution of the SLM surface near the objective's back aperture. In previously reported systems [33, 32], the two lenses of the telescope are at a distance to each other equal to the sum of their focal lengths, the SLM is in the back focal plane of the first telescope lens, and the objective is in the focal plane of the second one. This way a magnified image of the desired pattern is formed on the focal plane of the first lens, while the electric field at the SLM surface is reproduced on the objective back aperture, as reported in section §5.4, with a magnification depending on the ratio between the telescope lenses focal lengths. In such configuration however, the zero order of diffraction produced by the SLM will be focalized on the same plane where the objective forms the input pattern of the SLM. This would introduce an extremely bright spot of excitation light on the focal plane of the microscope, damaging the sample and creating artifacts on the images. A spatial filter can be introduced in the image of the pattern obtained between the telescope lenses, but this would create a dark area in the center of the pattern focalized by the objective. In the setup used for this thesis, a Fresnel lens based method for the suppression of the zero order light was used. A schematic representation is reported in figure 7.2.

In order to eliminate the zero order of diffraction, each calculated hologram is summed to a Fresnel lens pattern, so that the desired illumination pattern is generated on a plane axially shifted from the one of the zero order of diffraction. In this configuration, it is possible to insert a thin beam stop in the focal plane of the first lens, thus blocking the zero order beam without affecting the illumination pattern. The second lens of the telescope is slightly shifted in order to correct for the axial position of the illumination pattern created by the objective. Two different objectives are used to achieve different magnifications:

a 20X and a 40X objective (Plan-APOCHROMAT 20X 1.0 N.A. and Plan-APOCHROMAT 40X 1.0 N.A. , Zeiss), both with 1.0 numerical aperture, and optimized for near IR excitation.

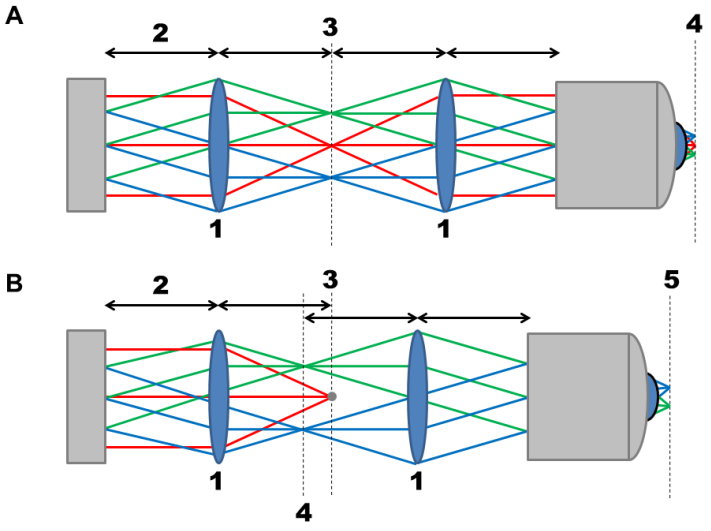

Figure 7.2.: Suppression principles for the zero order of diffraction in the path between the SLM and the objective.

Red lines represent the optical path of undiffracted light, while green and blue lines represent light forming two different points in a desired pattern. Telescope lenses are represented with the same focal length for simplicity. Panel A shows the optical path without zero order suppression; in this configuration undiffracted light creates a bright spot at the center of the image. 1. Telescope lenses 2. Telescope lenses focal length. 3. First plane of formation of the desired pattern, and focal point of undiffracted light. 4. Objective focal plane. Panel B shows the optical path with zero order suppression. In this configuration undiffracted light does not reach the objective focal plane. 1. Telescope lenses 2. Telescope lenses focal length. 3.Focal plane of the first telescope lens, with beam blocker at the center, absorbing undiffracted light. 4. First plane of formation of the desired pattern. The axial shift in this plane position is given by the addition of a Fresnel lens pattern to the calculated hologram. 5. Objective focal plane.

Excitation light and fluorescence light are separated by a dichroic mirror (750dcspxr, Chroma), and two emission filters (a 750 nm short-pass, and a fluorescence filter depending on the dye). In order to acquire both high resolution images and fast signals, two different detectors were used: an high resolution (1392x1040 pixels) cooled CCD camera (Coolsnap, Photometrics), and a fast (up to 10 kHz acquisition frequency) CMOS camera (Micam Ultima, Scimedia) with low resolution (100x100 pixels). The image of the objective's focal plane was generated on the detectors surface by an achromatic tube lens of 15 cm focal length. Selection of the detector in use was performed with a mirror mounted on a flippable holder. Only the most recent measurements were performed with a single sCMOS camera (Orca Flash 4.0, Hamamatsu) with high resolution (2000x2000 pixels), high efficiency in low light ($1.9e^{-}rms$ noise per frame), and high acquisition speed on a subregion of the detector (1.6 kHz on a 128x128 pixels subregion). In order to exploit the high acquisition speed of the sCMOS detector on small subregions, two different tube lenses, mounted in different tubes on a revolving selector, are used; one with 15 cm focal length, and one with 2.5 cm focal length, leading to a 0.16 ratio between magnifications.

7.2. Setup characterization

Imaging resolution

The setup described in section §7.1 is capable of acquiring two photon images, in two and three dimensions, through the use of the SLM, without any mechanical moving part, and to illuminate simultaneously multiple points of interest, selected on a two photon image, with submicrometer precision. The applied procedure for two photon images acquisition is described in chapter 6. In order to verify the setup performances, the spatial resolution of the system was measured, both in the lateral and axial directions, the points selection precision was verified, and the available axial shift range was addressed.

Spatial resolution was measured by imaging under-resolved fluorescent latex beads (100 nm diameter, $\lambda_{em} = 568nm$, Sigma Aldrich),

immobilized in agarose gel, with 800 nm excitation wavelength and a 40X, 1.0 N.A. Objective (Plan-APOCHROMAT, Zeiss).

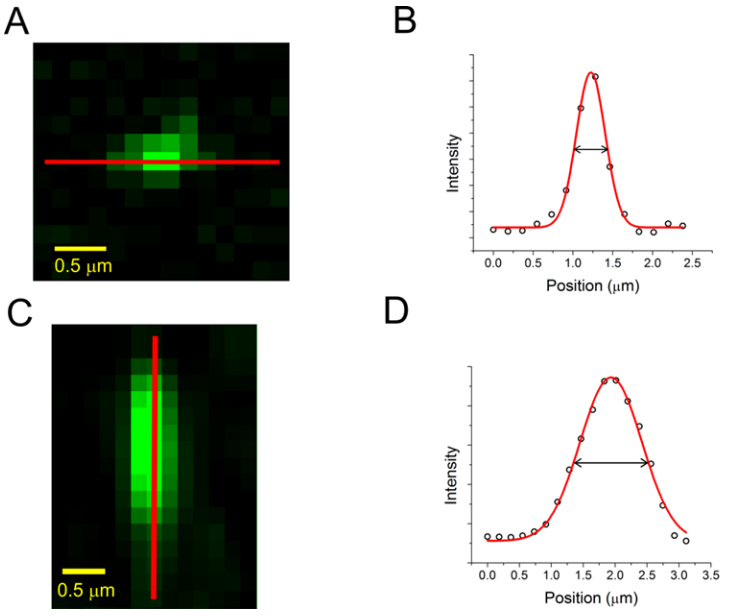

Figure 7.3.: Examples of microbeads images.

A. Image of a fluorescent polistyrene bead (100 nm diameter), immobilized in 1% agarose gel. The red line indicates the section used for fitting in B. B. Lateral profile of a fluorescent polystyrene bead, fitted with a Gaussian function. The arrow indicates the FWHM of the curve.C. Axial section of a 3D image of fluorescent polystyrene bead. The focal plane was shifted in $0.2\mu m$ steps by superimposing a Fresnel lens pattern on the sliding grid phase masks. The red line indicates the section used for fitting in D. D. Axial profile of a single bead, fitted with a Gaussian function. The arrow indicates the FWHM of the obtained curve.

Due to the high brightness of the sample, low excitation power was used (600 mW total, corresponding to 0,66 mW per focal volume in the 600x600 pixel scan sequence) to avoid detector saturation, and a 3x3 pixels integration area ($19.5x19.5\mu m^2$detector surface) was used for spots intensity measurement. The theoretical resolution limit (see section §1.3) for such combination of objective and excitation wavelength

is 400 nm in the lateral direction, and $1.1\mu m$ in the axial direction. Images were acquired with the 600x600 pixels scan sequence, covering a field of view of 220x300 μm^2, leading to a pixel size of 0.37*0.5 μm^2. Axial planes were acquired in 0.2 μm steps, through SLM generated axial shifts. A total of 25 beads were imaged on all three axes. The profiles were fitted with Gaussian functions, even on the axial direction, as the small integration area employed is equivalent to the use of a confocal pinhole, thus suppressing the typical Lorentzian shape of the two photon excitation axial profile. The averages of the results of the fits gave a lateral resolution estimation of $420 \pm 8nm$, and an axial resolution of $1.15 \pm 0.05\mu m$, thus proving that the system is diffraction limited in all three dimensions. Example images of microbeads and their respective Gaussian interpolations are reported in figure 7.3.

POI selection precision

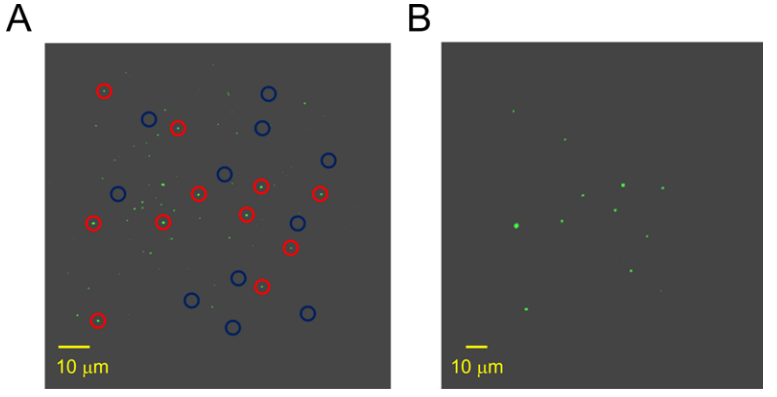

Figure 7.4.: Pointing Precision measurement.

A. Image (green) of fluorescent polistyrene beads (100 nm diameter, $\lambda_{em} = 568nm$), immobilized in 1% agarose gel. Red circles indicate the selected beads for the placement of focal points. Blue circles indicate the position of control focal points placed in dark areas of the image.B. Single exposure acquisition of the pattern illuminating the beads indicated by red circles in panel A. It can be observed that only the focal points placed over fluorescent beads are eliciting fluorescence signal. Grayscales were manipulated in both images to enhance contrast.

The precision in points of interest illumination was tested on the same microbeads sample. A bidimensional image with multiple fluorescent beads was acquired, and points of interest were placed on the brightest pixels of 11 beads images. For control the same number of points of interest were selected in dark areas of the sample. During the illumination of the points of interest through an appropriate phase mask, a single exposure image of the sample with the high resolution CCD camera was acquired, the focal points positioned on the microbeads were all extremely bright, compared with the randomly positioned focal points, which only showed a faint background fluorescence signal. The experiment is reported in figure 7.4. This proves that the error in focal points positioning is smaller than the resolution limit.

Three dimensional imaging

In order to test the three dimensional imaging capabilities of the systeam, a Purkinje cell in an acute cerebellar slice was intracellularly loaded with Alexa488 sodium salt and a 3d image was acquired with the 20x objective. The image (reported in figure 7.5, panels A and B) was acquired by sequentially shifting the excitation plane in 10 steps of 2µm, and acquiring separate images with the 400 frames scanning grid with 20 ms exposure of the camera (total acquisition time around 10 s for each confocal plane.) . Excitation light was set at 750nm with laser power of 4mW/FP, and a 515/30 bandpass filter was used for fluorescence detection. While an image of the full arborization of the Purkinje cell dendritic tree could be acquired, the low spatial sampling ($\sim 0.8 \mu m/pixel$) obtained with the 20X objective did not allow the discrimination of dendritic spines. Another image of a similar cells was acquired in identical condition with the 40X objective, in order to double the spatial sampling (a close up image is reported in figure 7.5, panel C); dendritic spines are clearly visible, proving that the performances of an SLM base two photon microscope are comparable to those of a traditional setup.

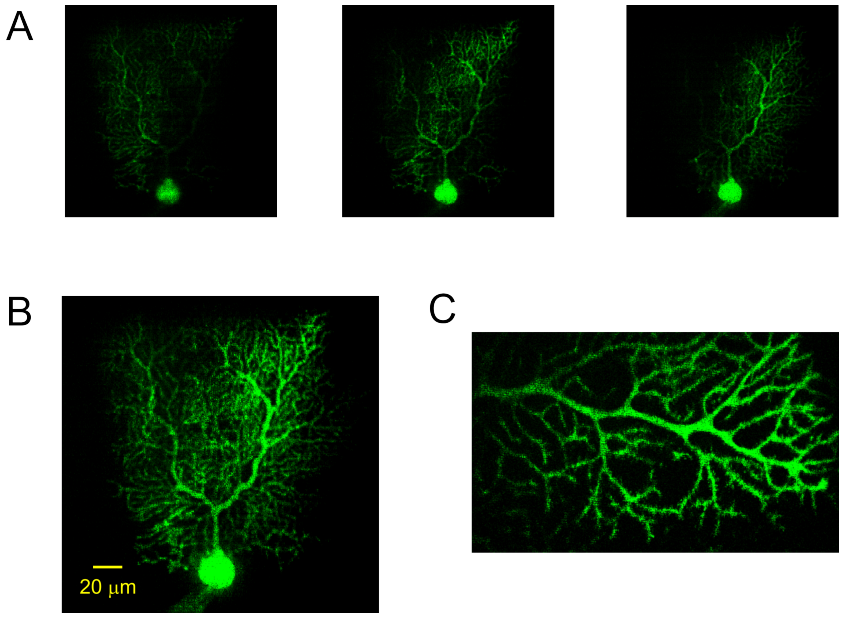

Figure 7.5.: 3d imaging test.

3D image of a Purkinje cell, intracellularly loaded with Alexa488. A. Three confocal images acquired at planes 4 µm apart. B. Overlay of 10 different confocal images showing the entire purkinje cell.

8. Cerebellar calcium signals experiments

The holographic setup described previously was employed for high speed calcium imaging experiments on multiple individual cells in acute cerebellar slices. Most of the results reported in this chapter were published as a peer reviewed article in "Frontiers in cellular neuroscience" [34].

8.1. Sample Preparation

Cerebellar calcium signals experiments were performed on acute cerebellar slices ($200\mu m$ thick), obtained from18- to 25-day-old Wistar rats. Rats were anesthetized with halothane (0.5 ml in 2 L for 1–2 min) before being sacrificed by decapitation. All experiments were conducted in accordance with international guidelines on the ethical use of animals (European Community Council Directive 86/609/EEC). The cerebellum was gently removed, and the vermis was isolated, fixed with cyanoacrylate glue, and immersed in cold (2–3 °C) cutting solution. Slices were cut in the sagittal plane. The cutting solution contained (in mM): 130 K-gluconate, 15 KCl, 0.2 EGTA, 20 HEPES, 10 glucose; the solution was brought to pH 7.4 with NaOH. Slices were then transferred to an oxygenated Krebs' solution containing (in mM): 120 $NaCl$, 2 KCl, 1.2 $MgSO_4$, 26 $NaHCO_3$, 1.2 KH_2PO_4, 2 $CaCl_2$, 11 glucose; pH 7.4 when equilibrated with $95\%O_2$-$5\%CO_2$. For extracellular bulk loading, slices were deposited on the bottom of a small Petri dish (35 mm $\times$10 mm) filled with 2ml of ACSF, ventilated with $95\%O_2$-$5\%CO_2$ and placed in a warmer (PBI International) at 34 °C. A $50\mu g$ aliquot of Fura-2AM (Molecular Probes, Eugene, OR, USA) was

prepared in 48μl DMSO and 2μl Pluronic F-127 (Molecular Probes). The dye aliquot was then placed on top of the slice in the Petri dish and slices were incubated in the dark at 35–37°C for 60 minutes. Slices were maintained at room temperature for at least 30 minutes before being transferred to the recording chamber. Slices were gently positioned in the recording chamber and fixed with a nylon mesh attached to platinum-wire to improve tissue adhesion and mechanical stability. Perfusion of oxygenated Krebs' solution at room temperature was continued during the recording session.

8.2. Simultaneous high speed calcium signals acquisition

In order to illustrate the actual capibilities of the system in calcium imaging, a typical experiment is reported in figure 8.1. Live Imaging acquisition mode was used for confocal plane selection. Planes were selected at 50-60 μm depth in the cerebellar slice. A standard two photon image of the selected plane is acquired with the 400 frames scanning grid. Laser power was set to 4mW/FP. CCD Camera and SLM refresh rate were set to 50 ms per frame in order to obtain an image with high S/N ratio, for a total image acquisition time of 20 seconds. POIs were selected within the soma of each visible granule cell, total number of cells monitored is $>$100. During signal acquisition, laser power was set to 10 mW/FP. Calcium transients were recorded by the high speed CMOS camera at frequencies up to 1 kHz. In standard conditions granule cell calcium signals showed a ΔF/F0 variation of 5-10% peaking around 100 ms after stimulation, acquired with an S/N ratio of around 10 at 1 kHz.

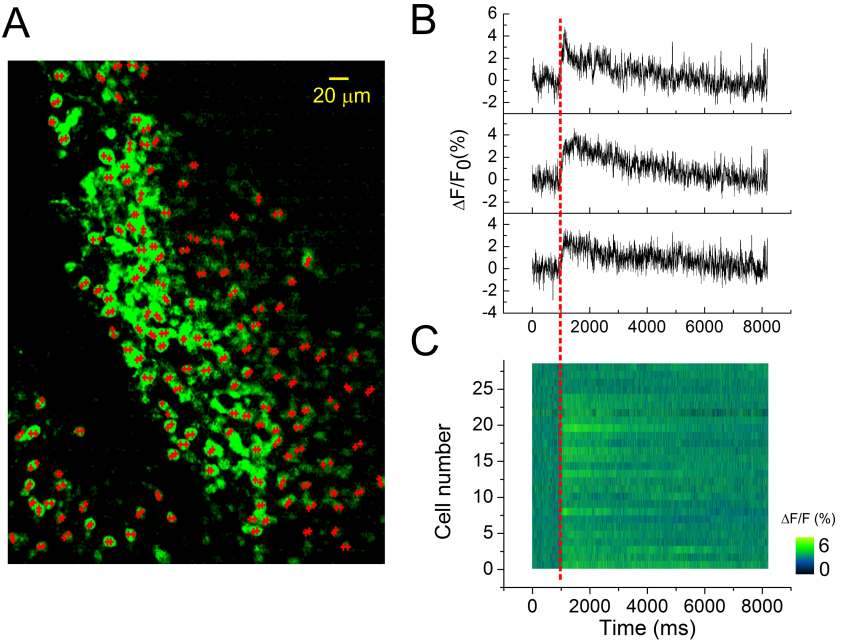

Figure 8.1.: Typical calcium imaging experiment with an holographic microscopy setup.

A. Reconstructed image of the granular layer in an acute cerebellar slice bulk-loaded with Fura-2 AM. Red crosses indicate the user selected positions for high frequency signals acquisition. B. Example of three different 1 kHz rate trace, with different kinetics, which would be impossible to discern with low time resolution. The red line indicates stimulation onset. C. Ensemble response of all 27 active cells in the sample, non responding granule cells are not shown.

8.3. Synaptic nature of responses

A first, important control experiment to perform with a novel calcium imaging technique, is the demonstration of the synaptic nature of the signals recorded. Fluorescence variations in these experiments are generally generated by variations in calcium concentration induced by neronal activity, but some artifacts can occur during stimulation, such as tissue movement, or cell apoptosis. In order to demonstrate

that the signals recorded in standard conditions by the system have a synaptic nature, and are therefore of biological interest, a variety of drugs were used to condition the responses.

The synaptic-dependent nature of the responses was directly assessed by applying blockers for ionotropic GABA and glutamate receptors. granule cells express several GABA-A receptor subunits[35, 36]. Blockade of GABA-A receptor-mediated synaptic inhibition is known to increase spike discharge and to depolarize the granule cells, increasing transmembrane Ca^{2+} influx[37]. During recordings, the perfusion of a solution containing the GABA-A receptor blocker, $20\mu M$ gabazine, increased both the peak amplitude ($+129.9\pm2.5\%$; n=15 slices; $p<0.001$) and the number of active cells ($+89.1 \pm 11.3\%$; n=15 slices; $p<0.01$). After 30 minutes washing with control Krebs' solution, the calcium signals recovered close to the initial conditions ($-3.5 \pm 1.8\%$; n=5 slices; $p>0.65$). The effect of Gabazine perfusion and wash-out is shown in figure 8.2.

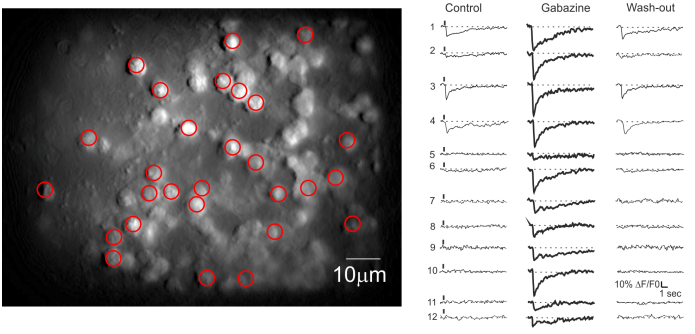

Figure 8.2.: Effects of Gabazine perfusion and wash-out in the granular layer.

Left panel shows an image of fluorescent granule cells acquired with the 40x objective. Red circles mark granule cells from which calcium signals were recorded.Calcium responses were elicited by 10 mossy fiber burst at 50 Hz, delivered at 0.1 Hz. Right panel shows responses to mossy fiber bursts. In control (left), only three granule cells (traces 1, 3, 4) respond to synaptic activation. After application of 20µM gabazine, all granule cells respond to synaptic activation and traces 1, 3, 4 are remarkably increased. Finally, after wash-out (right), all granule cell responses revert back to control conditions.

Gabazine application was followed by coperfusion of glutamate receptor blockers. Granule cells show a remarkable expression of NMDA receptors[38, 39]. Blockade of NMDA receptors is known to markedly decrease EPSP temporal summation and spike discharge, mostly in response to high-frequency mossy fiber bursts. In SLM-2PM recordings, perfusion of a solution containing the NMDA receptor blocker, $50\mu M$ APV, markedly reduced both the peak amplitude ($-75.5 \pm 12.3\%$; n=6 slices; $p<0.01$) and the number of active cells ($-79.6 \pm 9.3\%$; n=6 slices; $p<0.01$). The residual granule cell activity was completely blocked by application of the AMPA receptor blocker, $10\mu M$ NBQX(-100%; n=5 slices; $p<0.01$).It should also be noted that the area covered by responding granule cells increased with gabazine ($+86.3 \pm 15.5\%$; n=6 slices; $p<0.01$) and decreased with APV ($-34.9 \pm 4.4\%$; n=6 slices; $p<0.01$), according to the lateral inhibition and center-surround organization reported in the granular layer[22]. The effects of receptor blocker perfusion is shown in figure 8.3.

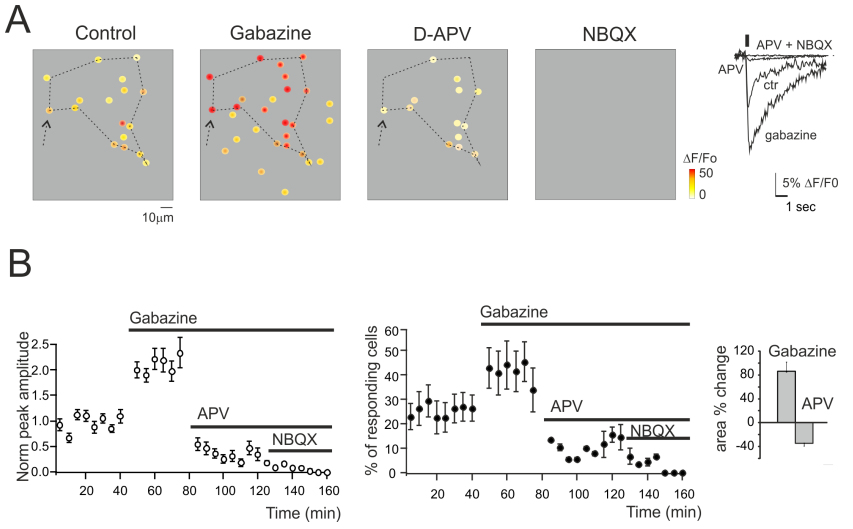

Figure 8.3.: Effects of receptor blockers perfusion.

Panel A shows activity maps of the granular layer showing the peak intensity of neuronal responses on a color scale. The location of colored dots corresponds to that of neurons in the slice. The four panels (from left to right) show that both the activation intensity and the number of active granule cells increase remarkably during 10 μM gabazine application, decrease following addition of 50 μM APV, and are fully blocked following further addition of 20 μM NBQX. The responding area (dashed lines) varies following the application of gabazine and APV (+73.1 and−24.5% compared to control conditions). The traces on the right show the $\triangle F/F_0$ changes caused by the drugs in a selected granule cell (arrow). Panel B shows time course of the normalized peak amplitude and of the number of responding granule cells in different experiments following the application of synaptic blockers (n=254 cells;n=15 slices.). In all these experiments, $\triangle F/F_0$ was measured at the peak of Fura-2AM calcium signals elicited by mossy fiber burst stimulation (10 impulses at 50 Hz) at 0.1 Hz.

8.4. Correlation of calcium signals with spike discharge

In order to determine the correlation between neuronal electroresponsiveness and $\Delta F/F_0$, whole cell recordings were performed with $200\mu M$ Fura-2 in the patch-pipette from granule cells and Purkinje cells.By us-

ing intracellular loading, the recoded cell was unequivocally identified and the electrical and optical signals could be recorded simultaneously. Results are illustrated in figure 8.4 for granule cells, and in figure 8.5 for Purkinje cells.

Granule cells showed typical passive (high input resistance $1.9 \pm 0.3G$, low membrane capacitance $4.2 \pm 0.1pF$, n=5) and active electroresponsive properties[40, 41]. Injection of depolarizing current pulses generated repetitive spike discharge associated with $\Delta F/F_0$ of over 10%. The calcium signal increased during spike discharge, continued its growth for tens of ms ($78.2 \pm 34.5ms$; n=4, p=0.05), reached the peak and then slowly decayed over hundreds of ms ($364.2 \pm 61ms$; n=4, p=0.05).

The relationship between $\Delta F/F_0$ and the number of granule cell spikes was evaluated during repetitive mossy fiber stimulation. The granule cells generated a variable number of spikes probably reflecting quantal variability in the neurotransmission process. A quasi-linear correlation of the number of granule cell spikes with $\Delta F/F_0$ peak ($R^2 = 0.85$; $p<0.05$; n=5) and time-to-peak ($R^2 = 0.94$; $p<0.01$; n=5) emerged, as well as of the depolarization area with $\Delta F/F_0$ area ($R^2 = 0.98$; $p<0.001$; n=5).

Purkinje cells were found to be spontaneously discharging ($22.8 \pm 2.5Hz$; n=4; $p<0.05$) and their activity was analyzed while injecting negative currents sufficient to maintain the membrane potential at -70 mV. Purkinje cell responses to mossy fiber bundle stimulation consisted of either simple spikes or complex spikes. Simple spikes were organized in brief bursts and longer discharges with variable adaptation[42], probably involving variable spike transmission from the granule cells. The $\Delta F/F_0$ related to simple spikes did not usually exceed 2–3% in PCs, and was thus smaller than in granule cells. The complex spikes appeared as high-frequency bursts with marked adaptation. The $\Delta F/F_0$ of complex spikes was significantly larger (>20%) than that of simple spikes and lasted for hundreds of milliseconds after the end of spike discharge. Moreover, the delay of calcium increase with respect to stimulus onset was significantly lower compared to that observed with simple spike responses ($3.7 \pm 1.4ms$ vs. $12.3 \pm 3.6ms$ respectively, n=4;

p<0.01). As for granule cells, a quasi-linear correlation of the number of Purkinje cell simple spikes with $\Delta F/F_0$ peak ($R^2 = 0.9$; p<0.01; n=4) and time-to-peak ($R^2 = 0.56$; p<0.01; n=4) emerged, as well as of the depolarization area with the $\Delta F/F_0$ area ($R^2 = 0.63$; p<0.05; n=4).It should be noted that traces taken from neurons that are either bulk-loaded or intracellularly loaded showed similar $\Delta F/F_0$ kinetics for rise-time ($76.3 \pm 5.9ms$ vs. $81.7 \pm 8.1ms$; n= 10 granule cells; p=0.92) and decay time (half-decay: $2.7 \pm 0.2s$ vs. $2.85 \pm 0.3s$; n=10 granule cells; p=0.89). Given that the calcium buffering capacity and the fluorescence yield of the two dyes is the same, this comparison suggests that the concentrations of Fura-2 and Fura-2 AM obtained with the two loading procedures were similar. It should also be noted that the relationships of $\Delta F/F_0$ peak vs. spike number and $\Delta F/F_0$ time-to-peak vs. spike number could be extrapolated toward a single spike, which corresponded to a detectable somatic calcium signal in several cases. From the slope of the $\Delta F/F_0$ vs. time-to-peak relationship it was possible to infer the number of granule cell spikes (two-tails t-test; p=0.82) and Purkinje cell spikes (two-tailst-test; p=0.99). The deviation of the predicted from actual spike number was negligible for granule cells ($< \pm 1$ spike) but became evident for Purkinje cells when the number of spikes increased to more than five. Therefore, prediction of the number of spikes from $\Delta F/F_0$ time-to-peak was more reliable for granule cells than for Purkinje cells.

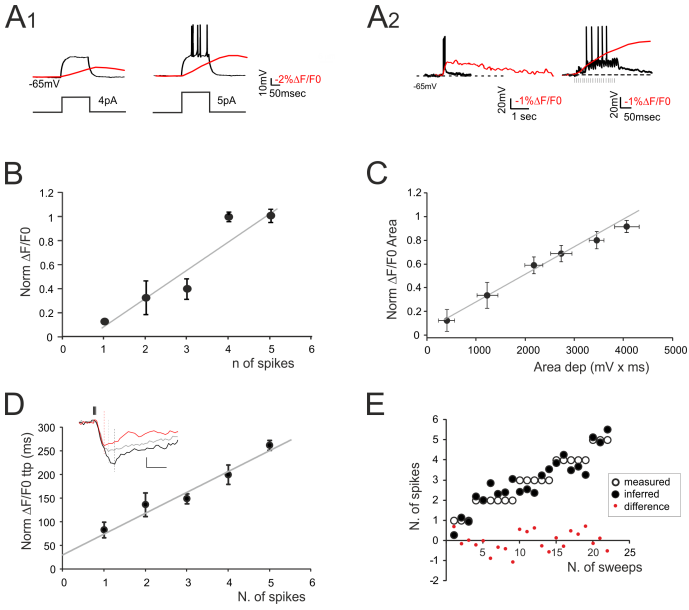

Figure 8.4.: Dependency of calcium signals from neuron activity (Granule cells).

Whole cell recordings were performed on granule cells in unstained slice, with cell impermeant Fura-2 present in the intracellular solution. Calcium signals and electrophysiological acquisitions were performed simultaneously. A1. Voltage traces showing responses of a granule cell to a 30-ms step-current injection (left 4 pA; right 5 pA). The transition from the sub-threshold (left) to the spiking regime (right) is correlated with an increase in the calcium transient (red traces). A2. Voltage traces showing EPSP-spike complexes induced by a mossy fiber burst (20 stimuli at 100 Hz). The sustained calcium transient correlated with action potentials. B. Dependence of normalized $\Delta F/F_0$ peak on the number of spikes emitted by granule cells in response to mossy fiber bursts (20 stimuli at 100 Hz) revealing a linear correlation (gray line; n=5 cells; $R^2 = 0.85$; p<0.05). C. Dependence of normalized $\Delta F/F_0$ area on the average depolarization in response to mossy fiber bursts (20 stimuli at 100 Hz) revealing a linear correlation (gray line; n=5 cells; $R^2 = 0.98$; p<0.001). Only sub-threshold responses were considered. D. Dependence of normalized $\Delta F/F_0$ time-to-peak on the number of spikes emitted in response to mossy fiber bursts (20 stimuli at 100 Hz) revealing a linear correlation (gray line; n=5 cells; $R^2 = 0.98$; p<0.01). The traces in the inset show $\Delta F/F_0$ signals correlated with 1 (red), 3 (gray), and 5 spikes (black). E. Comparison of the number of spikes measured in granule cells and that predicted by the slope of the time-to-peak vs.spike relationship shown in panel D. Note the matching between predicted and measured results (two-tailedt-test; p=0.82).

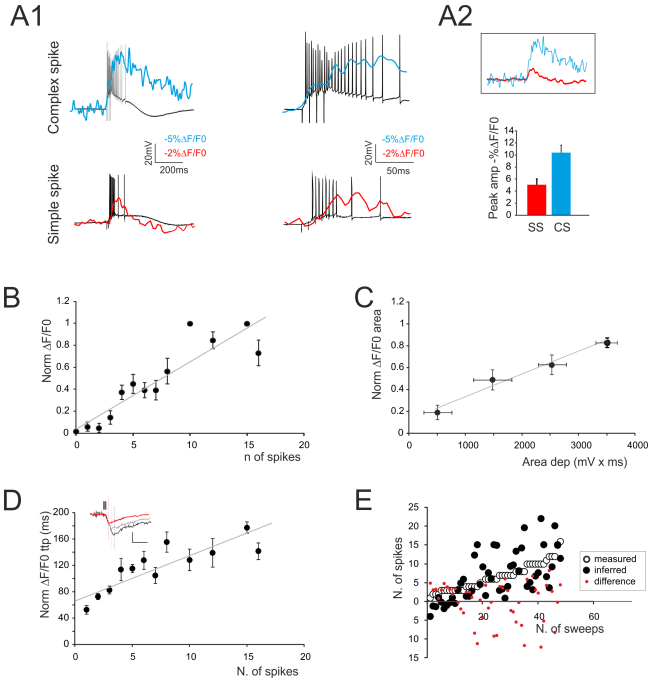

Figure 8.5.: Dependency of calcium signals from neuron activity (Purkinje cells).

Whole cell recordings were performed on Purkinje cells in unstained slice, with cell impermeant Fura-2 present in the intracellular solution. Calcium signals and electrophysiological acquisitions were performed simultaneously. A1. Voltage traces showing EPSP-spike complexes induced by a mossy fiber burst (5 stimuli at 100 Hz). Note the sustained depolarization induced by the presence of action potentials. Simple spikes (bottom panels) and complex spikes (upper panels) generate different calcium signals. A2. The calcium signals generated by simple and complex spikes are compared. The histogram shows larger size of complex-than simple-spike calcium signals. B. Dependence of normalized $\triangle F/F_0$ peak on the number of simple spikes emitted by Purkinje cells in response to mossy fiber bursts (5 stimuli at 100 Hz) revealing a linear correlation (gray line; n=4 cells; $R^2 = 0.9$; p<0.01). C. Dependence of normalized $\triangle F/F_0$ area on the average depolarization during simple spike discharge in response to mossy fiber bursts (5 stimuli at 100 Hz) revealing a linear correlation (gray line; n=4 cells; $R^2 = 0.63$; p<0.05; mean±s.e.m.). Only subthreshold responses were considered. D. Dependence of normalized $\triangle F/F_0$ time-to-peak on the number of simple spikes emitted in response to mossy fiber bursts (5 stimuli at 100 Hz) revealing a linear correlation (gray line; $R^2 = 0.56$; p<0.01; mean ±s.e.m.). The traces in the inset show $\triangle F/F_0$ signals correlated with one (red), five (gray) and 10 spikes (black). E. Comparison of the number of spikes actually measured in Purkinje cells and that predicted by the slope of the time-to-peak vs.spike relationship shown in panel D. Note the matching between predicted and measured results (two-tailedt-test; p=0.99)

8.5. Correlation of calcium signals with input stimuli

Mossy fiber bursts composed of different numbers of stimuli (1– 10) of identical intensity were used to evaluate the sensitivity of $\Delta F/F_0$ to the input pattern. The responses were recorded from the granule cells soma and showed a direct relationship between the number of mossy fiber impulses and $\Delta F/F_0$,which could be fitted with a growing exponential function ($R^2 = 0.94$; p$<$0.01). In some cells, signals related to single stimuli were clearly detectable, while in others a step marked the beginning of responses at around 4–5 stimuli. A similar direct relationship could be observed when correlating the number of mossy fiber inputs and $\Delta F/F_0$ in Purkinje cells, which could be fitted with a linear function with 0-intercept ($R^2 = 0.81$; p$<$0.05). In this case, the spikes generated by granule cells had to travel through the ascending axon (parallel fibers are severed in sagittal slices) and then activate the Purkinje cells. Therefore, the stimuli propagated through the entire network and the intensity of neuronal responses at different network levels was correlated with the number of mossy fiber impulses.

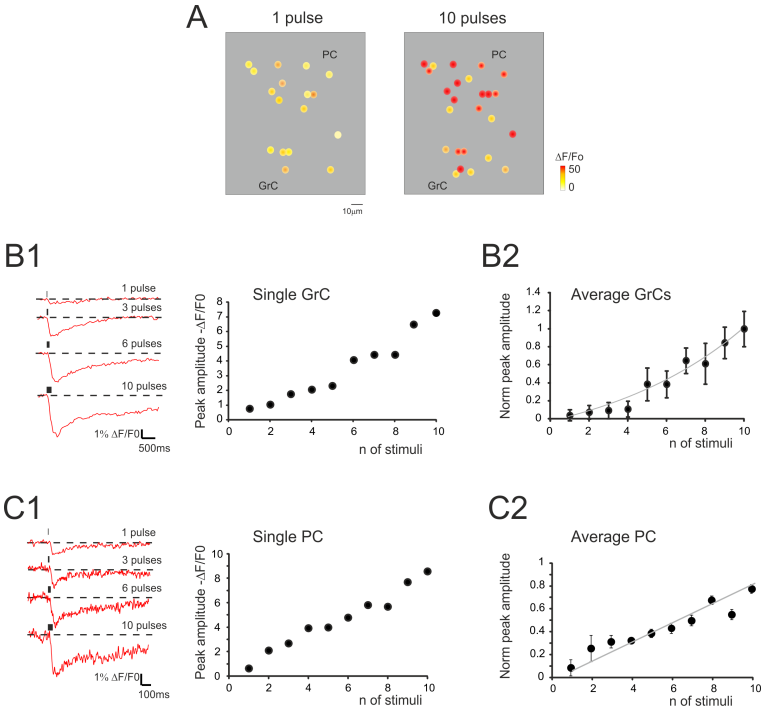

Figure 8.6.: Dependency of calcium signals from input stimuli.

A. Activity maps of a cerebellar slice showing the peak intensity of neuronal responses on a color scale. The location of colored dots corresponds to that of neurons in the slice. The two panels (from left to right) show that both the response intensity and the number of active granule cells increase remarkably by raising the number of stimulation pulses. B1. Traces on the left illustrate the time course of $\Delta F/F_0$ obtained from a granule cell in response to an increasing number of mossy fiber stimuli at 50 Hz. The plot on the right shows the values of $\Delta F/F_0$. Note the increase in normalized peak amplitude from one to ten stimuli. B2. The plot shows the average values of $\Delta F/F_0$. Note the increase in normalized peak amplitude from one to ten stimuli (n=35 cells in six experiments; exponential fitting $R^2 = 0.94$; p<0.01). C1. Traces on the left illustrate the time course of $\Delta F/F_0$ obtained from a Purkinje cell in response to an increasing number of mossy fiber stimuli at 50 Hz. The plot on the right shows the values of $\Delta F/F_0$. Note the increase in normalized peak amplitude from one to ten stimuli. C2. The plot shows the average values of $\Delta F/F_0$. Note the increase in normalized peak amplitude from one to ten stimuli (n=13 cells in five experiments; linear fitting $R^2 = 0.81$; p<0.05). In all these experiments, $\Delta F/F_0$ was measured at the peak of Fura-2 AM calcium signals elicited by mossy fiber stimulation.

8.6. Spatial organization of calcium responses

Given the possibility of resolving multiple neuronal responses, holographic two photon recordings were used to characterize the fundamental properties of cerebellar circuit activation. The delay from mossy fiber activation was estimated by intercepting the rising phase of the $\Delta F/F_0$ response at 20% of peak amplitude. Following mossy fiber stimulation, as shown in figure 8.7, the granule cells were activated first ($35 \pm 6.1ms$; n=6) followed by the MLIs ($45.5 \pm 1.5ms$; n=6) and Purkinje cells ($57.5 \pm 2.6ms$; n=6). Thus, MLI excitation was detected $9.8 \pm 3.6ms$ (n=6) and Purkinje cell excitation was detected $13.6 \pm 5.8ms$ (n=6) after granule cell excitation.

In different experiments, after control recordings, the GABA-A receptor blocker gabazine was perfused. Both the amplitude and the percentage of active granule cells cells and Purkinje cells increased after gabazine perfusion. Some neurons were inactive in control condition but their activity appeared with gabazine, attesting to the strong impact of inhibition on the circuit. During washout, all neuronal activities returned to the initial levels, demonstrating full reversibility of drug action and stability of the recordings. Activity maps were reconstructed showing that, with gabazine, the density of active cells and their responses were enhanced. Moreover, with gabazine, the area covered by responding granule cells increased ($+86.3 \pm 15.5\%$, n=6; $p<0.01$), according to the lateral inhibition reported in the granular layer[22].

By exploiting the correlation between time-to-peak of calcium transients and spike number, a 2D spike-emission profile was obtained. In response to a mossy fiber burst, the granule cells emitted a limited number of spikes decreasing from center to surround. The 1-spike intercept fell at $29.4\mu m$ indicating an active core of $58.8\mu m$ diameter[22, 43], and the number of spikes increased with gabazine, which caused all the cells to make at least one spike, and some up to six spikes. Results of the experiments are reported in figure 8.8.

In order to test whether the holographic data could effectively demonstrate the generation of a center-surround structure, a set of recordings,

shown in figure 8.9, was performed using 20x magnification, in which the field of view was significantly larger than the active area and the contour of excitation was defined. Mossy fiber bursts activated a spot of active granule cells, whose intensity rapidly decayed toward the edge of the spot (n=5). After gabazine perfusion, the number of responding neurons increased, the active area became larger and the intensity of activation in the center of the spot became stronger. The combined effect of inhibition in regulating granular layer activity was obtained by generating "E/I" maps, where $E/I = (E_{norm} - I_{norm})/E_{norm}$. Obviously, no response could be observed if excitatory fibers did not reach a neuron, even after gabazine perfusion. The map therefore represented the E/I balance in the area activated by excitatory fibers. This map showed that the excitation core was surrounded by a large and deep area of inhibition. The 5 experiments carried out with the $20\times$ objective were superimposed to obtain a stack image, which was subsequently filtered. The average E/I map showed a clear center-surround structure with active core of 40–60μm diameter, corresponding to that estimated by exploiting the relationship between calcium signal and number of activated spikes.

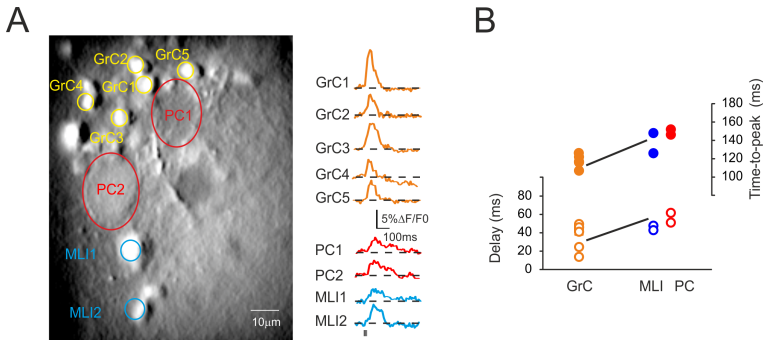

Figure 8.7.: Neuronal activation sequence.

A. Image of a cerebellar slice bulk-loaded with Fura-2AM, in which different cell types can be distinguished. Traces on the right show the signal generated by granule cells, Purkinje cells, and MLIs following stimulation of the mossy fiber bundle (10 pulses at 50 Hz). Different kinetics and peak amplitude are present in responses of different cerebellar neurons. B. The plot shows the time-to-peak (filled circles) and the latency (open circles) of $\Delta F/F_0$ transients in granule cells, Purkinje cells, and MLIs. granule cells activate first and are followed by MLIs and Purkinje cells.

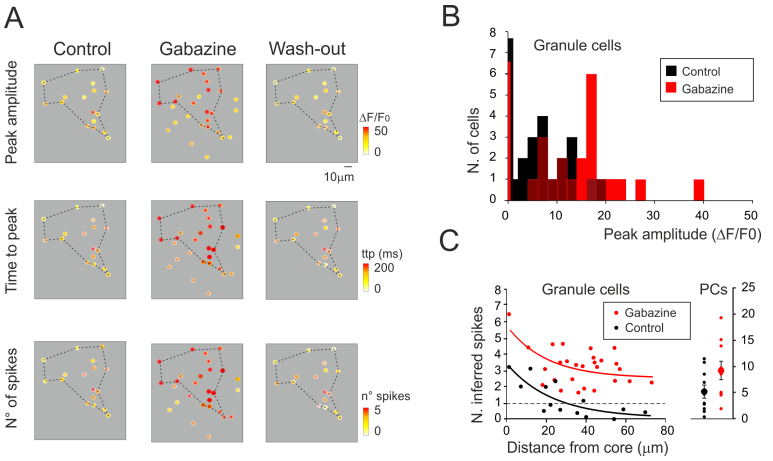

Figure 8.8.: Spatial organization of neuron activity (single experiment)

A. Activity maps of the granular layer (same recordings for granule cells as in figure 8.2, and similar recordings for Purkinje cells) showing the peak intensity of neuronal responses on a color scale. The location of colored dots corresponds to that of neurons in the slice. The panels show that both the activation intensity (upper panels), the time to peak of the response (middle panels) and the inferred number of emitted spikes (lower panels) increase remarkably applying gabazine and revert to control conditions after wash-out. B. The histogram shows the probability of occurrence of response amplitudes in the cell population analyzed in panel A. The distribution shifts toward larger amplitude after gabazine application. C. The plot (on the left) shows the relationship between the number of granule cells spikes (inferred from time-to-peak values of the $\Delta F/F_0$ transient) elicited by mossy fiber stimulation and the distance from center of the responding area. The raster plot (on the right) shows the number of Purkinje cell spikes (inferred from time to peak values of $\Delta F/F_0$ transient) elicited by mossy fiber stimulation. Data are taken from the same experiment shown in figure 8.2 and in the rest of this figure (control, black; gabazine, red). The number of spikes n was inferred using the equation $n = m * ttp + q$, where ttp is the time-to-peak of the $\Delta F/F_0$ transient elicited by mossy fiber stimulation and m and q are the slope and intercept of the average spike/ttp relationship reported in figure 8.4, panel E and figure 8.5, panel E. For granule cells $m = 39.2$ and $q = 56.9$; for Purkinje cells $m = 5.8$ and $q = 75.6$.

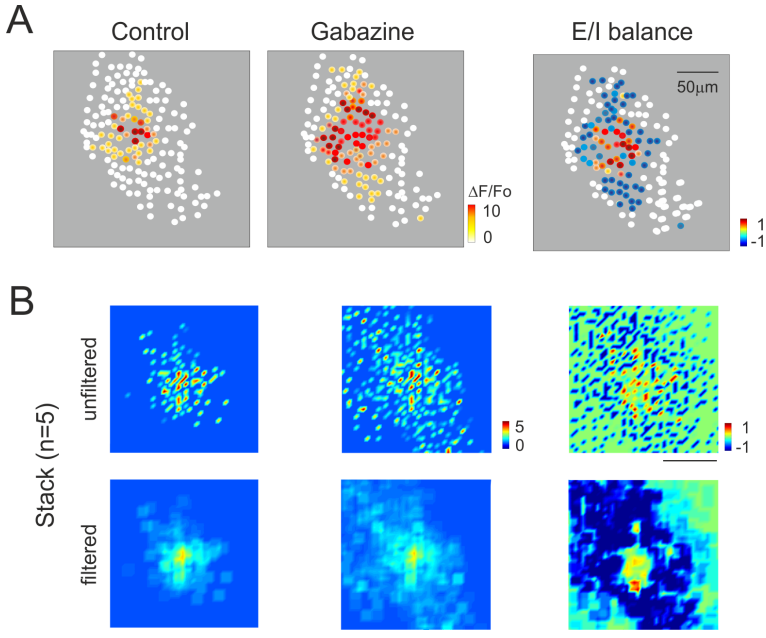

Figure 8.9.: Spatial organization of neuron activity (Statistical)

A. Activity maps of the granular layer with 20x magnification showing the peak intensity of neuronal responses on a color scale. The location of colored dots corresponds to that of neurons in the slice. The left most and mid panels show that the activation intensity, number of active cells and extension of activated area increase remarkably by applying gabazine. The E/I balance plot on the right shows that excitation prevails in the core, while inhibition exceeds excitation in the surround. B. Stacks of results obtained from 5 experiments after data normalization. The panels show on color-scale the average response pattern in control, after gabazine and the E/I balance. The plots are shown both before and after spatial filtering. Note in the filtered E/I balance plot the effective reconstruction of the center-surround structure.

Part III.

EMCCD based sFCCS in hemodynamics

9. Fluorescence correlation spectroscopy

Even though the techniques described in chapter 1 can get diffraction limited images at thousands of frames per second, there are situations, for example blood flow or molecular diffusion studies, in which the objects studied are too small, and/or they move too fast, and the actual detection of their motion is impossible. Nonetheless, if the concentration of the moving objects is low enough, the acquisition of images or signals shows traces of concentration fluctuations, which can be statistically studied to infer information about the motion of the fluorescent objects. This chapter describes the main techniques for the analysis of fluorescence fluctuations, with a particular focus on drift detection and measurement.

9.1. Standard FCS theoretical background

The first, and most used technique based on the study of fluorescence fluctuations is Fluorescence correlation spectroscopy[44] (FCS). Fluorescence correlation spectroscopy is based on the study of the intensity fluctuations of fluorescence generated in a single, diffraction limited, fixed focal volume. The raw data acquired is the intensity of fluorescence emission as a function of time $I(t)$. If the concentration of the fluorophore is low enough, the entrance and exit of fluorescent molecules in the focal volume will produce detectable fluctuations of the signal. In particular, a slowly diffusing, or flowing, specimen will generate faster fluctuations, while the amplitude of the fluctuations with respect to the average signal will be higher when the concentration of the fluorophore is lower. The study of the fluctuations therefore allows the

measurement of concentration, speed and diffusion coefficient of the fluorescent molecules.

In order to perform FCS the autocorrelation function $G(\tau)$ of the fluorescence signal is computed, through the expression

$$G(\tau) = \frac{\langle \delta I(t) * \delta I(t+\tau) \rangle}{\langle I(t) \rangle^2} \tag{9.1}$$

where $\delta I(t) = I(t) - \langle I(t) \rangle$, and fitted with a model function. The autocorrelation function gives a measure of the amplitude of the fluctuations and their average time duration, by comparing the function $I(t)$ with itself at different delay times τ. While model fit functions can be obtained for a variety of photodynamic processes, in this thesis we are mainly interested in variations in fluorophore concentration, usually generated by Brownian diffusion and directional drift. A qualitative description of the autocorrelation function shape is reported in figure 9.1, panel A.

The model fitting function for FCS is the normalized convolution of the excitation volume shape and the correlation function of the fluorophore concentration:

$$G(\tau) = \frac{\int \left| \hat{W}(\vec{q}) \right|^2 R(\vec{q}, \tau) d\vec{q}}{\left| \hat{W}(0) \right|^2 \langle C \rangle^2} \tag{9.2}$$

where $\hat{W}(q)$ is the Fourier transform of the excitation volume, $R(q, \tau)$ is the Fourier transform of the concentration correlation function $P(r, t)$, and $\langle C \rangle$ is the mean concentration of the fluorophore.

Since the concentration correlation function can be obtained by the diffusion equation:

$$\frac{\partial}{\partial t} P(\vec{r}, t) = -div(-D grad\,[P(\vec{r}, t)] + v_{drift} P(\vec{r}, t)) \tag{9.3}$$

where D is the diffusion coefficient, and $v_{drift}$is the drift speed. From

the differential equation the form of $R(q,t)$ can be obtained:

$$R(\vec{q},t) = \langle C \rangle \, exp\left[-D\left|\vec{q}\right|^2 t - i\vec{q}\cdot\vec{v}_{drift}t\right] \tag{9.4}$$

.

Since confocal volumes are generally 3D Gaussian (or a Gaussian Lorentzian shape, in case of two photon excitation, which is generally approximated with a 3D Gaussian for simplicity):

$$W(r) = I_0 exp\left[-2\frac{\left(x^2+y^2\right)}{\omega_0^2}\right] exp\left[-2\frac{z^2}{z_0^2}\right] \tag{9.5}$$

where ω_0 and and z_0 are the beam waist and Rayleigh range of the focused beam, the fitting formula for $G(\tau)$ can be calculated as:

$$\begin{cases} G(\tau) = \frac{\gamma}{\langle N \rangle} G_{diff} G_{drift} \\ G_{diff}(\tau) = \frac{1}{1+\frac{\tau}{\tau_D}} \frac{1}{\sqrt{1+\frac{\tau}{\tau_D}\left(\frac{\lambda}{\pi\omega_0}\right)^2}} \\ G_{drift}(\tau) = exp\left[-\left(\frac{\tau}{\tau_{drift}}\right)^2 \left(\frac{1}{1+\frac{\tau}{\tau_D}}\right)\right] \end{cases} \tag{9.6}$$

where $\langle N \rangle$ is the average number of fluorescent molecules in the excitation volume, $\tau_D = \frac{\omega_0^2}{4sD}$ is the decay time of the diffusion component (s is 1 for one photon excitation, 2 for two photon), and $\tau_{drift} = \frac{\omega_0}{\left|\vec{v}_{drift}\right|}$ is the decay time of the drift component. The factor γ is depending on the shape of the excitation volume, and expressed as:

$$\gamma = \frac{\int I^2(x,y,z)dxdydz}{\int I(x,y,z)dxdydz} \tag{9.7}$$

which is equal to 0.35 for one photon excitation, and 0.076 for two photon excitation.

The free parameters of the fit are therefore the diffusion coefficient D, the average number of molecules in the excitation volume $\langle N \rangle$, and

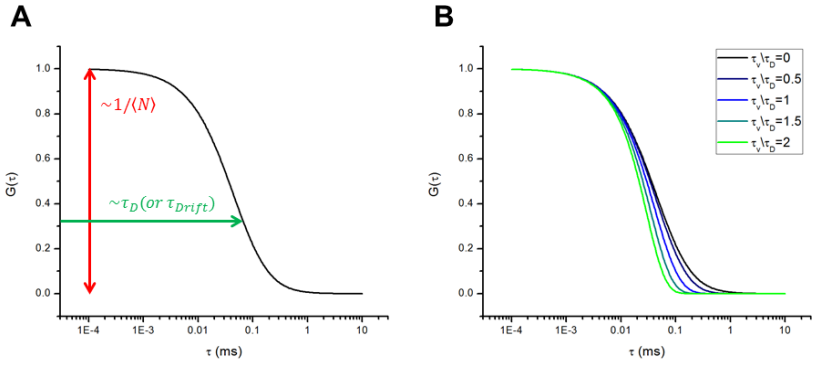

Figure 9.1.: Autocorrelation fit function.

A. Typical shape of an autocorrelation function. Example reported for $G(0) = 1$, $D = 0.3\mu m^2/ms$, $\omega_0 = 0.3\mu m$, $\lambda = 488nm$, with pure diffusion. The amplitude of the function is inversely proportional to the concentration of the dye, while the decay time is inversely proportional to the diffusion coefficient. B. Changes in the function of panel A in the presence of a drift. As the drift speed increases, the function changes from its hyperbolic form to a pure exponential, with decay time τ_{drift}.

the drift speed v_{drift}, and can therefore be estimated from the computed correlation function. Moreover, knowledge of the shape of the excitation volume allows to infer the concentration of the fluorescent specimen from the parameter $\langle N \rangle$.

Some considerations must however be made about the limits of applicability of the technique:

- FLUOROPHORE CONCENTRATION: While FCS works theoretically on any sample concentration, the detector's dark noise imposes a lower bound in usable concentration, since the brightness of very diluted sample can become undetectable. Moreover, since $G(0)$ is inversely proportional to sample concentration, a high sample concentration would lead to a nearly flat decay curve. As a result, FCS should be performed on concentrations ranging from nanomolar to micromolar.

- DETECTORS: Realistic values for τ_D and τ_{drift} are usually ex-

pressed in microseconds, and since that is the decay time of the function, a much higher sampling is required for a good fit. Moreover, the noise induced by the detector must be completely white, in order to avoid correlation contribution coming from the detector. This means that the best detectors for FCS are avalanche photodiodes, while standard photomultipliers should be used carefully, due to their correlated noise at short delay times. Pixelated detectors are too slow for most applications, since they can only achieve millisecond time resolution.

- DRIFT AND DIFFUSION DISCRIMINATION: Since both τ_D and τ_{drift} are free parameters in the fit, it should be possible to obtain, in an FCS experiment, both the flow speed and the diffusion coefficient. However, this is not generally true, as the presence of a directional flow only affects lightly the shape of the decay curve. In particular, when $\tau_D \geq \tau_{drift}$, the diffusion component is undetectable, and if $\tau_{drift} \ggg \tau_D$, the flow speed becomes difficult to obtain. An even bigger problem occurs when the experimenter supposes that the sample presents only Brownian diffusion, while in reality there is a drift occurring. In this case, since the shape of the correlation function in the two cases is not immediately discernible, the presence of a drift can lead to wrong estimations of the diffusion coefficient. The changes in the autocorrelation function generated by the presence of a drift are reported in figure 9.1, panel B.

9.2. sFCCS

As explained in the previous section, in a standard FCS experiment on a flowing sample, it is usually difficult, or impossible, to determine both the drift speed and the diffusion coefficient of the fluorophores. A more specific variant of FCS is spatially resolved fluorescence cross correlation spectroscopy (sFCCS)[45][46], where two different confocal volumes are positioned along the flow direction at a distance $\vec{S}$, the two separate fluorescence signals $I_1(t)$ and $I_2(t)$, and the cross correlation

function G_{X12} is computed as:

$$G_{X12}(\tau) = \frac{\langle \delta I_1(t) \delta I_2(t+\tau) \rangle}{\langle I_1(t) \rangle \langle I_2(t) \rangle} \tag{9.8}$$

.

The test function for sFCCS can be computed with equation (9.2). Since the signals correlated are generated in different points in space, a spatial phase term has to be added in the convolution:

$$G_{X12}(\tau) = \frac{\int \left| \hat{W}(\vec{q}) \right|^2 exp[-i\vec{q}\cdot\vec{S}] R(\vec{q},\tau) dq}{\left| \hat{W}(0) \right|^2 \langle C \rangle^2} \tag{9.9}$$

This leads to a fit function with the same diffusion term as equation (9.6), but presenting a Gaussian drift term, peaking at a delay time corresponding to the average time necessary for a drifting particle to get from one focal volume to another. Supposing $\vec{S}$ parallel to $\vec{v}$:

$$\begin{cases} G_{X12}(\tau) = \frac{\gamma}{\langle N \rangle} G_{diff} G_{drift} \\ G_{diff}(\tau) = \frac{1}{1+\frac{\tau}{\tau_D}} \frac{1}{\sqrt{1+\frac{\tau}{\tau_D}\left(\frac{\lambda}{\pi\omega_0}\right)^2}} \\ G_{drift}(\tau) = exp\left[-\left(\frac{S - v_{drift}\tau}{\omega_0} \right)^2 \left(\frac{1}{1+\frac{\tau}{\tau_D}} \right) \right] \end{cases} \tag{9.10}$$

This means that the resulting fit function presents a peak position determined by the flow speed, and a peak width determined by the diffusion coefficient, thus making it easy to obtain both the diffusion coefficient and the flow speed from the fit, regardless of their respective values. figure 9.2 reports an example of cross correlation function.

While sFCCS is indeed a powerful technique, the necessity of fluorescence detection from two separate focal volumes imposes some technical limitations when using photon counting detectors. In particular, the two focal volumes are usually generated in two predetermined positions by a fixed beam splitter, and the two signals are gathered by two op-

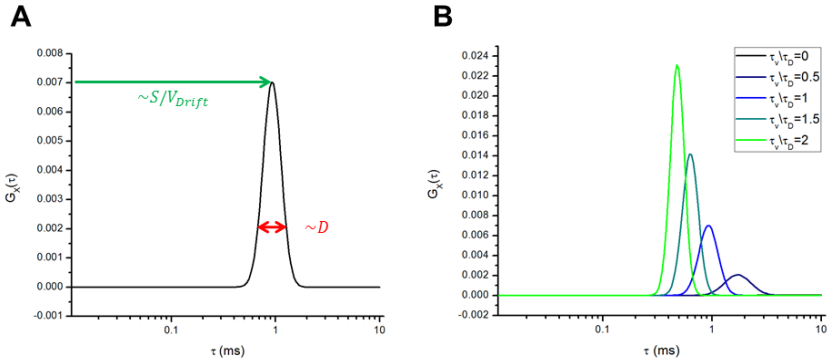

Figure 9.2.: Cross correlation fit function

A. Typical shape of a cross correlation function. Example reported for $G(0) = 1$, $D = 0.3\mu m^2/ms$, $\omega_0 = 0.3\mu m$, $\lambda = 488nm$, $S = 4\mu m$ and a drift speed of $4\mu m/ms$. The peak position is located at the mean time required for the flow to cover the distance between the two spots, while the width of the peak is proportional to the diffusion coefficient. B. Variation in the cross correlation function as a function of the speed. When $V = 0$ there is no correlation peak. It is to be noted hot the diffusion and speed contributions are always separated, leading to an easier fitting.

tical fibers in the image plane, acting as two pinholes, which separate the photons coming from the two volumes in two separate detection channels.

This kind of system is generally difficult to align and calibrate, imposes a limitation to the amount of fluorescence photons gathered, due to the limited numerical aperture of optical fibers, and, most importantly, imposes the use of volumes at a fixed distance, in a fixed direction, therefore requiring the rotation of the sample in order to align the flow direction to the focuses positions.

In chapter 7 and chapter 11, the possibility of overcoming such limitations through the use of movable focal volumes and a pixelated detector is discussed and tested in vivo on zebrafish embryos.

9.3. SLICS

The main disadvantage in sFCCS is the need for a dedicated optical setup. Scan lines image correlation spectroscopy (SLICS)[47] is a very similar technique, which can be performed with a standard confocal microscope, thus proving more versatile.

In a SLICS experiment, the x direction of the scanning head is aligned to the flow direction, and a single line is acquired multiple times at high frequency. The resulting raw data consists in an image obtained by arranging all the acquired lines in a temporal sequence, where the horizontal axis represents a spatial coordinate, while the vertical axis is a temporal coordinate. If fluorescent objects are flowing along the x axis direction, the xt image will present oblique stripes, with an angle in respect to the horizontal depending on the flow speed.

In order to numerically analyze this kind of data, couples of columns, each of which actually represents the fluorescence intensity traces at a single pixel location, are cross correlated and fitted with equation (9.10).

By using the mean of all the cross correlation function obtained by couples of columns at the same distance, the amount of data necessary for the creation of a smooth correlation function can be acquired in a very short time, and different signal distances S can be evaluated in the same experiment. Moreover, as some confocal microscopes allow for the optical rotation of the field of view, SLICS can be performed on flows in any direction, without having to align the sample with the scanning direction.

The downside in SLICS lies in the need for a careful choice of acquisition frequency. If the acquisition frequency is too slow, flowing fluorophores can leave the horizontal field of view in a time shorter than the line acquisition time, thus no correlation would appear. If the acquisition frequency is too fast, the objects would not move at all during the acquisition of the xt image, leading to the presence of vertical stripes in the image, and again no correlation between columns. While in the presence of low concentration, high contrast fluorescent flowing particles the acquisition frequency can be easily selected by looking at the stripes, more concentrated particles leading to low con-

trast images require multiple measurements in order to find a correct frequency setting for acquisition.

9.4. STICS

sFCCS and SLICS can accurately measure flow speeds in a single short segment between two focal volumes, or along a line were the speed is supposed to be constant. This is good for most microfluidics applications, where speed is measured along a smooth duct of constant section. However, sometimes the speed and direction of the flow can vary depending on the position, and multiple sFCCS measures at different angles would be required to completely map the flow behavior.

More information about the spatial distribution of the flow can be obtained by high speed wide field images, with a correlative technique called spatiotemporal image correlation spectroscopy (STICS)[48].

STICS requires a series of confocal images acquired at high frequency, and provides a complete mapping of the flow throughout the confocal plane. In order to do so, the cross correlation function expressed in equation (9.1) is computed between every pixel, and the pixels in a square area of size $2L+1$ pixels around them. The raw data produced is, for every pixel (x, y), a three dimensional correlation stack where the pixel (i, j, τ), with $-L < i, j < L$, is the value of the cross correlation $G_{(x,y,)(x+i,x+j)}$ at delay time τ. If only diffusion is present, the stack will represent a Gaussian shape in the plane (i, j), with increasing variance for increasing values of τ. In the presence of a drift, the peak of the Gaussian moves in the direction of the flow for increasing values of τ. By fitting each (i, j) plane of every correlation stack with a Gaussian, and fitting linearly the position of the peak as a function of τ, the speed of flow, and the diffusion coefficient can be obtained for each pixel.

While the technique is theoretically extremely powerful, it requires high frequency, high resolution, full field images acquisition; setups performances limit its practical usefulness to the study of extremely slow diffusion and drift processes (time scales on the order of seconds or minutes).

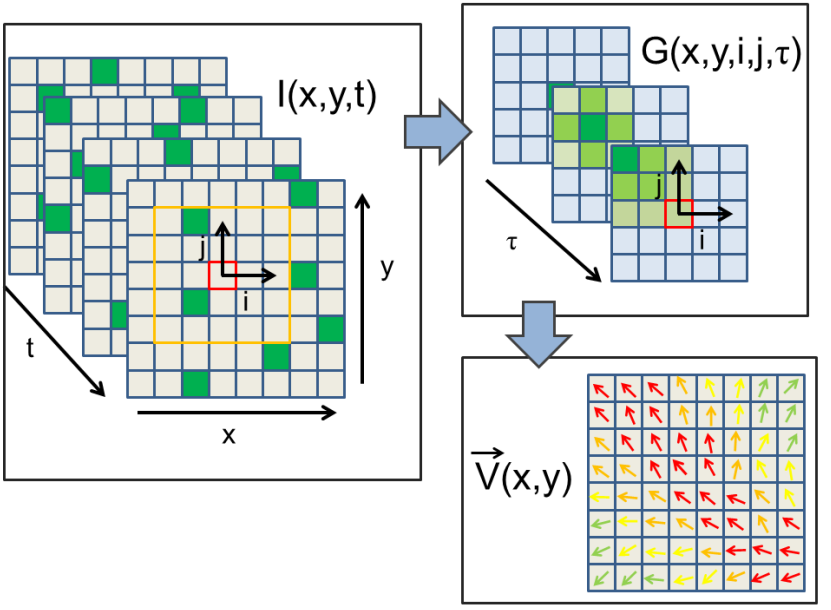

Figure 9.3.: Stics image analysis

A time series of bidimensional images $I(x, y, t)$ is acquired. For each pixel(x, y), the cross correlation function is computed with every pixel $(x+i, y+j)$ with $|i|, |j| < L$, obtaining a cross correlation stack $G(i, j, \tau)$. The position (i, j) of the maxima of the correlation functions is found for every value of τ, the direction and speed of movement of the maxima gives the direction and speed of the flow at the pixel (x, y), resulting in a map of the flow $\vec{v}(x, y)$.

10. Experimental setup

10.1. Setup design

Zebrafish blood flow was studied through sFCCS measurements (a technique described in section §9.2), performed through a pixelated detector, and with the possibility of focal volumes scanning. The standard experiment preceded as follows:

1. Identification of the zebrafish embryo in the agarose gel in transmitted light.

2. Selection of a focal plane where the vessels are on focus through standard two photon microscopy.

3. Positioning of the two focal volume for sFCCS.

4. Optional selection of the scanning amplitude.

5. sFCCS measurement.

The setup required is therefore a two photon microscope, with a splitter before the scanning head, and the possibility to choose between a standard photomultiplier for two photon imaging, or a fast and very sensible detector for sFCCS measurements.

The experiments were performed on a custom made inverted microscope. A standard Kohler illumination optical path provides condensed white light from a fiber coupled halogen lamp, for brightfield illumination porpoises. Fluorescence excitation is provided by a mode locked, $Nd:YAG$ pumped $Ti:Sa$ laser (Tsunami, Spectra Physics), continuously tunable emission wavelength in the 720-1000 nm range, with a peak power of 1.5 W at 800 nm.

The laser beam is splitted by a modified *Twiman-Green* interferometer with tiltable mirrors. A telescope formed by two plano-convex, IR coated lenses ($f_1 = f_2 = 50cm$) conjugates the plane of the mirrors of the interferometer with the plane where two galvanometric mirrors (6350, Cambridge Technology, Watertown, Massachusetts) are placed. This way two independent collimated beams are always impinging at the center of the first mirror, and their angle of incidence can be separately and finely regulated through the interferometer mirrors.

The plane between the galvanometric mirrors is conjugated with the objective (Olympus XLUMPlanFl 20x, 0.95 N.A.) back aperture through a reflective scanning head based on two concave mirrors ($f_1 = 7.5cm$, $f_2 = 15cm$), optimized for the 750 nm-1500 nm wavelength interval, which corrects for the astigmatism introduced by the finite distance between galvanometric mirrors.

Fluorescence light is reflected by a dichroic mirror (750dcspxr, Chroma), and an image of the objective focal plane is generated by a tube lens ($f = 20cm$). A flippable mirror allows to choose between the use of a photomultiplier(H7421, Hamamatsu), or an EMCCD detector (Cascade II 512B, Photometrics).

The EMCCD detector used is extremely sensitive, with a quantum efficiency >90% in the 500 nm-700 nm spectral range, and an effective noise $< 1e^-$rms. The chip is formed by 512x512 pixels, of $16x16\mu m$ size each, and has a temporal resolution of 4 ms when acquiring on a 20 lines subregion of the chip.

The setup can be used in four different modes:

- STANDARD TWO PHOTON MICROSCOPY: The mirrors of the interferometer are placed at the same angle, so that only one focal point is formed on the image plane. The photomultiplier is used for detection, and the focal volume is raster scanned on the sample in order to create a standard two photon image.

- SCANNED LIGHTSHEET: As in standard two photon microscopy mode, only one focal volume is generated and raster scanned on the sample, but light detection is performed with the EMCCD detector. The whole EMCCD detector is exposed, and exposure

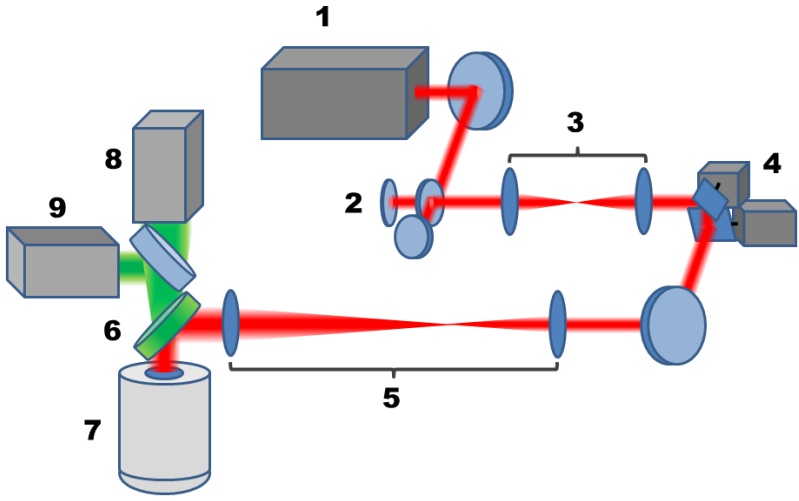

Figure 10.1.: Schematic of the Cross correlation setup.

1. Laser Source (Tsunami, Spectra Physics). 2. Twiman-Green interferometer. 3. Telescope (f1 = f2 = 50 cm). 4. Galvanometric mirrors (6350, Cambridge Technology, Massachusetts). 5. scan head. 6. dichroic mirror (750dcspxr, Chroma). 7. Objective (XLUMPlanFl 20X, Olympus). 8. EMCCD camera (Cascade II 512B, Photometrics). 9. Photomultiplier (H7421, Hamamatsu).

lasts as long as a complete raster scan of the field of view. This creates a confocal two photon image, but the image quality is affected by fluorescence light scattering. While the image has lower quality than a standard two photon image, this imaging mode generates images on the EMCCD chip, therefore allowing to choose the position of the two focal volumes for sFCCS. As a standard procedure a full field image is acquired, then a point-like field of view is selected, by stopping the galvanometric mirrors, near the position of the two spots locations, and the interferometer mirrors are used to place the two focal volumes on the desired pixels.

- Standard sFCCS: Once the two spots positions are selected, the chip binning is increased until the vertical distance between

the focuses is shorter than 20 pixels. A 20 pixel high region containing the two pixels is selected, in order to achieve the maximum possible frame rate (4 ms per frame). The signals are then acquired and cross correlated.

- Scanning sFCCS: if the two spots are separated vertically on the chip, they can be scanned horizontally through the galvanometric mirrors. The scanning is synchronized with the camera acquisition, so that a single horizontal line is scanned for each frame. This way each image presents two horizontal bright lines, and multiple measures of sFCCS can be performed in parallel on adjacent couples of pixels. This is particularly useful in order to acquire the speed profile of the flow.

10.2. Setup characterization

Test measurement were performed on different flowing specimen in a borosilicate glass capillary. The capillary used had a square section, to avoid optical aberrations. Capillaries were $5cm$ long, with an internal section side of $800\mu m$. In order to achieve a finely tunable flow speed, the capillary extremities were connected by Teflon tubing to two horizontally mounted, graduated,$4mm$ diameter transparent tubes, acting as fluid reserves. The vertical distance between the reserves can be finely adjusted, and the effective flow speed can be calculated from the volume flowing over a given time.

The system was tested by measuring flows in different conditions, the parameters considered were:

- The flow speed
- The diffusion coefficient of the fluorophores
- the distance between excitation focuses.

Flow speed measurements

Measurements of the flow speed V were performed on fluorescent microbeads ($\emptyset = 30nm$), measures are shown infigure 10.2. Excitation volumes were positioned at a distance $S = 16\mu m$. Flow speed was modified by changing the relative vertical position h between the reserves from $-3500\mu m$ and $5000\mu m$ in $500\mu m$ steps.

No flow was present for $-1000\mu m < h < 2500\mu m$. In this case, wall adhesion and capillary effects[49, 50, 51] interfere severely with the viscous flow and the fluid speed effectively vanishes. The estimate of the capillary pressure to be overcome, due to adhesion between water and the wall of the syringe, is $\approx 4(\gamma_{sg} - \gamma_{sl})/d_s$, where γ_{sg} and γ_{sl} are the surface tensions between plastic (solid) and air (gas), and between plastic and water (liquid) and d_s is the reservoir diameter ($d_s = 4000\mu m$). For polymethyl-methacrylate (PMMA)[51], $(\gamma_{sg} - \gamma_{sl}) \approx 0.02 J/m^2$ and the pressure difference amounts to $\sim -20 N/m^2$. This value corresponds to $2000\mu m$ of water height that compares well with the height gap in which we cannot measure any water flow.

In the $-3500\mu m < h < -1000\mu m$ and $2500\mu m < h < 5000\mu m$ ranges, a linear relationship between h and V was found, as expected from a Poiseouille flow, with respective slopes of $0.55 \pm 0.08 s^{-1}$ ad $0.42 \pm 12 s^{-1}$.

These values can be compared to the prediction made according to Poiseuille law for a square capillary of size d connected to two reservoirs. The flow is determined by the pressure gradient due to the relative height h of the two reservoirs, $\Delta P = \rho g h/L$, where ρ is the density of the fluid, here taken as that of water, g is the gravity acceleration, and the tubing length is $L \approx 0.69m$ in our setup. The estimated maximum speed in the capillary is then $V_{max}(h) = h[(\rho g/L\eta)0.084]d^2$. For the present case (the real size of the capillary is $d = 800\mu m$, the prediction $V_{max}(h)/h = 0.60 \pm 0.06 s^{-1}$ is in reasonable agreement with our experimental findings $V_{max}(h)/h = 0.51 \pm 0.07 s^{-1}$.

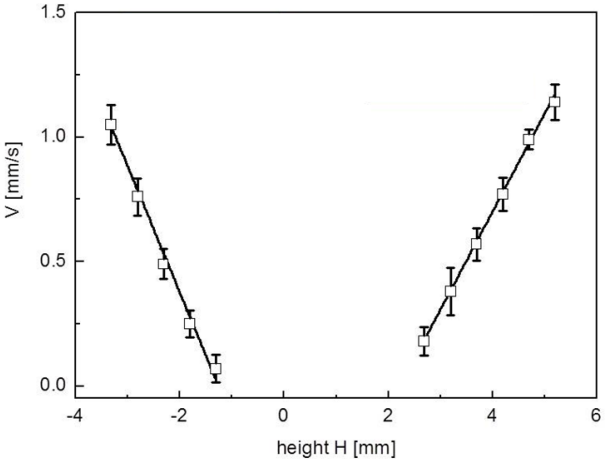

Figure 10.2.: Flow speed measurements.

Drift velocity measured on $30nm$ fluorescent microbeads suspension flowing in a square capillary (Size $720 \pm 20\mu m$). as a function of the difference in height of the two reservoirs. The distance between the two laser focuses is $16\mu m$.The CCFs were fitted to equation (9.10) in order to obtain the drift speed. Solid lines correspond to the linear fit to the drift speed in the regions $H > 0$ and $H < 0$.

Diffusion coefficient measurements

In order verify the possibility, for the system, to measure the diffusion coefficient, sFCCS measurements were performed on a solution of highly diffusing molecules (30 nM Rhodamine 6G), and on a suspension of slowly diffusing gold nanorods (approximate dimension 10x50 nm), showing extremely bright two photon luminescence signal.

Both measurements, shown in figure 10.3, led to estimates of the diffusion coefficient compatible with literature, as well as with our independent estimates[52, 53, 54]. In particular the best fit for rhodamine diffusion coefficient was $(310 \pm 30) * 10^{-12} m^2/s$, while the one for gold nanorods was $(12 \pm 1) * 10^{-12} m^2/s$.

It is important to notice that, in the case of rhodamine, the diffusion time for a focal volume of $0.6\mu m\omega_0$ is $\sim 75\mu s$, much lower than the time resolution of the EMCCD. While in this situation an autocorrelation measurement in impossible, sFCCS measurements are always possible even with low time resolution, at the only condition of positioning the focal volumes at a convenient distance.

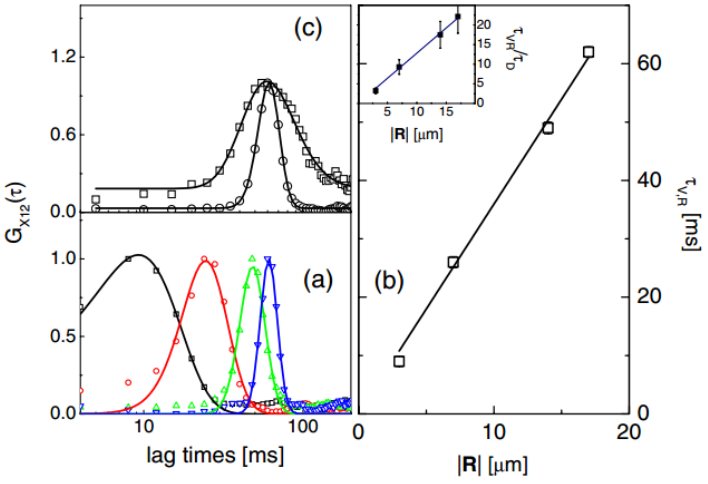

Figure 10.3.: Diffusion coefficient and spot distance measurements

Experiments on gold nanorods ($\approx 16nm \times 48nm$) in square microcapillary. (a) Normalized CCFs acquired from spots at distances $|R| = 3, 4, 14, 17\mu m$ (squares, circles, up and down triangles, respectively), collinear to the flow in the microcapillary. Solid lines are best fit of equation (9.10) to data ($\omega_0 = 0.6\mu m; \lambda_{exc} = 0.8\mu m$). (b) reports the best fit values of the flow speed obtained from τ_{VR} as a function of $|R|$. The solid line is the best fit with slope $3.59 \pm 0.04 ms/\mu m$. Inset: ratio of the best fit drift over diffusion times τ_{VR}/τ_D as a function of the interspot distance. The solid line is the linear trend $\tau_{VR}/\tau_D = |R|\,(8D/V\omega_0^2) \approx |R|\,(1.3 \pm 0.1)$. (c) Normalized cross-correlation signal from gold nanorods (circles, $|R| = 12\mu m$), and rhodamine 6G (squares, $|R| = 24\mu m$) in water solution (beam waist $\omega_0 = 0.6\mu m$). Solid lines are the best fit to equation (9.10). Fitted diffusion coefficients are $(310 \pm 30) \times 10^{-12} m^2/s$ for rhodamine 6G and $(13 \pm 1) \times 10^{-12} m^2/s$ for gold nanorods.

Interspot distance

We used the gold nanorod suspensions as a test of the invariance of the flow speed measurement on the distance between the two spots, results are reported in figure 10.3. The actual value of the speed, $V_{exp} = 280 \pm 50 \mu m/s$, was obtained by directly measuring the volumetric rate of the hydraulic system. Cross-correlation functions were computed at different distances between the excitation spots in the range of $3\mu m < |R| < 17\mu m$. The separate fits of the four CCFs give best fit drift times τ_{drift} that depend linearly on the interspot distance. The slope of the linear trend corresponds to an average drift speed $V_{fit} = 280 \pm 10 \mu m/s$ and diffusion time obtained from the best fit of the CCFs is $\tau_D = 3 \pm 0.5 ms$ (the uncertainty corresponds to the standard deviation computed over different interspot distances). A global fit to the whole set of CCFs leads to very similar results (best fit $\tau_D = 3ms$, $V_{fit} = 270 \pm 80 \mu m/s$). The drift speed is very well retrieved from the analysis of the CCFs in a wide range of the τ_{drift}/τ_D ratio ($2.5 < \tau_{drift}/\tau_D < 17$). The best fit slope is $\partial(\tau_{drift}/\tau_D)/\partial |R| = (1.3 \pm 0.1) \mu m^{-1}$, in good agreement with the expected value of the ratio $\frac{8D}{v\omega_0} = (1.0 \pm 0.2) \mu m^{-1}$.

Scanning sFCCS

As reported in section §10, the system can operate in scanning sFCCS mode, scanning the two focal volumes along the horizontal direction of the field of view with the galvanometric mirrors, at a frequency equal to the acquisition frequency of the camera. The images acquired present therefore two bright parallel lines instead of two bright spots, and if the flow is perpendicular to the scanning direction, FCCS can be performed on each couple of pixels along the flow direction, thus obtaining a flow speed profile, which can be used to estimate the shear stress at the interfaces.

The system was tested on fluorescent microbeads ($\emptyset = 30nm$) suspended in water. Measures and a sketch of the system are shown in figure 10.4. The flow speed was measured directly from the lag time of the maximum of the cross correlation functions in order to reduce the computational time of the procedure. Moreover, the direct fitting

of the correlation curves, as compared to the maximum estimate, leads to drift time underestimated by only 0.3% to 0.9%. The flow speed values as a function of the radial distance (z) from the center of the capillary have then been fit to the trial function[51]:

$$V_z = V_{max} sin\left[\pi \frac{(z - z_0)}{d}\right] \tag{10.1}$$

.In this equation, which is an extension of the known parabolic profile observed in circular cross-section capillaries,d and V_{max} are the size of the capillary and the maximum speed of the fluid (at the center of the capillary). The position of the center of the capillary section z_0 is not known and is used as a best fit parameter, which is the radial coordinate of the maximum speed in the capillary. The best fit of equation (10.1) to the data gives $d = 720 \pm 20 \mu m$, $V_{max} = 464 \pm 5 \mu m/s$, and $z_0 = 482 \mu m$. This fit offers an estimate of the actual internal size of the microcapillary that is 10% lower than nominal data. The forced fit of the data) while keeping d fixed at the nominal sized $800 \mu m$ gives clearly unsatisfactory results.

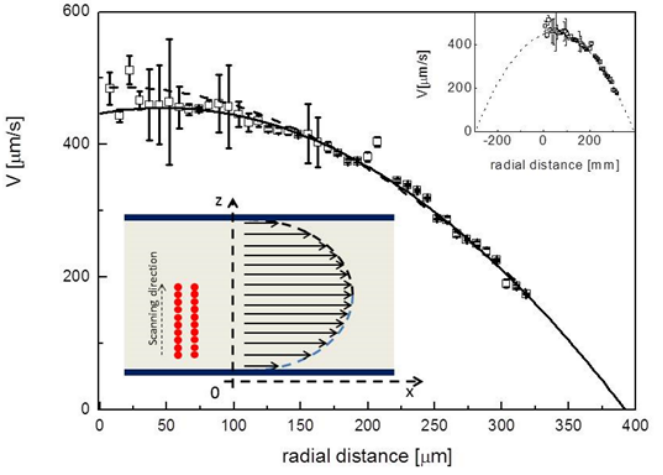

Figure 10.4.: Scanning sFCCS measurement in a glass capillary

Characterization of the speed profile of the section of the glass square capillary. The flow speed was obtained directly from the lag time of the maximum of the CCFs. The CCFs over almost half of the capillary section were computed in parallel on two corresponding spots lying along the flow direction that were scanned in a direction perpendicular to that (see sketch). The solid line is the best fit to the data of 10.1 with best fit values of $z_0 = 48 \pm 2\mu m$, $d = 720 \pm 20\mu m$, and $V_{max} = 464 \pm 5\mu m/s$. The dashed line is the best fit of the data to10.1 with d kept fixed at $800\mu m$. The inset reports the data superimposed on the extrapolation of the best fit profile over the whole capillary width.

11. sFCCS experiments in zebrafish embryos

The dual spot setup described previously was employed for hemodynamics studies in zebrafish embryos. Most of the results reported in this chapter were published as a peer reviewed article in "Journal of Biomedical Optics"[55].

11.1. Veins blood flow measurements

We applied CCD cross-correlation spectroscopy to study blood flow in zebrafish embryos vessels. For this purpose, we have employed transgenic embryos whose blood red cells express dsRed protein. dsRed fluorescence is primed by two-photon excitation at $\lambda_{exc} = 900nm$ and the emission is collected at$\lambda_{em} = 600nm$ through a HQ600/40filter (Chroma, Bellows Falls, Vermont). The two spots of the infrared laser were set at variable distances along the vessel axis in the middle of the vessel cross-section and along the blood flow direction. Coarse adjustment of the spots along the flow lines was reached by moving the embryo and finer tuning was obtained by moving one of the spots in the focal plane by means of the interferometer mirrors. We tested at first the accuracy of the blood flow speed measurements on a single embryo by performing repeated measurements on the embryo's vein at increasing distances between spots. All the CCFs have been analyzed according to equation (9.10) in the range of $6\mu m \leq |R| \leq 24\mu m$, and in this range, the average value is determined with under 3% uncertainty on the single embryo. The data reported correspond to a 4 days post fertilization embryo and $V = 640 \pm 20\mu m/s$ (3% uncertainty). The diffusion time in the analysis of all the CCFs is kept at $\tau_D \approx 0.1ms$.

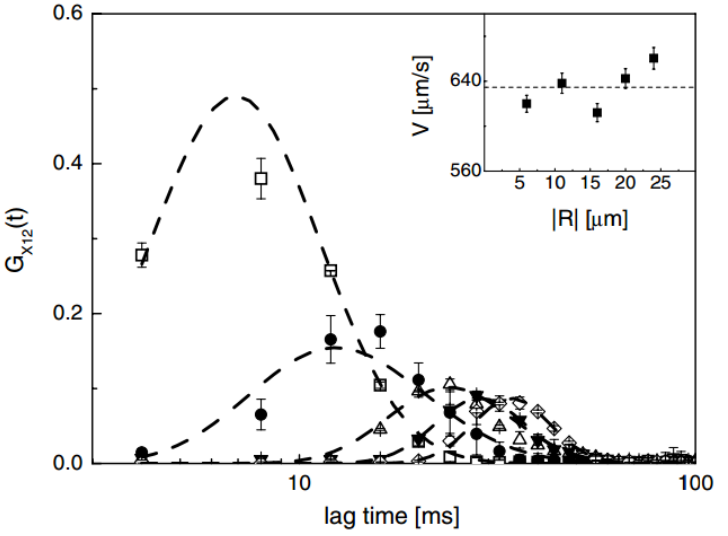

Figure 11.1.: Measures in zebrafish veins.

CCFs computed on vein blood vessels of a zebrafish embryo (four days postfertilization) at increasing values of the distances between the laser spots. The different symbols refer to $|R| = 6\mu m$ (open square), $11\mu m$ (filled circles), $16\mu m$ (open up-triangles),$20\mu m$ (filled down-triangles), and $24\mu m$ (open diamonds). The error bars correspond to an average over three different measurements on the same embryo. The dashed lines are the best fit curve to 9.10. The inset reports the best fit values of the drift speed obtained from fitting the cross-correlation to 9.10. The dashed line indicates the speed average value.

11.2. Arteries blood flow measurements

When performing sFCCS on arteries instead of in veins, the cross correlation functions show a more complex behavior, which require a more thorough discussion. For this purpose, the biological variability of the data was evaluated. Averages of the flow parameters over three to four different embryos at the same developmental stage were considered. From the fluid-dynamics point of view, the major difference between the two vessels is the presence of a double peak in the CCF measured on the artery. In the vein, far from the tail, we find a single peak

that corresponds to a drift speed of $V_{vein} = 630 \pm 70 \mu m/s$. On the contrary, in the artery, two peaks in the CCFs are found, suggesting the presence of two phases in the blood flow. According to the literature[56, 57], these phases can be ascribed to the systole (faster phase) and diastole (slower phase) phases. The data taken in the embryo artery was analyzed according to a drift model (equation (9.10)) with two drift components (the same diffusion time was taken for both the drift components of the CCFs) at different distances from the tail capillary bed. The CCFs collected at 50% of the heart-tail distance are reported. The analysis of these functions gives $V_{syst} = 1420 \pm 200 \mu m/s$ and $V_{diast} = 380 \pm 20 \mu m/s$. When we perform the same experiment at 20% of the tail-heart distance, we still obtain two drift components with much more closely spaced speed values. The average values of the systole and diastole speeds are, in this case,$V_{syst} = 980 \pm 120 \mu m/s$ and $Vdiast = 420 \pm 40 \mu m/s$. The systolic component shows a larger decrease when approaching the tail, compared to the diastolic component that is almost constant. The averages taken over three to four different embryos at the same developmental stage show larger uncertainty (10%) than those obtained from repeated blood flow speed measurements on the same embryo. The figure of 10 to 12%, therefore, represents the biological uncertainty on the blood flow measurements.

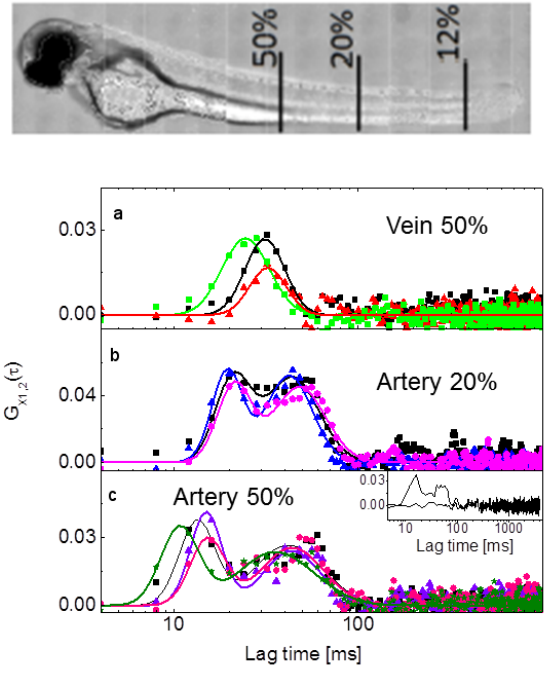

Figure 11.2.: Measures in veins and arteries.

CCFs measured in vessels of different zebrafish embryos at four days postfertilization (d.p.f.) ($|R| = 20\mu m$). Examples of CCFs measured in the vein are reported in (a) together with their best fits. The average value of the drift speed is $V_{vein} = 630 \pm 70\mu m/s$. Examples of the CCFs measured in the artery close (20% tail-heart distance, see image) to embryo's tail are reported in (b). The average value of the best fit systolic and diastolic speeds are$V_{syst} = 980 \pm 120\mu m/s$ and $V_{diast} = 420 \pm 40\mu m/s$, respectively. Examples of the CCFs computed in the artery at half way between embryo heart (50% tail-heart distance, see image) are reported in panel (c). The average value of the best fit systolic and diastolic speeds are $V_{syst} = 1420 \pm 200\mu m/s$ and $Vdiast = 380 \pm 20\mu m/s$, respectively. Inset in panel (c) report the comparison of the CCFs $G_{X12}(t)$(thin line) and $G_{X21}(t)$(thick line). The latter function does not show a correlation peak, confirming the direction of the flow. The image reports the transmitted light image of a zebrafish embryo at 4 d.p.f. (size≈3.5mm).

11.3. Strain rate estimates

Plasma shear stress is a relevant parameter for hemodynamics since it can trigger the response of a number of proteins on the vessel epithelium[56, 58, 59]. In the literature, various methods have been applied to monitor the flow speed in microfluidic setups and even in animal models[60, 61, 62, 63]. Beside a few applications of laser speckle imaging[64], fluorescence detection in cytometry[65] and nuclear magnetic resonance[66], PIV[59, 61, 62, 63] has been widely applied to follow injected nanospheres and platelets and/or blood red cells observed in transmission optical microscopy and tomography[26]. Microinjection of particles needed for PIV could alter physiology due to unavoidable spheres'aggregation[60], and correlation methods applied to cells flowing in the blood stream should be preferred for physiologically relevant insights[26]. CCFs of red blood cells fluorescence were measured both in the dorsal vein and in the caudal aorta at half way between the zebrafish tail and heart, far enough from the pulsation origin (the heart) and the tail capillary bed, which has a large hydraulic compliance. The edges of the vessel were detected by following the abrupt fall of the value of the CCF amplitude $G(0)$, and the parallel increase in the relative uncertainty on the drift speed, that occurs when we focus the laser spots outside the vessel. For each pixel, the CCFs were fit to equation (9.10) with one (for the vein) or two (for the artery) drift components. We have checked that the blood flow was perpendicular to the two scanned lines across the vessel by computing CCFs of adjacent pixels,$G^{i\cdot i\pm1}_{X1,2}(\tau)$. The peak amplitude of the CCF decreased by increasing distances between the pixels with $peak(G^{i\cdot i}_{X1,2}) = 0.08 \pm 0.01$, which is larger than $peak(G^{i\cdot i-1}_{X1,2}) \approx peak(G^{i\cdot i+1}_{X1,2}) = 0.042 \pm 0.005$ and $peak(G^{i\cdot i-2}_{X1,2}) \approx peak(G^{i\cdot i+2}_{X1,2}) = 0.009 \pm 0.004$. The radial profile of the speed is well reproduced in embryos of similar ages. We assume a linear relationship between the shear stress and the strain rate. In this way, we can obtain the shear stress[67, 68] from the measurement of the steepness of the flow speed profile in the vessels of zebrafish embryos. We measure here an effective shear stress since we are following the motion of red blood cells (RBCs) that are comparable in size with the

vessel diameter. The maximum effective strain rate in the vein, $\gamma = |(\partial V/\partial r)[r_0 \pm (d_V/2)]| = 4\{V(r_0) - V[r_0 \pm (d_V/2)]\}/d_V = 15 \pm 3s^{-1}$, is intermediate to those relative to the systole and diastole pulses measured in the artery,$|(\partial V/\partial r)[r_0 \pm (d_V/2)]| = 34 \pm 6s^{-1}$ (systole) and $|(\partial V/\partial r)[r_0 \pm (d_V/2)]| = 8 \pm 3s^{-1}$ (diastole). This can be due to the fact that the heart pulsation is much more effective in the artery than in the vein and that the volumetric flow rate is much lower in the systole than in the diastole phase[69]. The values of the strain rate found here, when converted to shear stress (RBC viscosity$\approx 5 \times 10^{-3} Pa \cdot s$)[68], give values of ≈0.05 to 0.15 Pa that are lower than those (≈1Pa) derived for rabbit arterioles (larger than zebrafish vessels) by Tangelder et al.[59] and those measured in the aortic arch in zebrafish 4 d.p.f. by Chen et al. by μ-PIV[69]. These studies correspond, however, to higher pressures and reproduced the speed profile more closely than was done here since the tracked object (platelets or microbeads) is much smaller than the vessel diameter. Moreover, one should take into account that the wall shear stress measurement based on RBC tracking is an effective value[67]. The measured speed does not vanish at the edge of the vessel and the ratio of maximum velocity to the marginal velocity is $\chi = V(r_0) - V(r_0 \pm (d_V/2)) \approx 1.2 \pm 0.05$ for both the vessels. This has been observed earlier[59, 67, 70, 71] in similar cases. Zhong et Al.[70] reported detailed speed profiles in 32- to 120-μm-diameter retina veins obtained by tracing the motion of red blood cells on optical scanning microscopy images, finding $\chi \approx 1.36$ for 32μm diameter capillaries and $\chi \approx 2$ for very large capillaries (the values should tend to infinity in a Poiseuille regime). A model developed by Yen et al.[72] and generalized by Zhong et al.[70] relates χ to the vessel diameter d_V.

$$\chi \cong 2\left(1 - 0.5328 exp\left[-\sqrt{0.00435 d_V}\right]\right)$$

In the case reported, the vessel diameter is $d_V \approx 12 \pm 2\mu m$ for the vein and $d_V \approx 13 \pm 3\mu m$ for the aorta at midway between the tail and the heart, leading to $\chi \approx 1.25$, which is very close to our experimental result. The simplest rationalization of the reduced value of the speed ratio χ is related to the finite size of the RBCs. The size of the vessels

is, on the average, only twice the size of the red blood cells: the red blood cells are, therefore, most of the time rolling over the epithelium along the vessel. The minimum distance from the epithelium at which we can measure the flow speed is then only half the red blood cell size. For a circular capillary of diameter d_V in Poiseuille regime, the speed profile is $V(r) = V_{max}[1-(2r/d_V)^2]$ and the minimum speed value measurable due to the finite size of the red blood cells should then be $V_{min} = V_{max}\left\{1-[(d_V-\delta_{RBC})/d_V]^2\right\}$. For the present case, these estimates lead to $\chi \approx 1.6$, a value that, though not so low as the one found experimentally, is much less than the one corresponding to pure Poiseuille flow in no-slip boundary conditions. In larger capillaries, additional hydrodynamic effects (reduced effective viscosity close to the vessel walls) can partially contribute to the reduction of χ[59, 70, 73]. In the above measurements, we exploited dual line scanning coupled with CCF computation on the EM-CCD frames.

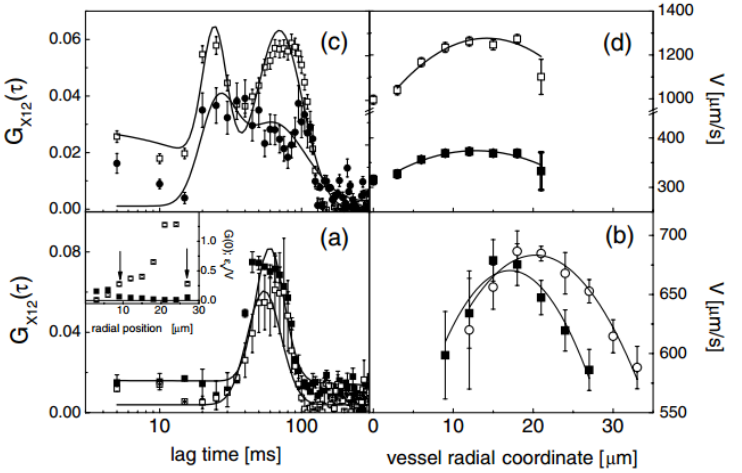

Figure 11.3.: Strain rate estimates.

Speed profile across veins and arteries measured at 50% of heart-tail distance in zebrafish embryos (developmental stage: 4 d.p.f., $|R| = 40\mu m$). (a) reports two exemplary CCFs measured in zebrafish veins at a distance $\approx 0.25 d_V$ (open squares) and $\approx 0.125 d_V$ (filled squares) from the vessel wall (d_V is the estimated vessel diameter). Solid lines are the best fit to 9.10 with a single drift component. Inset: plot of the CCF amplitude,$G(0)$, and the drift speed uncertainty,$\varepsilon V/V$, obtained from the data fitting as a function of the radial distance across the vessel. The vertical arrows indicate the estimated position of the vessel wall. (b) Profile of the best fit speed values in veins measured on two (4 d.p.f.) zebrafish embryos. Each set of data is the average of three different scanning on the same embryo. The solid line is the best fit of the data to the trial function $V(r) = V_{max}[1-(2r/d_V)^2]$. (c) Two exemplary CCFs measured in zebrafish arteries at $\approx 0.25 d_V$ (open squares) and $\approx 0.125 d_V$ (filled squares) from the vessel wall. Solid lines are best fit to 9.10 with two drift components corresponding to the systole (higher values) and diastole (lower values). (d) Profile of the best fit speed values (open squares, systole and filled squares, diastole) measured on a 4 d.p.f. zebrafish embryo. The data are the average of three different scanning on the same embryo. The solid line is a parabolic fit to the data according to the same trial function as in (b).

Part IV.

Conclusion

12. Future outlook

Holographic microscopy

The two photon holographic setup described in this thesis was realized, tested, and employed in neurobiological research, producing significant data published in peer reviewed journal, proving its reliability and the possibility to use it for future research. Moreover, being based on a particularly simple design, it shifts the balance in complexity from the hardware to the software component of the system. This means that its alignment, maintenance and operation procedures are easier compared with other custom made setups, allowing for their use from researchers with limited experience in optics.

The future applications of the technique are numerous, in particular, without further modifications to the setup or the samples, preliminary results showed that it is possible to use the system to study long term synaptic plasticity. The use of genetically modified mices or adenovirus injections could allow to use calcium sensitive fluorescent proteins, leading to an easier preparation of the sample and better fluorescence signals. Moreover, specific marking with fluorescent proteins would allow to identify different cell types inside the granular layer, leading to a better understanding of the working mechanisms of the network. Preliminary measurements with GlyT2 mices expressing GFP in inhibitory cells showed that the system is capable to easily identify single fluorescent cells in the granular layer.

Preliminary measurements with commercially available voltage sensitive dyes showed that membrane voltage monitoring can not currently be achieved with holographic microscopy. In the future, on the chance that dyes with better two photon efficiency will become available, as well as more sensitive fast pixelated detectors, the system could aim to single action potential detection over multiple neurons in a working

network.

Finally, with appropriate surgery protocols, in vivo microscopy would permit to study the network in a closed loop environment.

As for the strictly technical evolution of the setups, several improvements can be made to the system.

In particular, the main and most immediate improvement can be obtained with an high speed spatial light modulator. The SLM employed in the reported setup has a refresh rate of 60 Hz, thus limiting the acquisition speed for full field two photon images to one frame in several seconds. The development of faster SLM, with refresh frequency of several hundreds frames per second allow two photon imaging at a speed equal or higher to the one of a standard two photon microscope. Given the construction simplicity of an SLM setup, and its reliability, SLM microscopes could become a cheaper and simpler alternative to standard laser scanning microscopes.

Another improvement to the system could be achieved in three dimensional imaging. At the moment, the generation of three dimensional images through holographic movement of the focal plane, is limited by the fixed focus position of the camera detector, and by the strong spherical aberrations introduced by modern objectives while imaging outside its designed focal plane. The camera focus could easily be varied with an adaptive lens used as tube lens of the system. Spherical aberrations on the excitation path could be prevented by applying adaptive optics principles in the calculations of phase masks. A characterization of the objective would allow to compensate for the spherical aberration without the need for a wavefront detector. However, fluorescence light would still create an aberrated image on the detector. The only way to prevent such problem would be the addition of a deformable mirror on the optical path, correcting aberrations of both the excitation and emission light.

A final, more radical evolution of the idea would be the realization of a single photon variant of the setup, which would allow for the use of existing voltage sensitive dyes. In theory, using an SLM designed for visible light, the system should be able to acquire images and to illuminate multiple points of interests simultaneously. The pinhole present

in traditional single photon microscopes could be replaced by the use of a single pixel of an high resolution detector for the acquisition of each signal. However, the acquisition speed of CCD and CMOS camera depends on the number of pixels employed, so that millisecond time resolution can be achieved only with low spatial resolution (100x100 pixels, in the case of the measurements reported in the thesis), which, in case of one photon excitation, would correspond to the use of large diameter pinholes, thus generating a loss in axial resolution. The realization of a single photon holographic microscope based on a similar setup to the one reported here will therefore be possible only after an improvement in the existing pixelated detectors technology.

Cross correlation spectroscopy

The reported measurements of sFCCS microscopy were performed on live genetically modified healty Zebrafish embryos, as a proof of concept of the accuracy and versatility of the setup. Since the zebrafish is an easily modifiable organism, models of existing genitical cardiovascular diseases could be developed and studied through sFCCS, in order to better understand their effects on microcirculation.

In the measurements reported on this thesis, the accuracy in the estimate of strain rates is mainly limited by the fact that the fluorescent flowing specimens are red blood cells, which diameter is comparable with the vessel dimension. The use of microinjected smaller molecules, or genetically modified specimens expressing fluorescent proteins directly in the blood plasma, could dramatically increase the performances of the system.

Due to the multiphoton excitation employed in the system, measures of interest could be performed in easily accessible vessels of more complex organisms, such as the skin vessels of murine models, or retinal vessels, employing some corrective optics for microscopy through the cornea. With surgery procedures even the epatic microcirculation could be accessed.

The introduction of a spatial light modulator, as the one used in this thesis for calcium imaging, could make simultaneous measurements

on multiple vessels possible. More complex flow patterns could be studied with STICS analysis, using a dedicted SPIM setup, already in development in the lab, with promising preliminary results. This would however limit the axial and lateral resolution, and limit the applicability of the technique to transparent, gel mounted samples.

13. Conclusions

The aim of this thesis was to provide new optical microscopy techniques for the study of fast processes in biological samples. In particular two different setup were designed and realized, one intended to perform high speed calcium imaging, and the other for sFCCS measurements in flowing samples. Both setups are based on multifocal two photon excitation and on fluorescence detection with a pixelated detector, and their main differences lie in the spatial structuring method for the excitation light and in the nature of the employed detector.

The setup for sFCCS is thought as an evolution of the existing sFCCS technology, reported in literature, but only used on simple artificial flows due to the complexity and low versatility of the system. While previouly reported setups were based on fixed focal points position, and on detection through separate photon counting detectors, the idea behind the setup here reported is that, using a pixelated detector, the position of the two focal points can be finely tuned, while preserving the ability to separately acquire the two signals. The advantage in the use of such setup lies in the possibility to adjust the distance between the two focuses, and their direction with respect to the flow direction. Moreover, the addition of a couple of galvanometric mirrors allows to realize two photon images of the sample, on which to select the position of the excitation focuses, and to perform parallel sFCCS measurements along a scanning line perpendicular to the flow direction.

The drawback in the use of a pixelated detector, and in particular, for the setup described, of an EMCCD is the limited temporal resolution, limited to a few hundreds of frames per second, compared to the nanosecond resolution of a photon counting based system. However, as illustrated in 9.2, characteristic times of sFCCS functions are usually on the millisecond scale, and are linearly dependent on the distance be-

tween the focuses, so that moving them apart reduces the requirements in temporal resolution.

The system was tested in simple artificial systems, in which it was able to provide reliable measurements of the flow speed and the diffusion coefficient, and to measure flow speed profiles in scanning mode. Moreover, it was employed for the first reported measurements of sFCCS in vivo, in Casper zebrafish embryos, providing the flow speed of fluorescent red blood cells, and estimates of the strain rates. Due to the high diameter of red blood cells, and to the complex non-Brownian motion of the blood flow, no realistic estimates of the diffusion coefficient are possible.

As for the calcium imaging setup, it is intended for the acquisition of calcium signals inside scattering tissues from multiple cells with a time resolution of at least one millisecond. Such value of the time resolution is of critical importance in neuroscience, as the basic event regulating the activity of a neuronal network, the action potential, lasts 1 ms, imposing the lower limit of the time scale on which neuronal information processing works. The only reported technique capable of achieving millisecond time resolution in acquisition in multiple locations is RAMP microscopy, but it is limited by the serial nature of the acquisition, so that only up to 20-30 points of interest can be monitored with millisecond time resolution.

The technique reported in this thesis is based on the use of a spatial light modulator for the excitation of the sample in multiple positions, and on the use of an high speed pixelated detector for signals acquisition. While the technique was recently reported by other groups, a key problem in such kind of setup is the use of a separate galvanometric mirrors for image formation, making the precise positioning of excitation focuses on structures of interest difficult. This thesis reports a scanless setup for the acquisition of full field two photon images with the spatial light modulator, and positioning of focal volumes on the structures on the images with sub-micrometer resolution.

The system proved to be capable of acquiring diffraction limited two photon images in two and three dimensions, in a completely digital procedure without any moving parts. Moreover, it was employed for high

speed two photon calcium imaging in acute cerebellar slices, acquiring signals from hundreds of cells simultaneously with millisecond time resolution, and providing the first single-cell resolution measurements of center-surround activation in the cerebellar granular layer.

These results confirm the reliability and efficiency of the technique, and open interesting new horizons in the study of the organization of neuronal networks.

Ringraziamenti

(English version in next page)

Durante questi tre anni ho avuto il privilegio di lavorare su due differenti progetti, in due laboratori distanti, sia geograficamente che nel campo di studio ed interesse. La più piacevole conseguenza di tutto ciò sta nella incredibile quantità (e qualità) delle persone con le quali ho avuto la possibilità di lavorare e interagire. Per ringraziare adeguatamente tutti non basterebbe una tesi intera: farò ciò che posso in questo paio di paginette (il cui carattere si è misteriosamente ristretto), citando un pò tutti in ordine semi-sparso, sperando di non commettere imperdonabili dimenticanze:

- Primi fra tutti i due "capi": Giberto, con la sua fiducia e il suo entusiasmo nell'assecondare ogni mia balzana idea sperimentale, ed Egidio, per il suo visionario impegno nel realizzare un piccolo paradiso per fisici nel suo laboratorio di elettrofisiologia.

- Jonathan e Daniela, per una quantità infinita di motivi, ma soprattutto per la disponibilità e l'entusiasmo nel coinvolgermi nel loro progetto sul due fotoni, oltre che in praticamente ogni nuova idea e impresa nella quale si sono imbarcati o si imbarcheranno.
  E per la quantità infinita di pranzi che mi hanno offerto: seriamente, la prima volta che passo da Modena offro io il gnocco fritto per tutti.

- Mary, spesso unica luce nel buio della stanza laser, oltre che unica barriera al disordine che genero imperterritamente, con la quale ho condiviso gioie e dolori della ricerca sperimentale, oltre a qualche segreta partita a Puzzle Bubble della quale nessuno deve sapere.

- La schiera dei tesisti passati dal setup dual spot del lab di Milano, che hanno spesso sopperito egregiamente alla mia assenza mentre ero a Pavia, oltre a costituire una costante fonte di idee e di ispirazione. In rigoroso ordine di apparizione, come nei titoli dei film: Leone, Alberto, Chiara, Francesca, Nicolò, Lorenzo e Michele.

- La "crew" del laboratorio di Pavia, per avermi accolto come uno di loro (solo un pò più strano), per aver gettato un pò di neurofisiologia nel terribile abisso della mia ignoranza, e per il numero francamente imbarazzante di fettine di cervelletto che hanno tagliato per me. Sperando di non dimenticare nessuno: Lisa, Licia, Teresa, Simona, le due Martine, le due Francesche, Gigi e Letizia. Una menzione speciale anche per Leda e Irene, che hanno lottato fieramente con la burocrazia mondinese per tutti gli strani acquisti della stanza laser.

- Gabriele, che ha costruito mezza stanza laser, e in tre anni, nonostante l'assurdità delle mie richieste, non mi ha mai detto "non si può".

- La popolazione del laboratorio di Milano, con la quale ho condiviso infinite ed infinitamente piacevoli colazioni e pranzi, oltre che ore e ore in laboratorio e una notte dei ricercatori particolarmente intensa: le boss Maddalena, Laura e Laura (sì, Sironi, sei una boss pure tu ormai!); i colleghi Margaux, Nikolas, Nicolò e Cassia, oltre a tutta la gioventù passata di lì per le varie tesi, in particolare Valeria, Sara e il Padelli (che la tesi deve ancora iniziarla, ma ormai siamo stanchi di vederlo).

- Il gruppo Zebrafish di Franco Cotelli dell'Università statale, e in particolare Efrem. Mai come in questo caso "Grazie per tutto il pesce". Un grazie anche ad Andrea e Luca, del Politecnico, per averceli fatti conoscere, ed averci fornito gli embrioni per le prime prove.

- Ultimi, ma forse i più importanti di tutti, i miei genitori, per il loro supporto su ogni fronte possibile alla mia carriera, e per l'ingiustificato enorme orgoglio che provano nei miei confronti. Grazie.

Acknowledgements

During these three years i had the privilege of working on two different projects, in two distant laboratories, both geographically and on their field of interests and study. The most pleasant consequence in this, is found in the quantity (and quality) of the people i had the chance to work and interact with. In order to acknowledge everyone in the way they deserve, an entire book would not be enough: i'll try to do my best in these two pages (written in a misteriously smaller character), naming everyone in semi-random order, hoping not to unforgivably forget anyone:

- First and foremost, my two "chiefs": Giberto, with the trust and enthusiasm he put in my every crazy experimental idea, and Egidio, for his visionary undertking in creating a small physicist's paradise inside his neurophysiology lab.

- Jonathan and Daniela, for an infinite amount of reasons, but mainly for the willingness and the enthusiasm with which they included me in their two-photon project, as well as in every new idea and project they had or are creating.
  And for the infinite amount of lunches they offered me: seriously, guys, next time i'm in Modena, i'll pay for your gnocco fritto.

- Mary, often the only light in the laser lab darkness, and only barrier to the disorder i keep continuously creating there. With her i share the joys and sorrows of experimental research, and some secret Puzzle Bubble matches, but nobody has to know about them.

- The crowd of thesis students who worked at the dual spot setup in Milan, often successfully filling my absence while i was in Pavia, and representing an inexaustible source of ideas and ispiration. In order of appearence, as in movie credits: Leone, Alberto, Chiara, Francesca, Nicolò, Lorenzo and Michele.

- The Pavia lab "crew", for welcoming me as one of their own (just a little weirder), for putting some neurophysiology in the bottomless abyss

of my ignorance, and for the frankly embarassing number of slices of cerebellum they cut for me. Hoping not to forget anyone: Lisa, Licia, Teresa, Simona, the two Martinas, the two Francescas, Gigi and Letizia. A special mention goes to rene and Leda, for their perennial fight against the Mondino burocracy in order to grant all the strange stuff we bought for the laser lab.

- Gabriele, who built half the laser room, and in three years never said "in can't be done", no matter how strange my requests were.

- The population of the Milano lab, with which i shared infinite breakfasts and lunches, togheter with many hours in the lab and the intense "MeetMeTonight" event: the bosses Maddalena, Laura and Laura (yes, Sironi, you are a boss now too!); my colleagues Margaux, Nikolas, Nicolò and Cassia, and all of the young people who passed by for their thesis, in particular Valeria, Sara, Lucy and Padelli (who still has to start his thesis, but we are already tire of seeing him everyday).

- The Zebrafish group of Franco Cotelli at the Milano Statale University, and in particular Efrem. Never before the phrase "thanks for all the fish" has been more appropriate. A special thank to Andrea and Luca, too, who made us meet Efrem, and gave us the embryos for the first trials.

- Last, but maybe the most important of all, my parents, for their support in every aspect of my career, and for the unjustified pride they have in my respect. Thanks.

Bibliography

[1] Eugene HECHT and Alfred ZAJAC. *Optics*. Addison-Wesley Publishing Company, London, 1974. LCCC No 79-184159.

[2] J.R. Lakowicz. *Principles of Fluorescence Spectroscopy*. Springer, 2007.

[3] E. WANG, C. M. BABBEY, and K. W. DUNN. Performance comparison between the high-speed yokogawa spinning disc confocal system and single-point scanning confocal systems. *Journal of Microscopy*, 218(2):148–159, 2005.

[4] Togo Shimozawa, Kazuo Yamagata, Takefumi Kondo, Shigeo Hayashi, Atsunori Shitamukai, Daijiro Konno, Fumio Matsuzaki, Jun Takayama, Shuichi Onami, Hiroshi Nakayama, Yasuhito Kosugi, Tomonobu M. Watanabe, Katsumasa Fujita, and Yuko Mimori-Kiyosue. Improving spinning disk confocal microscopy by preventing pinhole cross-talk for intravital imaging. *Proceedings of the National Academy of Sciences*, 110(9):3399–3404, 2013.

[5] Winfried Denk, James H Strickler, Watt W Webb, et al. Two-photon laser scanning fluorescence microscopy. *Science*, 248(4951):73–76, 1990.

[6] Jörg Bewersdorf, Rainer Pick, and Stefan W Hell. Multifocal multiphoton microscopy. *Optics letters*, 23(9):655–657, 1998.

[7] Milton Gottlieb, Clive LM Ireland, and John Martin Ley. Electro-optic and acousto-optic scanning and deflection. *New York, Marcel Dekker, Inc., 1983, 208 p.*, 1, 1983.

[8] R Salome, Y Kremer, S Dieudonne, J-F Léger, O Krichevsky, C Wyart, D Chatenay, and L Bourdieu. Ultrafast random-access scanning in two-photon microscopy using acousto-optic deflectors. *Journal of neuroscience methods*, 154(1):161–174, 2006.

[9] Gilbert F Amelio, Walter J Bertram Jr, and Michael F Tompsett. Charge-coupled imaging devices: Design considerations. *Electron Devices, IEEE Transactions on*, 18(11):986–992, 1971.

[10] Willard S Boyle and George E Smith. Charge coupled semiconductor devices. *Bell System Technical Journal*, 49(4):587–593, 1970.

[11] Peter JW Noble. Self-scanned silicon image detector arrays. *Electron Devices, IEEE Transactions on*, 15(4):202–209, 1968.

[12] Yuki Maruyama and Edoardo Charbon. An all-digital, time-gated 128x128 spad array for on-chip, filter-less fluorescence detection. In *Solid-State Sensors, Actuators and Microsystems Conference (TRANSDUCERS), 2011 16th International*, pages 1180–1183. IEEE, 2011.

[13] Cristiano Niclass and Edoardo Charbon. A single photon detector array with 64× 64 resolution and millimetric depth accuracy for 3d imaging. In *Solid-State Circuits Conference, 2005. Digest of Technical Papers. ISSCC. 2005 IEEE International*, pages 364–604. IEEE, 2005.

[14] Ryan A Colyer, Giuseppe Scalia, Ivan Rech, Angelo Gulinatti, Massimo Ghioni, Sergio Cova, Shimon Weiss, and Xavier Michalet. High-throughput fcs using an lcos spatial light modulator and an 8× 1 spad array. *Biomedical optics express*, 1(5):1408–1431, 2010.

[15] Eric R Kandel, James H Schwartz, Thomas M Jessell, et al. *Principles of neural science*, volume 4. McGraw-Hill New York, 2000.

[16] William F Ganong and William Ganong. *Review of medical physiology*, volume 18. Appleton & Lange Stamford, CT, 1997.

[17] Thomas C Watson, Nadine Becker, Richard Apps, and Matthew W Jones. Back to front: cerebellar connections and interactions with the prefrontal cortex. *Frontiers in systems neuroscience*, 8, 2014.

[18] Benjamin F Grewe, Dominik Langer, Hansjörg Kasper, Björn M Kampa, and Fritjof Helmchen. High-speed in vivo calcium imaging reveals neuronal network activity with near-millisecond precision. *Nature methods*, 7(5):399–405, 2010.

[19] Thomas Panier, Sebastián A Romano, Raphaël Olive, Thomas Pietri, Germán Sumbre, Raphaël Candelier, and Georges Debrégeas. Fast functional imaging of multiple brain regions in intact zebrafish larvae using selective plane illumination microscopy. *Frontiers in neural circuits*, 7, 2013.

[20] Alicia Lundby, Hiroki Mutoh, Dimitar Dimitrov, Walther Akemann, and Thomas Knöpfel. Engineering of a genetically encodable fluorescent voltage sensor exploiting fast ci-vsp voltage-sensing movements. *PloS one*, 3(6):e2514, 2008.

[21] Walther Akemann, Hiroki Mutoh, Amélie Perron, Jean Rossier, and Thomas Knöpfel. Imaging brain electric signals with genetically targeted voltage-sensitive fluorescent proteins. *Nature methods*, 7(8):643–649, 2010.

[22] Jonathan Mapelli and Egidio D'Angelo. The spatial organization of long-term synaptic plasticity at the input stage of cerebellum. *The Journal of neuroscience*, 27(6):1285–1296, 2007.

[23] Ping Yan, Corey D Acker, Wen-Liang Zhou, Peter Lee, Christian Bollensdorff, Adrian Negrean, Jacopo Lotti, Leonardo Sacconi, Srdjan D Antic, Peter Kohl, et al. Palette of fluorinated voltage-sensitive hemicyanine dyes. *Proceedings of the National Academy of Sciences*, 109(50):20443–20448, 2012.

[24] Luca Formaggia, Alfio M Quarteroni, and Alessandro Veneziani.

Cardiovascular mathematics. Number CMCS-BOOK-2009-001. Springer, 2009.

[25] Sumio Isogai, Masaharu Horiguchi, and Brant M Weinstein. The vascular anatomy of the developing zebrafish: an atlas of embryonic and early larval development. *Developmental biology*, 230(2):278–301, 2001.

[26] Luca Fieramonti, Efrem A Foglia, Stefano Malavasi, Cosimo D'Andrea, Gianluca Valentini, Franco Cotelli, and Andrea Bassi. Quantitative measurement of blood velocity in zebrafish with optical vector field tomography. *Journal of biophotonics*, 2013.

[27] Xianke Shi, Lin Shin Teo, Xiaotao Pan, Shang-Wei Chong, Rachel Kraut, Vladimir Korzh, and Thorsten Wohland. Probing events with single molecule sensitivity in zebrafish and drosophila embryos by fluorescence correlation spectroscopy. *Developmental Dynamics*, 238(12):3156–3167, 2009.

[28] Thorsten Wohland, Xianke Shi, Jagadish Sankaran, and Ernst HK Stelzer. Single plane illumination fluorescence correlation spectroscopy (spim-fcs) probes inhomogeneous three-dimensional environments. *Optics express*, 18(10):10627–10641, 2010.

[29] M.V. Klein. *Optics*. Wiley, 1970.

[30] Gabriel C Spalding, Johannes Courtial, and Roberto Di Leonardo. *Holographic optical tweezers*. Academic Press, 2008, (the chapter about iterative alghoritms is also available for free at http://sun.iwu.edu/~gspaldin/HOTsReview.pdf).

[31] Ralph W Gerchberg. A practical algorithm for the determination of phase from image and diffraction plane pictures. *Optik*, 35:237, 1972.

[32] Volodymyr Nikolenko, Brendon O Watson, Roberto Araya, Alan Woodruff, Darcy S Peterka, and Rafael Yuste. Slm microscopy: scanless two-photon imaging and photostimulation using spatial light modulators. *Frontiers in Neural Circuits*, 2(5), 2008.

[33] Sean Quirin, Jesse Jackson, Darcy S Peterka, and Rafael Yuste. Simultaneous imaging of neural activity in three dimensions. *Frontiers in Neural Circuits*, 8(29), 2014.

[34] Daniela Gandolfi, Paolo Pozzi, Marialuisa Tognolina, Giuseppe Chirico, Jonathan Mapelli, and Egidio D'Angelo. The spatiotemporal organization of cerebellar network activity resolved by two-photon imaging of multiple single neurons. *Frontiers in Cellular Neuroscience*, 8(92), 2014.

[35] Stephen G Brickley, Stuart G Cull-Candy, and Mark Farrant. Single-channel properties of synaptic and extrasynaptic gabaa receptors suggest differential targeting of receptor subtypes. *The Journal of neuroscience*, 19(8):2960–2973, 1999.

[36] Mark Farrant and Zoltan Nusser. Variations on an inhibitory theme: phasic and tonic activation of gabaa receptors. *Nature Reviews Neuroscience*, 6(3):215–229, 2005.

[37] M Martina, G Kilić, and E Cherubini. The effect of intracellular ca2+ on gaba-activated currents in cerebellar granule cells in culture. *The Journal of membrane biology*, 142(2):209–216, 1994.

[38] J. Garthwaite and A. R. Brodbelt. Synaptic activation of N-methyl-D-aspartate and non-N-methyl-D-aspartate receptors in the mossy fibre pathway in adult and immature rat cerebellar slices. *Neuroscience*, 29(2):401–412, 1989.

[39] E D'angelo, P Rossi, and J Garthwaite. Dual-component nmda receptor currents at a single central synapse. *Nature*, 346(6283):467–470, 1990.

[40] E D'Angelo, G De Filippi, P Rossi, and V Taglietti. Synaptic excitation of individual rat cerebellar granule cells in situ: evidence for the role of nmda receptors. *The Journal of Physiology*, 484(Pt 2):397–413, 1995.

[41] S. Armano, P. Rossi, V. Taglietti, and E. D'Angelo. Long-term potentiation of intrinsic excitability at the mossy fiber-granule cell

synapse of rat cerebellum. *J. Neurosci.*, 20(14):5208–5216, Jul 2000.

[42] C. L. Ojakangas and T. J. Ebner. Purkinje cell complex and simple spike changes during a voluntary arm movement learning task in the monkey. *J. Neurophysiol.*, 68(6):2222–2236, Dec 1992.

[43] Jonathan Mapelli, Daniela Gandolfi, and Egidio D'Angelo. Combinatorial responses controlled by synaptic inhibition in the cerebellum granular layer. *Journal of neurophysiology*, 103(1):250–261, 2010.

[44] Douglas Magde, Elliot Elson, and W. W. Webb. Thermodynamic fluctuations in a reacting system—measurement by fluorescence correlation spectroscopy. *Phys. Rev. Lett.*, 29:705–708, Sep 1972.

[45] Olga I Vinogradova, Kaloian Koynov, Andreas Best, and François Feuillebois. Direct measurements of hydrophobic slippage using double-focus fluorescence cross-correlation. *Physical review letters*, 102(11):118302, 2009.

[46] Petra S Dittrich and Petra Schwille. Spatial two-photon fluorescence cross-correlation spectroscopy for controlling molecular transport in microfluidic structures. *Analytical chemistry*, 74(17):4472–4479, 2002.

[47] Molly J Rossow, William W Mantulin, and Enrico Gratton. Scanning laser image correlation for measurement of flow. *Journal of biomedical optics*, 15(2):026003–026003, 2010.

[48] Benedict Hebert, Santiago Costantino, and Paul W Wiseman. Spatiotemporal image correlation spectroscopy (stics) theory, verification, and application to protein velocity mapping in living cho cells. *Biophysical journal*, 88(5):3601–3614, 2005.

[49] SK Wilson and BR Duffy. A rivulet of perfectly wetting fluid draining steadily down a slowly varying substrate. *IMA journal of applied mathematics*, 70(2):293–322, 2005.

[50] Y Kuo and RI Tanner. Laminar newtonian flow in open channels with surface tension. *International Journal of Mechanical Sciences*, 14(12):861–873, 1972.

[51] Henrik Bruus. Theoretical microfluidics. 2008.

[52] CB Müller, A Loman, V Pacheco, F Koberling, D Willbold, W Richtering, and J Enderlein. Precise measurement of diffusion by multi-color dual-focus fluorescence correlation spectroscopy. *EPL (Europhysics Letters)*, 83(4):46001, 2008.

[53] Giuseppe Chirico, Piersandro Pallavicini, and Maddalena Collini. Gold nanostars for superficial diseases: a promising tool for localized hyperthermia? *Nanomedicine*, 9(1):1–3, 2014.

[54] Ana J García-Sáez and Petra Schwille. Surface analysis of membrane dynamics. *Biochimica et Biophysica Acta (BBA)-Biomembranes*, 1798(4):766–776, 2010.

[55] Paolo Pozzi, Laura Sironi, Laura D′Alfonso, Margaux Bouzin, Maddalena Collini, Giuseppe Chirico, Piersandro Pallavicini, Franco Cotelli, and Efrem A Foglia. Electron multiplying charge-coupled device-based fluorescence cross-correlation spectroscopy for blood velocimetry on zebrafish embryos. *Journal of biomedical optics*, 19(6):067007–067007, 2014.

[56] Jonathan B Freund, Jacky G Goetz, Kent L Hill, and Julien Vermot. Fluid flows and forces in development: functions, features and biophysical principles. *Development*, 139(7):1229–1245, 2012.

[57] Yannick Blum, Heinz-Georg Belting, Elin Ellertsdottir, Lukas Herwig, Florian Lüders, and Markus Affolter. Complex cell rearrangements during intersegmental vessel sprouting and vessel fusion in the zebrafish embryo. *Developmental biology*, 316(2):312–322, 2008.

[58] Vincent T Turitto and Hans R Baumgartner. Platelet interaction with subendothelium in flowing rabbit blood: effect of blood shear rate. *Microvascular Research*, 17(1):38–54, 1979.

[59] GJ Tangelder, DICK W Slaaf, THEO Arts, and ROBERT S Reneman. Wall shear rate in arterioles in vivo: least estimates from platelet velocity profiles. *Am J Physiol*, 254(6 Pt 2):H1059–H1064, 1988.

[60] Xiaotao Pan, Hanry Yu, Xianke Shi, Vladimir Korzh, and Thorsten Wohland. Characterization of flow direction in microchannels and zebrafish blood vessels by scanning fluorescence correlation spectroscopy. *Journal of biomedical optics*, 12(1):014034–014034, 2007.

[61] M Oishi, K Utsubo, H Kinoshita, T Fujii, and M Oshima. Continuous and simultaneous measurement of the tank-treading motion of red blood cells and the surrounding flow using translational confocal micro-particle image velocimetry (micro-piv) with sub-micron resolution. *Measurement Science and Technology*, 23(3):035301, 2012.

[62] Peter Vennemann, Kenneth T Kiger, Ralph Lindken, Bianca CW Groenendijk, Sandra Stekelenburg-de Vos, Timo LM ten Hagen, Nicolette TC Ursem, Rob E Poelmann, Jerry Westerweel, and Beerend P Hierck. In vivo micro particle image velocimetry measurements of blood-plasma in the embryonic avian heart. *Journal of biomechanics*, 39(7):1191–1200, 2006.

[63] Michael L Smith, David S Long, Edward R Damiano, and Klaus Ley. Near-wall< i> μ</i>-piv reveals a hydrodynamically relevant endothelial surface layer in venules in vivo. *Biophysical journal*, 85(1):637–645, 2003.

[64] Haiying Cheng, Qingming Luo, Shaoqun Zeng, Shangbin Chen, Jian Cen, and Hui Gong. Modified laser speckle imaging method with improved spatial resolution. *Journal of Biomedical Optics*, 8(3):559–564, 2003.

[65] W Wang, Y Liu, GJ Sonek, MW Berns, and RA Keller. Optical trapping and fluorescence detection in laminar flow streams. *Applied physics letters*, 67(8):1057–1059, 1995.

[66] B Manz, P Stilbs, B Jönsson, O Söderman, and PT Callaghan. Nmr imaging of the time evolution of electroosmotic flow in a capillary. *The Journal of Physical Chemistry*, 99(29):11297–11301, 1995.

[67] Robert S Reneman, Theo Arts, and Arnold PG Hoeks. Wall shear stress–an important determinant of endothelial cell function and structure–in the arterial system in vivo. *Journal of vascular research*, 43(3):251–269, 2006.

[68] Jay R Hove, Reinhard W Köster, Arian S Forouhar, Gabriel Acevedo-Bolton, Scott E Fraser, and Morteza Gharib. Intracardiac fluid forces are an essential epigenetic factor for embryonic cardiogenesis. *Nature*, 421(6919):172–177, 2003.

[69] Chia-Yuan Chen, Michael J Patrick, Paola Corti, William Kowalski, Beth L Roman, and Kerem Pekkan. Analysis of early embryonic great-vessel microcirculation in zebrafish using high-speed confocal μpiv. *Biorheology*, 48(5):305–321, 2011.

[70] Zhangyi Zhong, Hongxin Song, Toco Yuen Ping Chui, Benno L Petrig, and Stephen A Burns. Noninvasive measurements and analysis of blood velocity profiles in human retinal vessels. *Investigative ophthalmology & visual science*, 52(7):4151–4157, 2011.

[71] Peter Gaehtgens, Herbert J Meiselman, and Harold Wayland. Velocity profiles of human blood at normal and reduced hematocrit in glass tubes up to 130 μ diameter. *Microvascular research*, 2(1):13–23, 1970.

[72] RT Yen and YC Fung. Effect of velocity distribution on red cell distribution in capillary blood vessels. *American Journal of Physiology-Heart and Circulatory Physiology*, 235(2):H251–H257, 1978.

[73] Timothy W Secomb. Mechanics of blood flow in the microcirculation. *Biomedical Flows at Low Reynolds Numbers*, page 9, 1995.